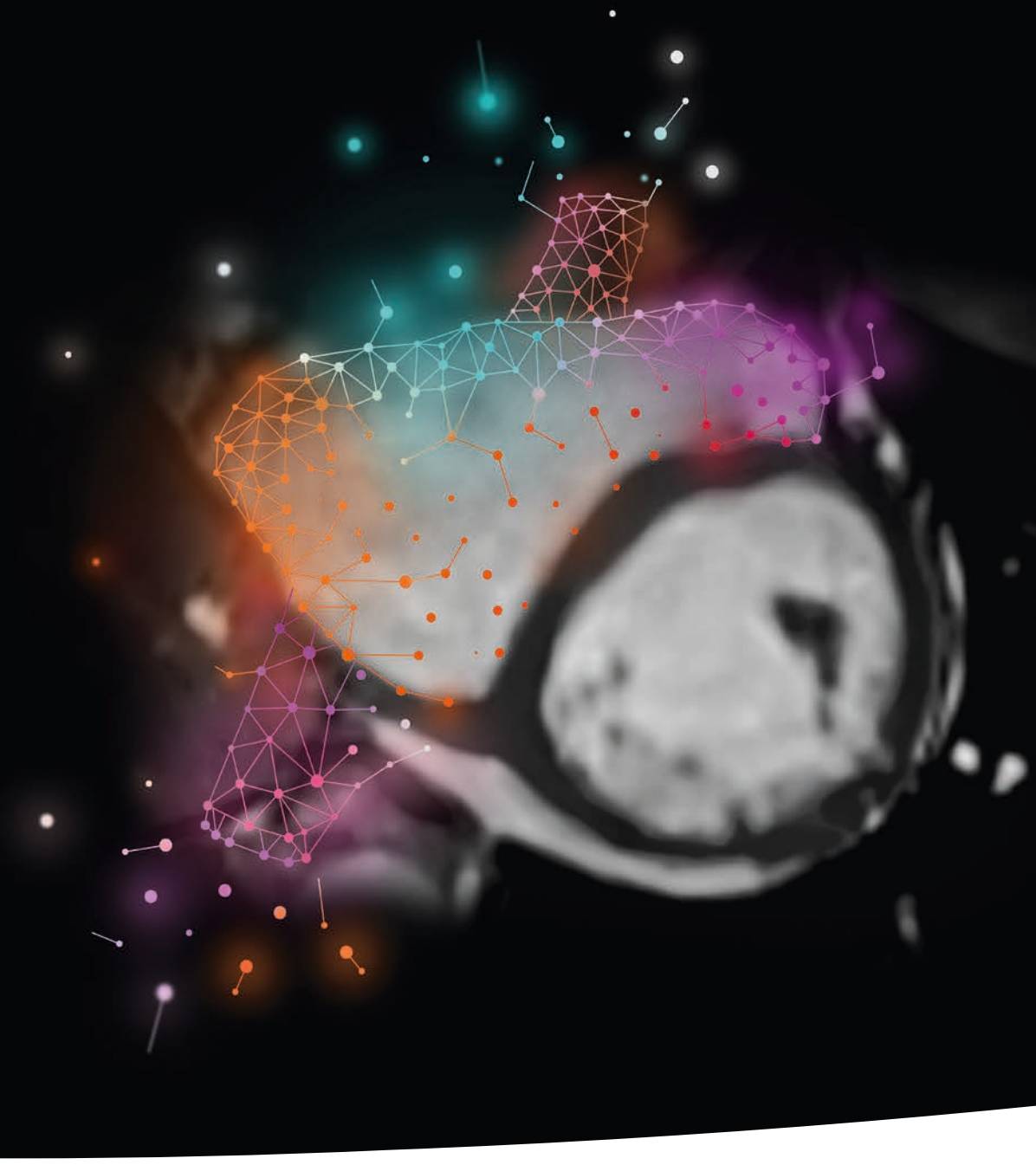

MAGNETOM Flash

Issue Number 67, 1/2017
SCMR Edition

siemens.com/magnetom-world

SIEMENS Healthineers

Professor Jeanette Schulz-Menger

Jeanette Schulz-Menger is from Berlin, Germany. She is married and has a 22-year-old son, who is studying medicine. She is a cardiologist by training and active in CMR since 1996. In 2008 the Charité University Medicine Berlin created a chair in Cardiovascular Imaging housed in Cardiology, based on a close collaboration with the HELIOS-Clinics, Germany, and appointed Professor Jeanette Schulz-Menger to this chair. She heads a group focusing on clinically oriented CMR-research that has been able to establish new structures including a CMR-driven research setting working in close collaboration with the Max-Delbrueck-Center (MDC). The main interest has remained the CMR-driven understanding of myocardial injury and its relation to the cardiovascular system. They have established new structures including the extension of CMR-research from 1.5 Tesla (dedicated cardiac system) to 3T to 7T. Over recent years a new post-processing lab (CMR reading and development) has been installed, allowing to speed up processes. In 2011 an academic outpatient department of cardiology was founded under Professor Schulz-Menger's leadership, allowing a personalized phenotyping and the

Cardiovascular Magnetic Resonance – a routine tool for clinical decision-making and an exciting research instrument. The non-invasive chance to improve the understanding of cardiology

Dear colleagues,

Writing an editorial without repeating the ideas of the authors is always a challenge, and an editorial is always, of course, a personal view. It has become a welcome tradition that MAGNETOM Flash has a special SCMR edition. That means we are lucky ones, as we are always the first publication of the new year – an exciting start.

Although CMR itself has a longer history, SCMR celebrates its 20th anniversary in 2017.

This issue of MAGNETOM Flash nicely reflects the different aspects we wish to see covered by CMR. I had already used one of the last SCMR-Newsletters to share with you the thought that we as the Board of Trustees of SCMR developed during our last strategic meeting: That it is our responsibility to convince patients and referring doctors that CMR not only has a place in guidelines, but is suitable in the clinical environment. Utilizing CMR instead of other non-invasive imaging techniques means that one will get more definitive, relevant, and actionable answers because a CMR exam provides comprehensive information and has superior diagnostic and prognostic power, without the need for radiation. Furthermore, there are CMR-only capabilities including virtual heart biopsy, high-resolution perfusion imaging, and advanced blood flow analysis.

This MAGNETOM Flash issue provides aspects from sequence development to clinical application as well as tips and tricks helping to meet the overarching aim.

The authors share exciting news, as well as cookbook-like approaches to improve image quality. This aspect has a high priority, as it will help technologists not only to meet the needs of high-quality CMR, but also to enhance the understanding that CMR is doable today on a routine basis. As evidence of this, CMR is today mentioned in more than 29 guidelines of the European Society of Cardiology [1]. We have well-accepted and standardized SCMR protocols [2] and advices for post-processing [3]. But the aim to make the method easier and more time-efficient is also reflected in technical developments and has already allowed us a short time later e.g. to publish a consensus statement with a proposal for a 20-minute stress perfusion [4].

establishment of a research database dedicated to patient oriented research. The group is committed to CMR education, offering courses in different structures and they have established a teaching network within the HELIOS-clinics. As a cardiologist, Professor Schulz-Menger also has clinical responsibilities regarding imaging. One major achievement has been the leading participation in the successful application for the German Center of Cardiovascular Research (GCCR) within which Professor Schulz-Menger is one of the Principal Investigators of the Charité.

She was Founding Director and interim Co-Director of the Berlin Ultrahigh Field Facility of the Max-Delbrueck-Center and thus one of the leading forces in the successful application for the 7 Tesla human scanner at the MDC and the implementation of a fruitful collaboration between MDC, Charité, PTB and Siemens Healthcare. She is an elected member of the Council of the Charité. Following the intention to bring CMR-research into clinical reality, she has also been active in several imaging societies, including the Society of Cardiovascular Magnetic Resonance.

Berlin, Germany

In the following I will aim to reflect on the articles in this issue of MAGNETOM Flash in the light of these thoughts.

Fast free-breathing techniques assist considerably in the goal towards a reliable and efficient exam, easy for patients. Peter Kellman and co-workers are introducing a free-breathing Late Enhancement Imaging technique. The Phase Sensitive Inversion Recovery (PSIR) with Respiratory Motion Corrected (MOCO) averaging[1] allows high-resolution free breathing imaging. The technique gives not only the chance to increase diagnostic accuracy, but also to broaden the application of CMR to a vulnerable population. The images nicely demonstrate the high quality that is achievable.

Whilst the constant focus of attention is the patient, the ease of handling may also be an obstacle for technologists. That is often the case, for example, if CMR is not the only application at a dedicated scanner. However, it should be the norm, that all indications are covered, from knee, to brain, to heart.

Armando et al. report on their experience with an upgrade from MAGNETOM Avanto to Avanto^{fit}. The Italian group shares the experience of the improved ease of use and the resulting effectivity. They have been able to reach a reduction of acquisition times of about 40%. Interestingly, that was also translated in a use of more challenging techniques. They state that they are now able to perform the complete Lake Louise protocol [5] for assessment of acute myocarditis including early enhancement increasing the number of positive findings. As the assessment of inflammatory diseases and cardiomyopathies reflect a unique capability of CMR, this has an implication for clinical decision-making. Our own experiences with the need for fast and efficient scanning are illustrated by some case-examples. In our own environment the referring doctors don't pay particluar attention to arrhythmias or other limiting factors like patient's conditions e.g. the capability to hold their breath or the case of deafness. We try to scan all patients and in nearly all of them we are able to provide a diagnosis and therapeutic guidance. But that means that techniques like real-time cine or motion-corrected perfusion are crucial. The latter is already a routine tool leading to free-breathing stress perfusion in all patients. That is convenient for patients and also for medical staff, as the sequence can be started immediately when reaching the adenosine effect and furthermore, the slice position is much more predictable.

Ease of use and reproducibility of a scan were also the reason for Jonathan Richer to summarize in a cookbook like approach the imaging of the coronaries themselves.

However, CMR would not be CMR if we did not have scientists crossing the borders of our known and familiar world. Those thoughts are often the driving forces for further developments. But no doubt, new possibilities, new awareness can be initiated from both sides: the clinical and the scientific. It is a pleasure to recognize that the basic idea of our joint ISMRM/SCMR workshop is also present in several articles. The exchange of existing knowledge and beyond is the basis for a network in medicine as introduced by Chan and Loscalzo in 2012. They referred to the interaction of basic research and clinical research [6].

Christoph Forman and co-workers introduce in their article the potential of Compressed Sensing[2] for CMR. They explain the current stage and its potential in detail. Compressed Sensing will allow rapid CMR imaging based on a dedicated data acquisition and image reconstruction. The acceleration can be translated into a reduction of the acquisition time or into spatial and/or temporal resolution. Compressed Sensing in a clinical setting would allow an improved real-time imaging reducing the need for breath-holding. This new feature of the Siemens Healthineers-Team will be integrated in the scanner environment, allowing a further introduction of applications.

[1] WIP, the product is currently under development and is not for sale in the US and in other countries. Its future availability cannot be ensured.

[2] 510(k) pending. Compressed Sensing Cardiac Cine is not commercially available. Future availability cannot be guaranteed.

"Utilizing CMR instead of other non-invasive imaging techniques means, that one will get more definitive, relevant, and actionable answers because a CMR exam provides comprehensive information and has superior diagnostic and prognostic power, without the need for radiation. Not to forget unique CMR capabilities like virtual heart biopsy, high-resolution perfusion imaging, and advanced blood flow analysis."

Professor Jeanette Schulz-Menger

While Compressed Sensing sounds like a future tool in CMR, one can already appreciate first examples especially in vessel imaging. Yamamoto et al. demonstrate a Compressed Sensing based Time-of-Flight MR Angiography[1]. The technique has been used for visualization of cerebral arteries and was able to reduce the scan time while minimizing loss of image quality at high acceleration rates. It is impressive to see these first experiences in clinical setting using highly accelerated CS-TOF. Compressed Sensing seems also to allow the imaging of medium-to-small sized pulmonary vasculature. Wintersperger et al. describe their promising experience with iterative TWIST[1] as a dynamic angiography. If IT-TWIST were really to allow "a straightforward inject-and-shoot CE-MRA protocol without the need for any bolus timing" as stated by the authors, it would again help us to simplify CMR.

First clinical experience is also demonstrated using exercise CMR as described by group from Australia. Strugnell at al. have used a prototype of a Compressed Sensing[2] bSSFP sequence exercise ergo-metry in healthy volunteers as well as in patients. They conclude that in this pilot test the application of this highly accelerated imaging sequence has allowed the assessment of biventricular response during exercise with a reliability that was not previously possible. Both groups agree that further trials are needed to confirm these results. Nevertheless, this could be the start of a new era.

Improvement of assessment of ischemia is an ongoing research field, despite its accepted value in clinical routine. Juliano L. Fernandes et al. have successfully aplied parametric mapping for assessment of myocardial ischemia. T2* mapping is already known to be suitable for assessment of myocardial perfusion abnormalities. However, they applied T1 and T2 mapping sequences during stress, potentially reflecting changes in the myocardial intravascular components. The authors indicate that the application of native T1 mapping could reduce the need for gadolinium-based contrast agents, as T1 mapping allows the detection of different pathologies. At the current stage it should be one part of a protocol in most of the indications.

CMR allows the assessment of the heart itself, but at least as important is the capability to assess the cardiovascular system. The interaction between myocardial, structural and vascular diseases is one of the true challenges in clinical decision making. The assessment of the vessels themselves has a long history in MRI, where 4D Flow experienced an increasing recognition in recent years. Michael Markl and co-workers provide a comprehensive update on 4D Flow MRI. 4D Flow opens the door to a noninvasive assessment on hemodynamics and its impact on prognosis. An increasing number of groups are currently working in this field, so one could assume that in the near future multi-center trials will help to identify the value of 4D for clinical decision making in different fields. In congenital heart disease this value is already demonstrated.

A next step could be high-quality 4D magnitude images to overcome the need for an additional angiography. But on the other hand, it is an advantage that high-quality MR-angiographies are part of a clinical routine. It is generally accepted that, depending on anatomy and pathology, MRAs can be challenging.

Botelho et al. from Chicago provide protocols for the imaging of calcified vasculature using PETRA and FREEZEit StarVIBE. These protocols allow use at different field strengths. The imaging of calcified vessels will experience growing impact due to the increasing number of complex interventions in the ageing society.

The assessment of atherosclerosis in all vessel territories is a clinical need. But more relevant than the visualization itself is the plaque characterization and/or the impact on perfusion. There is an ongoing effort to identify the vulnerable plaque. It seems that application of MR/PET using new tracers will help to cut the Gordion knot.

[1] WIP, the product is currently under development and is not for sale in the US and in other countries. Its future availability cannot be ensured.
[2] 510(k) pending. Compressed Sensing Cardiac Cine is not commercially available. Future availability cannot be guaranteed.

Colleagues from New York and Edinburgh present a case using ^{18}F-NaF applying coronary MR/PET. They have been able to detect disease activity in the coronaries. Using MR/PET instead of PET/CT would again allow a reduction in radiation dose. MR/PET in CMR is currently mainly recognized as a research tool. But the group from Mount Sinai demonstrated a case with an active cardiac sarcoidosis. The combination ^{18}F-FDG PET and MR may help to indicate disease activity and this could have a clinical impact soon.

This MAGNETOM Flash gives us a flavor of the multiple features of CMR. CMR is here, and today it can be applied quickly and efficiently in clinical routine. I will conclude with the words of German writer Bertolt Brecht. In one of his *"Stories of Mr. Keuner"* he describes how a man who had not seen the protagonist Mr. K for a long time greeted him with the words: "You haven´t changed at all". "Oh!" replied Mr. K, and turned pale."

In my view, this says a lot about our work and life. It is no compliment to be told you haven't changed. Change is desirable and necessary. It is this constant drive for change that is the motor for all scientific progress.

Jeanette Schulz-Menger, M.D.

References

1 von Knobelsdorff-Brenkenhoff F, Schulz-Menger J. Role of cardiovascular magnetic resonance in the guidelines of the European Society of Cardiology. J Cardiovasc Magn Reson. 2016;18:6. doi: 10.1186/s12968-016-0225-6. PubMed PMID: 26800662; PubMed Central PMCID: PMCPMC4724113.

2 Standardized cardiovascular magnetic resonance (CMR) protocols 2013 update. Kramer CM, Barkhausen J, Flamm SD, Kim RJ, Nagel E; Society for Cardiovascular Magnetic Resonance Board of Trustees Task Force on Standardized Protocols. J Cardiovasc Magn Reson. 2013 Oct 8;15:91. doi: 10.1186/1532-429X-15-91.

3 Schulz-Menger J, Bluemke DA, Bremerich J, Flamm SD, Fogel MA, Friedrich MG, et al. Standardized image interpretation and post processing in cardiovascular magnetic resonance: Society for Cardiovascular Magnetic Resonance (SCMR) board of trustees task force on standardized post processing. Journal of cardiovascular magnetic resonance : official journal of the Society for Cardiovascular Magnetic Resonance. 2013;15:35. Epub 2013/05/03. doi: 10.1186/1532-429X-15-35. PubMed PMID: 23634753; PubMed Central PMCID: PMC3695769.

4 CMR First-Pass Perfusion for Suspected Inducible Myocardial Ischemia. Hendel RC, Friedrich MG, Schulz-Menger J, Zemmrich C, Bengel F, Berman DS, Camici PG, Flamm SD, Le Guludec D, Kim R, Lombardi M, Mahmarian J, Sechtem U, Nagel E. JACC Cardiovasc Imaging. 2016 Nov;9(11):1338-1348. doi: 10.1016/j.jcmg.2016.09.010.

5 Friedrich MG, Sechtem U, Schulz-Menger J, Holmvang G, Alakija P, Cooper LT, et al. Cardiovascular magnetic resonance in myocarditis: A JACC White Paper. J Am Coll Cardiol. 2009;53(17):1475-87. Epub 2009/04/25. doi: S0735-1097(09)00496-3 [pii] 10.1016/j.jacc.2009.02.007. PubMed PMID: 19389557; PubMed Central PMCID: PMC2743893.

6 Chan SY, Loscalzo J. The emerging paradigm of network medicine in the study of human disease. Circ Res. 2012 Jul 20;111(3):359-74. doi: 10.1161/CIRCRESAHA.111.258541.

Content

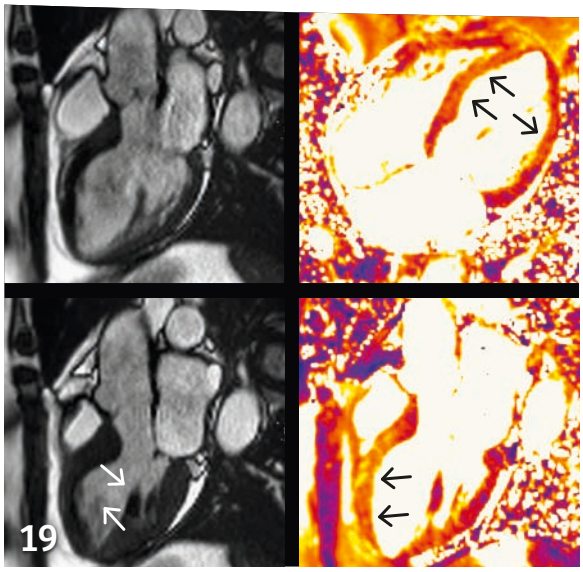

CMRI for very sick patients

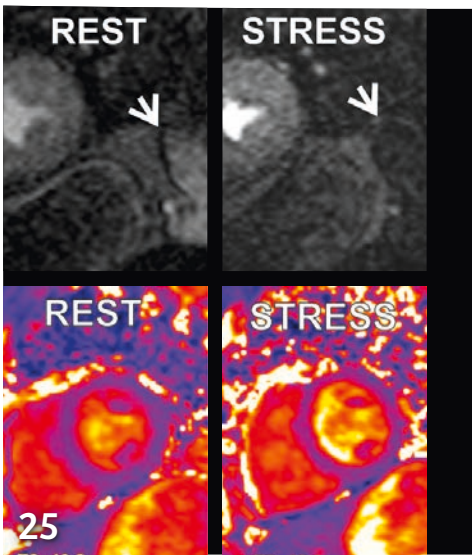

Stress-mapping for the assessment of myocardial ischemia

Learn from the experience of other MAGNETOM users

The MAGNETOM World is the community of Siemens MR users worldwide, providing you with relevant clinical information. Here you will find application tips and protocols to optimize your daily work. Lectures and presentations from experts in the field will allow you to be exposed to new ideas and alternative clinical approaches.

Put the advantages of the MAGNETOM World to work for you!

siemens.com/magnetom-world

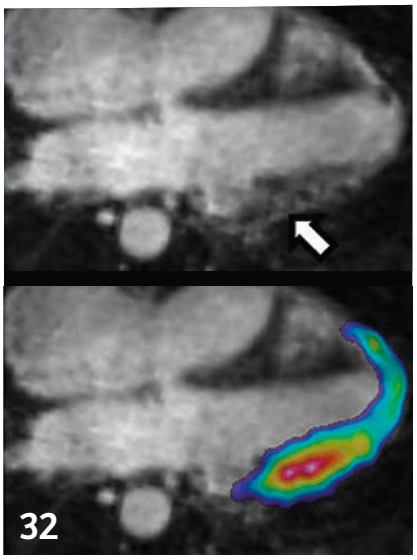

^{18}F-FDG PET/MR for imaging of active cardiac sarcoidosis

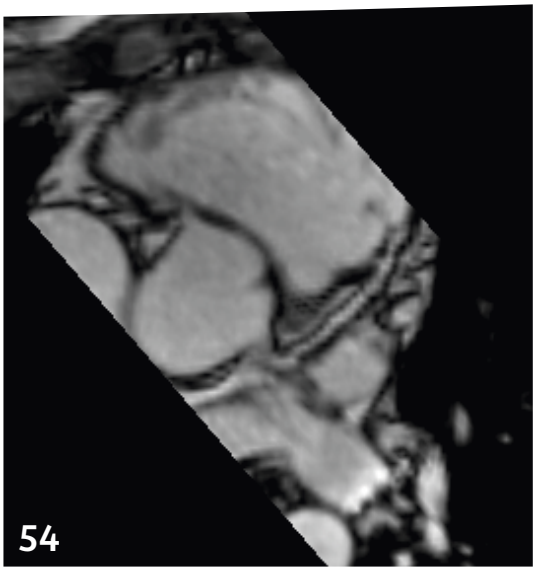

How-I-do-it: coronary root imaging

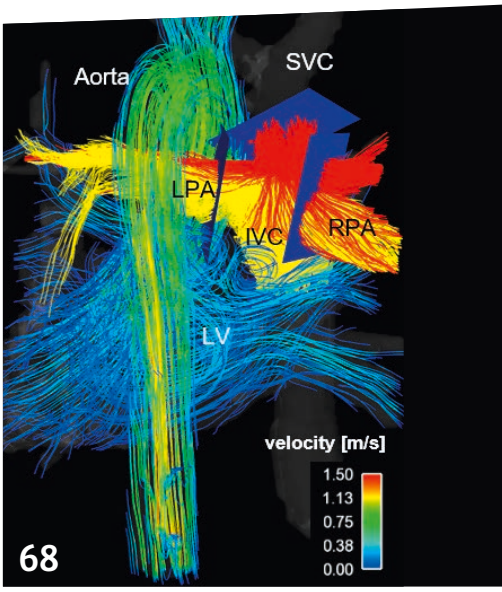

4D Flow MRI

Cardiovascular Imaging

Meet Siemens Healthineers

[1] 510(k) pending. Compressed Sensing Cardiac Cine is not commercially available. Future availability cannot be guaranteed.
[2] WIP, the product is currently under development and is not for sale in the US and in other countries. Its future availability cannot be ensured.

Cardiac MRI: Image Quality Improvement and Examination Time Shortening After MAGNETOM Avanto^{fit} Upgrade

Enrico Armando; Leonardo Maria Capitolo; Federico Cesarani

Radiology Department, Ospedale Cardinal Massaia, Asti, Italy

Introduction

Cardiac MRI examinations have long been considered too difficult for general radiologists and radiographers and have therefore often been restricted to academic or dedicated heart centers.

The main technical difficulty of a standard cardiac MRI protocol for the assessment of cardiac function and tissue characterization is the high number of breath-hold and cardiac triggered sequences (about fifty) along cardiac planes, which differ from the anatomical sagittal, coronal and axial planes used in almost every other body application.

Gaining time

However, at the Radiology Department of Cardinal Massaia Hospital in Asti, Italy, thanks to the 2014 upgrade of our MAGNETOM Avanto scanner to MAGNETOM Avanto^{fit}, cardiac MRI has progressed steadily from being the nightmare of every radiographer – due to its length and difficulty – to become a routine examination of about the same duration as a conventional brain protocol for multiple sclerosis.

Before the upgrade, a conventional cardiac MRI protocol including cine SSFP on cardiac long and short axis, evaluation of myocardial edema with triple inversion recovery sequences, perfusion FLASH sequences, early and late enhancement IR or PSIR T1w images, lasted about one hour from the first scout sequence to the last one (Figure 1, Group A).

The first innovation – the introduction of the automatic commands for breath-hold – has shortened the examination time. Since the radiographers are no longer focused on speaking to the patient, they can instead plan the next sequence (Figure 1, Group B), a saving of about 10 minutes.

The second improvement has resulted in a better image quality due to the higher number of coil channels and the possibility to use GRAPPA in cine SSFP sequences: Image resolution is higher, SAR (specific absorption rate) is lower, and it is possible to increase the flip angle of cine SSFP from 55° to 80°, performing short axis cine SSFP sequences after

1

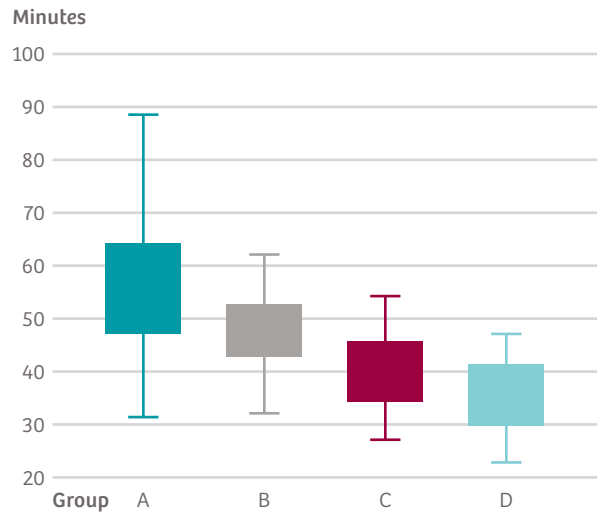

Figure 1: Length of MRI examinations in four groups showing the changes in cardiac MRI protocol.

2

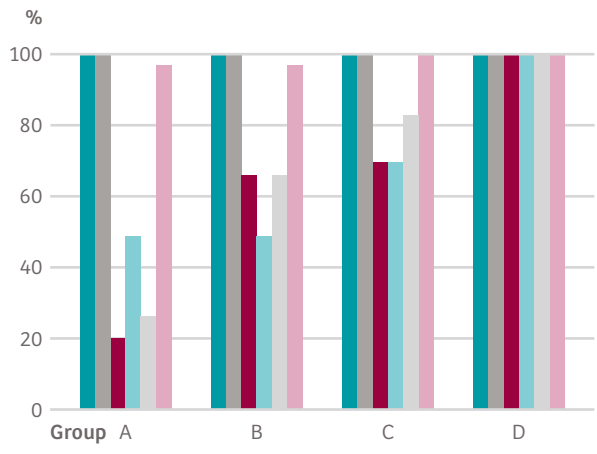

Figure 2: While scout and axial images (petrol), cine SSFP (gray) and late enhancement images (light red) were almost always performed in every group, the percentage of examinations with T2 triple IR (red), perfusion (light petrol) and early enhancement (light gray) increased from less than 50% in group A to almost 100% in group D.

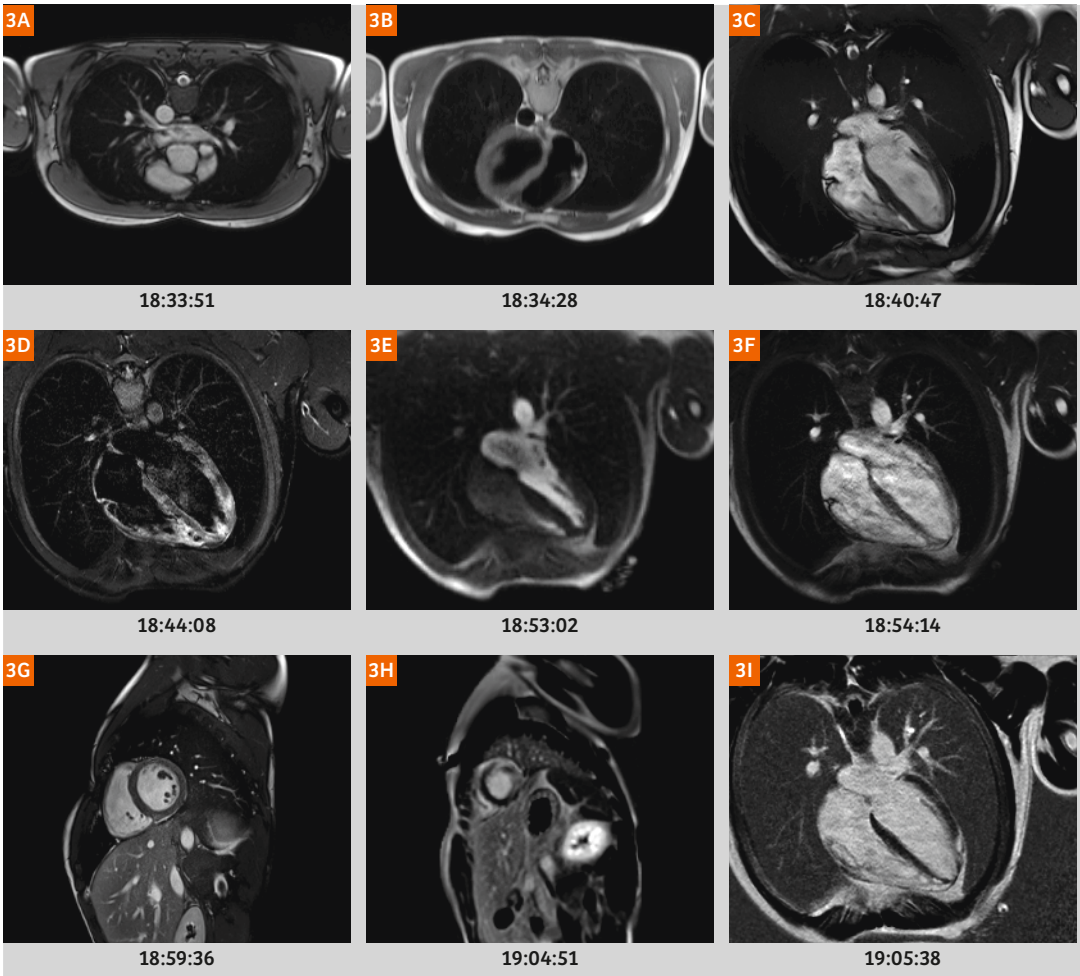

Figure 3:
A 32-minute complete protocol for myocarditis using axial TrueFISP and T2w HASTE sequences **(3A, B),** TrueFISP cine long axis **(3C),** T2w triple IR images **(3D),** GRE perfusion images **(3G),** PSIR late enhancement sequences along short and long cardiac axis **(3H, I),** showing patchy edema, early and late enhancement in the apical anterior, lateral and inferior walls of the left ventricle and in the apical free wall of the right ventricle.

the administration of paramagnetic contrast medium. This protocol change has also allowed a mean reduction in scan time of an additional 8 minutes (Figure 1, Group C).

Finally, by changing the protocol design, we were able to further exploit the features of the *syngo* MR D13 software. Once the radiographer has set the cardiac long axis and short axis planes, the following sequences automatically copy the measurement parameters, including field-of-view, phase oversampling and matrix. All the radiographer needs to do is adapt the sequence to the cardiac cycle, shortening the examination time even further to 35.8 minutes (Figure 1, Group D).

Conclusion

An analysis of our cardiac examinations reveals a reduction in acquisition times of about 40%, alongside an actual increase in the number of sequences (Figure 2). Prior to the scanner upgrade, the length of the examination meant that rest perfusion imaging, T2 triple inversion recovery imaging and early enhancement were performed in less than 50% of our patients. With the upgrade, almost all our patients undergo a complete examination. Moreover in the definition of acute myocarditis it is now possible to perform every long axis early enhancement IR sequence twice, increasing the number of positive findings because of fewer movement artifacts.

As an example, we share images of a patient who underwent a cardiac MRI examination before the upgrade in the follow-up exam of myocarditis, and after the upgrade during a myocarditis relapse. The first examination lasted one hour and included cine long and short axis and late enhancement PSIR images. The second examination lasted 32 minutes, including cine SSFP short and long axis, T2 IR, rest perfusion imaging, early and late enhancement (Figure 3).

Contact

Enrico Armando, M.D.

Radiology Department

Ospedale Cardinal Massaia Asti
Corso dante 202
14100 Asti
Italy
enrico.armando@gmail.com

Compressed Sensing: a Paradigm Shift in MRI

Christoph Forman[1]; Jens Wetzl[2]; Carmel Hayes[1]; Michaela Schmidt[1]

[1] Siemens Healthineers, Magnetic Resonance, Erlangen, Germany
[2] Pattern Recognition Lab, Friedrich-Alexander-University Erlangen-Nuremberg, Erlangen, Germany

Introduction

Reducing the complexity and length of examinations has been a major direction of research in magnetic resonance imaging (MRI) in recent years. With the introduction of the Dot engines, the complexity of MR examinations could be reduced through automatization and guidance, providing standardized and time-efficient workflows. Considerable effort has also been spent on developing methods to speed up data acquisition without degrading image quality. Accelerated imaging is a key factor to enable the visualization of rapid physiological or contrast changes in dynamic imaging. Moreover, short scans reduce the risk of artifacts due to any kind of motion during the scan.

A significant speed-up of data acquisition allows both respiratory and cardiac motion to be frozen while maintaining an adequate temporal and spatial resolution. This in turn results in a high-quality and robust examination even for uncooperative patients, since data acquisition may be performed in free breathing. Furthermore, reduced scan time and a decreased number of breath-holds improve patient comfort. Last but not least, accelerated imaging means shorter examinations that can be invested in additional scans, higher resolution, or to improve the overall patient throughput. In this context, parallel imaging and compressed sensing techniques have been proposed to

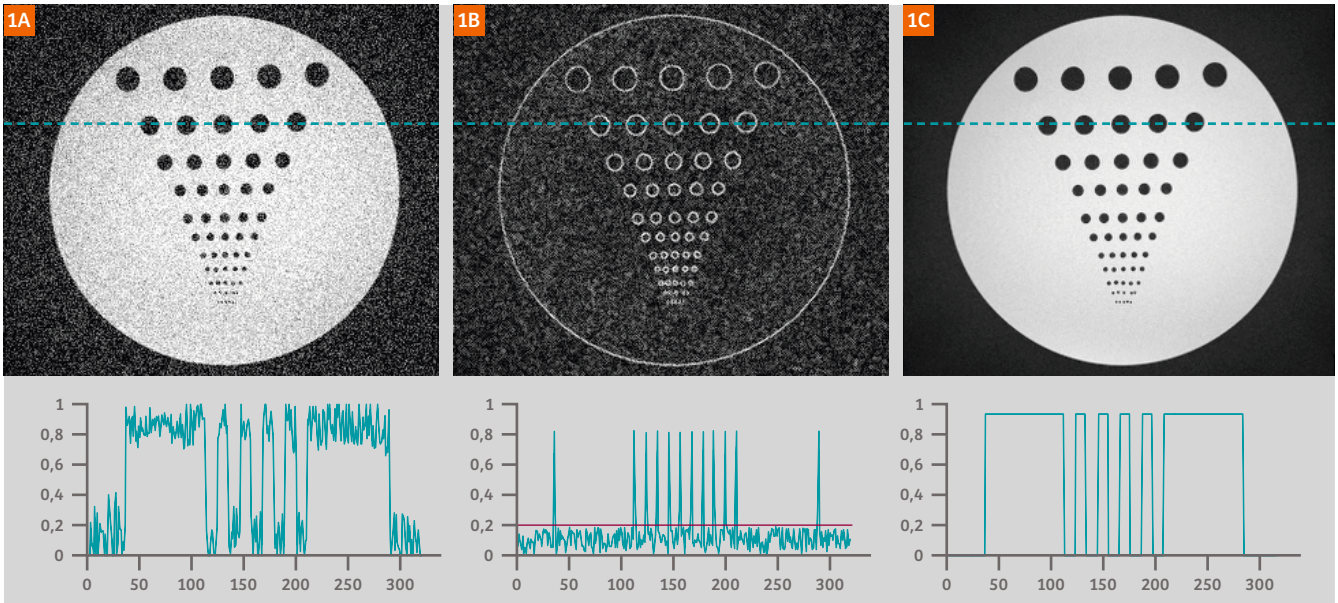

Figure 1: Additional noise reduces the homogeneity in the image of the resolution phantom **(1A),** which can also be observed in the line plot along the dashed line. After transformation into a sparse representation using finite differences **(1B),** the homogeneity can be restored by denoising, i.e., setting all pixels below a threshold level (red line) to 0. After the image is transformed back to its original domain, the phantom is piecewise constant **(1C).**

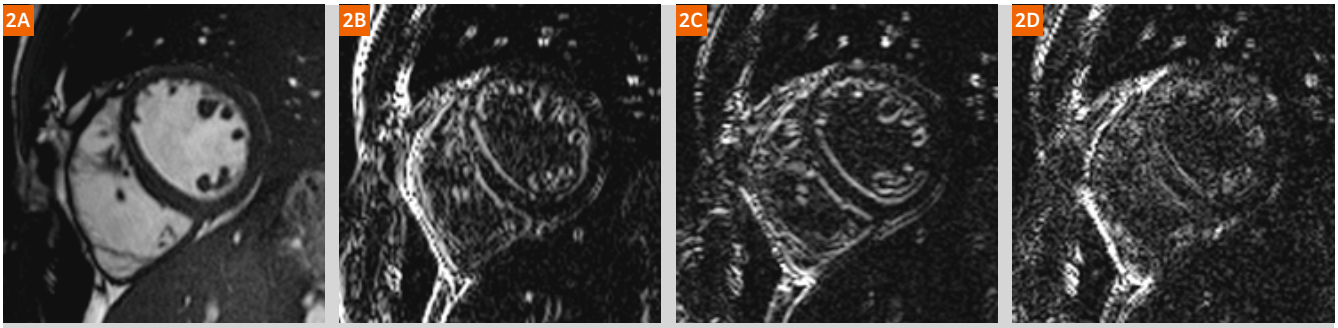

Figure 2: The short-axis view of the heart **(2A)** is transformed by the wavelet transform to achieve a sparse representation. In addition to the low-resolution representation of the original image, the wavelet transform results in three edge images **(2B–2D):** While **(2B)** and **(2C)** contain the edges in horizontal and vertical direction, respectively, Figure 2D shows the diagonal edge components of the image. In the wavelet domain, the content of the image is sufficiently described by only few coefficients, i.e. the bright pixels.

significantly speed up the acquisition time while maintaining diagnostic image quality.

Parallel imaging

Parallel imaging [1, 2] is well established in current clinical practice to speed up data acquisition in a large number of applications. With this technique, scan acceleration is usually achieved by uniformly sub-sampling *k*-space, for example, by skipping every other line. The resulting aliasing can be unfolded by incorporating the spatial encoding capabilities of multi-coil receiver arrays. However, the scan time reduction is often restricted to moderate acceleration factors between 2 and 4. This limitation is due to the restricted encoding capabilities in terms of number and position of the receiver coils. Additionally, acquiring less data also leads to a reduced signal-to-noise ratio (SNR).

Compressed sensing

In recent years, compressed sensing[1] has gained large scientific attention. Originally, it was proposed as a general concept to accurately reconstruct a signal from a small number of random measurements [3, 4]. A few years later, compressed sensing[1] was introduced to MRI [5] and successfully combined with parallel imaging [6, 7]. Exploiting the compressibility of medical images, this method promises to markedly exceed the acceleration rates that are feasible with parallel imaging. Although compressed sensing has denoising properties, it also has to deal with SNR loss from scan acceleration. Hence, possible acceleration factors scale with the native SNR of the scan. Up to now, the potential of compressed sensing has been shown in a large number of applications from 2D to 5D imaging [8–16].

The successful utilization of compressed sensing is a team play of data acquisition and image reconstruction. In the paper introducing compressed sensing to MRI, three criteria were identified as being essential to ensure successful image recovery from sub-sampled data [5]:

- First, the object that is acquired should have a *sparse representation* after conversion with a mathematical transformation.
- Second, *k*-space should be sub-sampled such that the aliasing results in *incoherent*, i.e. noise-like, artifacts in the image.
- Finally, image reconstruction requires a *nonlinear, iterative optimization* that simultaneously enforces a sparse representation of the resulting image. Thereby, it removes the noise-like artifacts, while it preserves its consistency to the acquired data.

These three essential requirements are discussed in detail below.

Transform sparsity

An image is considered as sparse when its informational content is represented by only a few pixels, while the contribution of the remaining majority of pixels is close to zero. In medical imaging, an angiogram provides a good example for such a sparse representation. However, in MRI, not all images are inherently sparse. But these images can also have a sparse representation utilizing a sparsifying transform. This transform provides an invertible mapping from an image to a sparse representation. Finite differences, i.e. images that contain only edge information, provide a simple technique to achieve a sparse representation, if the image is piecewise constant as shown in Figure 1. Discrete cosine transform and discrete wavelet transform are frequently used in the context of image compression, for example, in JPEG image compression. Utilizing such methods, images may be transformed into a sparse representation (see Fig. 2). In this domain, the content of the image is sufficiently described by only few coefficients, i.e. the bright pixels. The percentage of these pixels relative to the total number of pixels defines the sparsity of the image.

[1] 510(k)pending. Compressed Sensing Cardiac Cine is not commercially available. Future availability cannot be guaranteed.

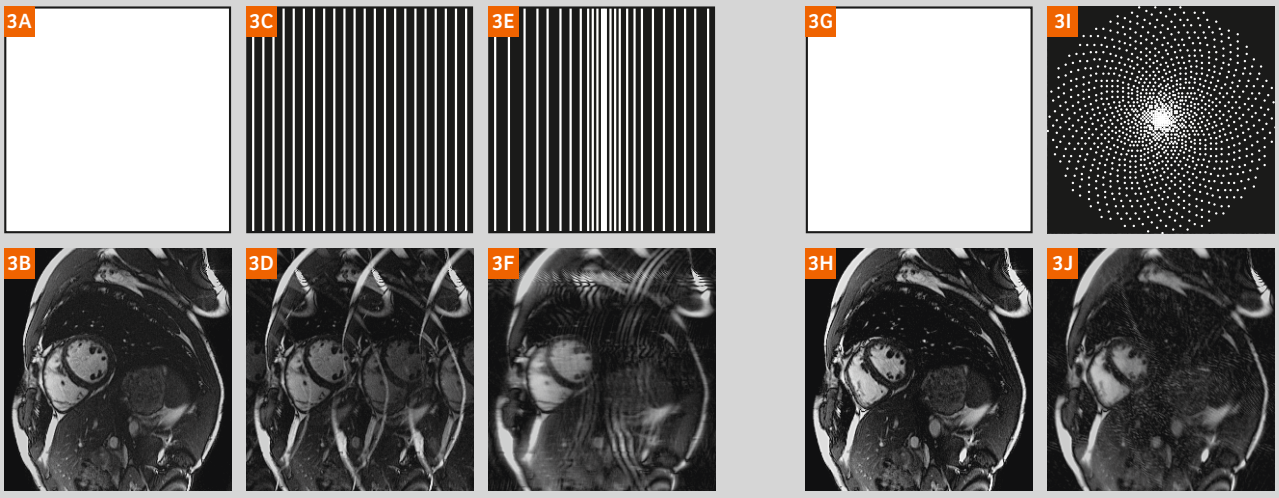

Figure 3: Examples of different sampling schemes, where *k*-space locations that are acquired are highlighted in white and the ones that are skipped are black (upper row) with corresponding image results and aliasing artifacts after Fourier transform (lower row). In 2D imaging, sub-sampling is limited to one phase-encoding direction whereas for 3D sub-sampling can be applied in two phase-encode directions. In case of CINE imaging, additional incoherence can be achieved in the temporal domain. **(3A, 3B)** Fully sampled *k*-space with artifact free result image; **(3C, 3D)** Regular subsampled *k*-space like PAT resulting in superposition of multiple ghosts; **(3E, 3F)** Irregular subsampled *k*-space as used in CS leading to incoherent aliasing artifacts similar to noise; **(3G, 3H)** Fully sampled *k*-space with artifact free result image; **(3I, 3J)** Irregular subsampled *k*-space as used in CS with noise-like artifacts.

For image compression, pixels in this sparse representation that are below a certain threshold can be set to zero, which facilitates a compression of the signal. Once the compressed signal is converted back to its initial domain, the visual difference between the resulting image and its original version is negligible. In particular, the discrete wavelet transform has been shown to be a suitable sparsifying transform for many natural images, including MRI images, and is commonly used in compressed sensing applications. In the case of dynamic imaging, including CINE imaging, this transform can also be applied in the temporal dimension. The redundancy of information along this temporal dimension can be exploited, and often the sparsity is even higher compared to the spatial dimensions.

Incoherent sampling

Unlike the regular sub-sampling patterns used for parallel imaging, the data acquisition process for compressed ensing requires that *k*-space sub-sampling is irregular (see Fig. 3C for regular and 3E, 3I for irregular sampling). In conventional Cartesian parallel imaging, regular sub-sampling of *k*-space is advantageous in that the phase-encoding gradient is increasing linearly during the measurement, which is beneficial for physical and MRI hardware limitation reasons. However, violating the Nyquist sampling theorem in this manner results in a superposition of shifted replicas of the original signal as illustrated in Figure 3D. The number of replicas equals the chosen sub-sampling rate. This aliasing can then be unfolded utilizing the spatial encoding capabilities of the multi-coil receiver array and parallel imaging. In contrast, irregular, incoherent sub-sampling of *k*-space, as required for compressed sensing, would result in a noise-like appearance of sub-sampling artifacts (see Figs. 3F, 3J). Theoretically, completely random sub-sampling is optimal to ensure this noise-like behavior. However, purely random sampling is impractical in the case of MRI. On the one hand, large and random steps in *k*-space may require large-amplitude gradient steps and should be avoided due to hardware limitations and physical reasons. On the other hand, the sampling trajectory must be repeatable to allow the same acquisition to be reproduced with consistent image quality. Therefore, sub-sampling patterns featuring deterministic properties that mimic random sampling within the given constraints are frequently used for compressed sensing data acquisition. In 2D Cartesian imaging with pure spatial coverage, the sub-sampling is limited to one dimension, as only the phase-encoding direction is sub-sampled in MRI. But in case of 2D dynamic imaging, the sampling pattern can be varied from one time frame to the next in order to maintain sufficient incoherence for compressed sensing. In 3D Cartesian imaging, sub-sampling can be applied in two phase-encoding directions. Alternatively, non-Cartesian sampling trajectories can be used, e.g., radial or spiral imaging, that already facilitate an incoherent sampling of *k*-space for 2D imaging.

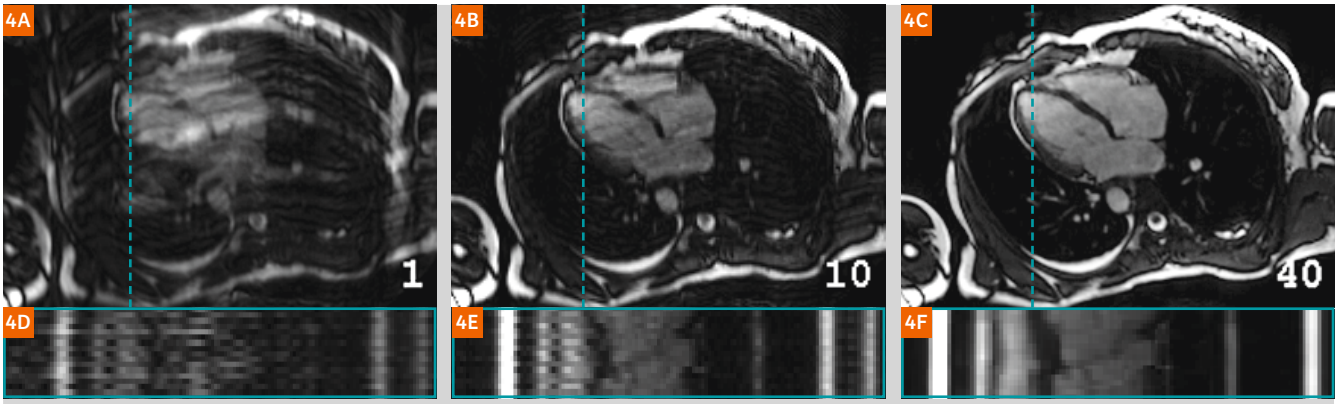

Figure 4: This Figure shows the progress of the optimization procedure to preserve data fidelity and reduce noise-like artifacts exemplarily in a Cardiac 2D CINE dataset **(4A–4C).** While the top image shows one image of the time series, a temporal profile along the dashed line is plotted below. The incoherent sub-sampling in the spatio-temporal domain results in incoherent artifacts that dominate the image after the first iteration **(4A).** Enforcing a sparse representation of the image and exploiting temporal redundancy, these artifacts are reduced with an increasing number of iterations **(4B).** The compressed sensing reconstruction is terminated after 40 iterations and results in an aliasing-free image **(4C).**

Nonlinear image reconstruction

If the two above-mentioned requirements are sufficiently met, the image can be recovered from the sub-sampled data by nonlinear, iterative reconstruction. In this reconstruction, a data fidelity term ensures consistency of the estimated image to the acquired data and a transform sparsity term enforces a sparse representation of the image in the transform domain by solving the following equation:

$$\min_x \underbrace{\|Ax - y\|_2^2}_{\text{data fidelity}} + \lambda \underbrace{\|\Phi(x)\|_1}_{\text{transform sparsity}}$$

The data fidelity term minimizes the least-squares difference ($\|\cdot\|_2^2$) between the estimated image, x, and the acquired *k*-space data, y. The system matrix, A, describes the data acquisition process, i.e., the transform from spatio-temporal to frequency domain, which is required for the comparison of the image and acquired data. Incorporating parallel imaging, it consists of the coil sensitivity maps of the individual receiver coil elements, the Fourier transform, and the applied sub-sampling pattern during data acquisition. In the transform sparsity term, the image is transformed into a sparse representation by $\Phi(\cdot)$, for example, using the discrete wavelet transform. In this term, the sum of the absolute values of the pixels in the transform domain, denoted by the ℓ_1 norm ($\|\cdot\|_1$), is minimized. Hence, the optimization procedure minimizing this equation seeks to find a solution that fulfills both criteria, data consistency and transform sparsity. This optimization procedure is more computationally intensive than conventional reconstruction, e.g., parallel imaging. The balance between data fidelity and sparsity is adjusted with the regularization parameter λ, which is usually found empirically. While small values of λ lead to an image that is closer to the acquired data, increasing this value tends to produce an image that is in favor of the sparse solution. When λ is too low, the image will be noisy, and when λ is too high a strongly filtered image appearance may be the consequence. The equation described above is iteratively minimized until a convergence criterion is met or a fixed number of iterations is reached. Figure 4 illustrates this optimization in the example of real-time CINE imaging of the heart.adverse surgical outcomes.

Transition into clinical routine

Compressed sensing acquisition and reconstruction have been completely integrated into our clinical MRI scanners. Works-in-progress packages have been developed and tested by our clinical cooperation partners world-wide for various applications in the fields of cardiovascular [17–20], neurological [21], musculoskeletal [22–24] and oncological [25] imaging. The additional parameters needed to compose the compressed sensing protocols, for both acquisition and reconstruction, have been seamlessly integrated into our user interface (UI). A selection of possible continuous acceleration factors takes the place of discrete numbers that were familiar from parallel imaging. This facilitates a UI experience with a low level of complexity. The award-winning algorithm for compressed sensing reconstruction [9], ranking first at the ISMRM 2014 "sub-Nyquist" reconstruction challenge, has been fully integrated into the Siemens image reconstruction environment. Without the need for additional hardware, the images are directly calculated inline utilizing the full computational power

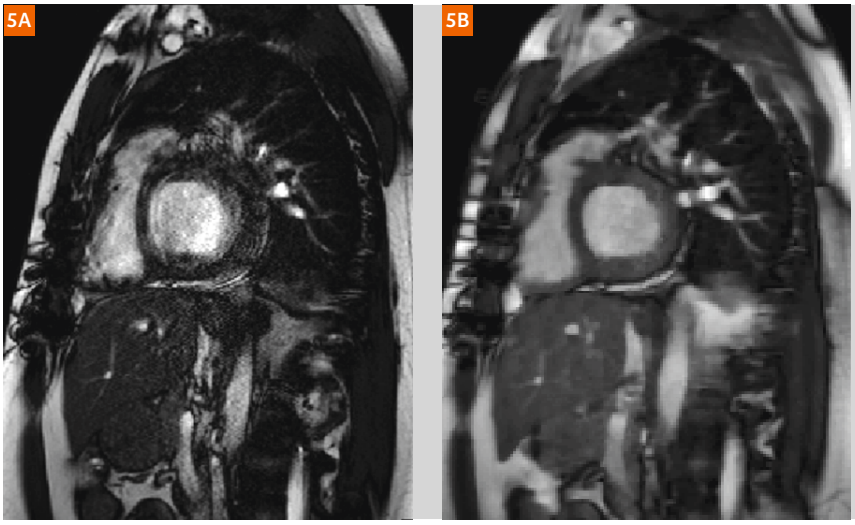

Figure 5: In cardiac imaging, the high acceleration rate due to compressed sensing enables real-time CINE imaging with a temporal and spatial resolution in a comparable range as conventional segmented acquisitions. While conventional imaging might fail in challenging scenarios, like in case of arrhythmia **(5A),** the compressed sensing real-time sequence preserves a diagnostic image quality that still enables the quantification of LV function **(5B).** *Images courtesy of Dr. François Pontana, Lille University Hospital, Lille, France.*

of the reconstruction computer. Compressed sensing reconstruction is performed on a graphics processing unit, which provides a significant speed-up in processing time. For example, the image series of one cardiac real-time CINE slice is processed in 10 to 15 seconds.

Thanks to its high acceleration rate due to compressed sensing, real-time sequences allow for a temporal and spatial resolution comparable to that of conventional segmented acquisitions. For example, compressed sensing in cardiac imaging permits fast quantification of left-ventricular (LV) function in a single breath-hold [26]. As demonstrated in Figure 5, this sequence still provides diagnostic images for LV function quantification even in challenging scenarios, such as in the presence of arrhythmia, where conventional sequences usually fail. This sequence may also be applied in free breathing, which is beneficial for patients who are not able to hold their breath sufficiently and, in general, allows for a simplified and more patient-friendly examination workflow.

Conclusion

Compressed sensing facilitates rapid MR imaging by exploiting the fact that medical images have a sparse representation in a certain transfer domain. Representing a team play of data acquisition and image reconstruction, this allows for the reconstruction of artifact-free images following incoherent data acquisition. The acceleration enables a reduction in the acquisition time or an improvement in the spatial and/or temporal resolution. Real-time imaging featuring compressed sensing helps to reduce the need for breath-holding or ECG triggering. The integration of protocols based on compressed sensing in clinical workflows allows a significant reduction in the examination time for each patient. Our generalized integration of compressed sensing in the scanner environment will allow for the straightforward introduction of further applications that are likely to come in the near future.

References

1 M. A. Griswold, P. M. Jakob, R. M. Heidemann, M. Nittka, V. Jellus, J. Wang, B. Kiefer, and A. Haase. “Generalized Autocalibrating Partially Parallel Acquisitions (GRAPPA)”. Magnetic Resonance in Medicine, Vol. 47, No. 6, pp. 1202–1210, June 2002.
2 K. Pruessmann, M. Weiger, M. B. Scheidegger, and P. Boesiger. “SENSE: Sensitivity Encoding for Fast MRI”. Magnetic Resonance in Medicine, Vol. 42, No. 5, pp. 952–962, Nov. 1999.
3 D. Donoho. “Compressed Sensing”. IEEE Transactions on Information Theory, Vol. 52, No. 4, pp. 1289–1306, Apr. 2006.
4 E. Candes and J. Romberg. “Sparsity and incoherence in compressive sampling”. Inverse problems, Vol. 23, No. 3, pp. 969–985, Apr. 2007.
5 M. Lustig, D. Donoho, and J. M. Pauly. “Sparse MRI: The Application of Compressed Sensing for Rapid MR Imaging”. Magnetic Resonance in Medicine, Vol. 58, No. 6, pp. 1182–1195, Dec. 2007.
6 D. Liang, B. Liu, J. Wang, and L. Ying. “Accelerating SENSE Using Compressed Sensing”. Magnetic Resonance in Medicine, Vol. 62, No. 6, pp. 1574–1584, Dec. 2009.
7 Block, K. T., Uecker, M. and Frahm, J., “Undersampled radial MRI with multiple coils. Iterative image reconstruction using a total variation constraint”, Magnetic Resonance in Medicine, Vol. 57, No. 6, pp. 1086-1098, May 2007.
8 G. Adluru, L. Chen, S. Kim, N. Burgon, E. G. Kholmovski, N. F. Marrouche, and E. V. R. DiBella. “Three-dimensional late gadolinium enhancement imaging of the left atrium with a hybrid radial acquisition and compressed sensing”. Journal of Magnetic Resonance Imaging, Vol. 34, No. 6, pp. 1465-1471, Dec. 2011.
9 J. Liu, J. Rapin, T.-C. Chang, A. Lefebvre, M. O. Zenge, E. Mueller, and M. S. Nadar. “Dynamic cardiac MRI reconstruction with weighted redundant Haar wavelets”. In: Proceedings of the 20th Annual Meeting of ISMRM, p. 4249, Melbourne, Australia, May 2012.
10 F. Han, S. Rapacchi, S. Kahn, I. Ayad, I. Salusky, S. Gabriel, A. Plotnik, J. P. Finn, and P. Hu, “Four-dimensional, multiphase, steady-state imaging with contrast enhancement (MUSIC) in the heart: A feasibility study in children”. Magnetic Resonance in Medicine, Vol. 74, No. 4, pp. 1042-1049, Oct. 2015.
11 S. T. Ting, R. Ahmad, N. Jin, J. Craft, J. Serafim da Silveira, H. Xue, and O. P. Simonetti. “Fast Implementation for Compressive Recovery of Highly Accelerated Cardiac Cine MRI Using the Balanced Sparse Model”. Magnetic Resonance in Medicine, doi: 10.1002/mrm.26224.

12 D. Stäb, T. Wech, F. A. Breuer, A. M. Weng, C. O. Ritter, D. Hahn, and H. Köstler, "High resolution myocardial first-pass perfusion imaging with extended anatomic coverage". Journal of Magnetic Resonance Imaging, Vol. 39, No. 6, pp. 1575–1587, Jun. 2014.
13 X. Chen, M. Salerno, Y. Yang, and F. H. Epstein, "Motion-compensated compressed sensing for dynamic contrast-enhanced MRI using regional spatiotemporal sparsity and region tracking: Block low-rank sparsity with motion-guidance (BLOSM)", Magnetic Resonance in Medicine, Vol. 72, No. 4, pp. 1028-1038, Oct 2014.
14 H. Xue, S. Inati, S. Sørensen, P. Kellman, and M. S. Hansen, "Distributed MRI Reconstruction Using Gadgetron-Based Cloud Computing", Magnetic Resonance in Medicine, Vol. 73, No. 3, pp. 1015-1025, March 2015.
15 J. Wetzl, F. Lugauer, M. Schmidt, A. Maier, J. Hornegger, and C. Forman. "Free-Breathing, Self-Navigated Isotropic 3-D CINE Imaging of the Whole Heart Using Cartesian Sampling", In: Proceedings of the 24th Annual Meeting of ISMRM, p. 411, Singapore, May 2016.
16 L. Feng, L. Axel, H. Chandarana, K. T. Block, D. K. Sodickson, and R. Otazo. "XD-GRASP: Golden-angle radial MRI with reconstruction of extra motion-state dimensions using compressed sensing". Magnetic Resonance in Medicine, Vol. 75, No. 2, pp. 775–788, Feb. 2016.
17 C. Forman, D. Piccini, R. Grimm, J. Hutter, J. Hornegger, and M.O. Zenge. "Reduction of respiratory motion artifacts for free-breathing whole-heart coronary MRA by weighted iterative reconstruction", Magnetic Resonance in Medicine, Vol. 73, No. 5, pp. 1885-1895, May 2015.
18 A. F. Stalder, M. Schmidt, H. H. Quick, M. Schlamann, S. Maderwald, P. Schmitt, Q. Wang, M. S. Nadar, and M. O. Zenge. "Highly undersampled contrast-enhanced MRA with iterative reconstruction: Integration in a clinical setting", Magnetic Resonance in Medicine, Vol. 74, No. 6, pp. 1652-1660, Dec. 2015
19 T. Yamamoto, K. Fujimoto, T. Okada, Y. Fushimi, A. Stalder, Y. Natsuaki, M. Schmidt, and K Togashi, "Time-of-Flight Magnetic Resonance Angiography With Sparse Undersampling and Iterative Reconstruction: Comparison With Conventional Parallel Imaging for Accelerated Imaging", Investigative Radiology, Vol. 51, No. 6, pp. 372-378, Jun 2016.
20 J. Wetzl, C. Forman, B. J. Wintersperger, L. D'Errico, M. Schmidt, B. Mailhe, A. Maier, and A. F. Stalder. "High-resolution dynamic CE-MRA of the thorax enabled by iterative TWIST reconstruction", Magnetic Resonance in Medicine, doi: 10.1002/mrm.26146.
21 E. Mussard, T. Hilbert, R. Meuli, J.-P. Thiran, and T. Kober. "Accelerated MP2RAGE Imaging Using Sparse Iterative Reconstruction", In: Proceedings of the 24th Annual Meeting of ISMRM, p. 4216, Singapore, May 2016.
22 R. Otazo, M. Nittka, M. Bruno, E. Raithel, C. Geppert, S. Gyftopoulos, M. Recht, and L. Rybak. "Sparse-SEMAC: Rapid and Improved SEMAC Metal Implant Imaging Using SPARSE-SENSE Acceleration", Magnetic Resonance Imaging, July 2016, Early View, DOI: 10.1002/mrm.26342.
23 J. Fritz, S. Ahlawat, S. Demehri, G.K. Thawait, E. Raithel, W.D. Gilson, M. Nittka. "Compressed Sensing SEMAC: 8-fold Accelerated High Resolution Metal Artifact Reduction MRI of Cobalt-Chromium Knee Arthroplasty Implants", Investigative Radiology, October 2016, Vol. 51, Issue 10, pp 666–676.
24 J. Fritz, E. Raithel, G. K. Thawait, W. Gilson, and D. F. Papp. "Six-Fold Acceleration of High-Spatial Resolution 3D SPACE MRI of the Knee Through Incoherent k-Space Under-sampling and Iterative Reconstruction – First Experience". Investigative Radiology, Vol. 51, No. 6, pp. 400-409, Jun 2016.
25 D. Nickel, X. Chen, B. Mailhe, Q. Wang, Y. Son, J. M. Lee, and B. Kiefer. "Motion-resolved 3D dynamic contrast enhanced liver MRI", In: Proceedings of the 24th Annual Meeting of ISMRM, p. 4253, Singapore, May 2016.
26 G. Vincenti, P. Monney, J. Chaptinel, T. Rutz, S. Coppo, M.O. Zenge, M. Schmidt, M.S. Nadar, D. Piccini, P. Chèvre, M. Stuber, and J. Schwitter, "Compressed Sensing Single–Breath-Hold CMR for Fast Quantification of LV Function, Volumes, and Mass" JACC: Cardiovascular Imaging, Vol. 7, No. 9, pp. 882–892, Sep. 2014.

Contact

Christoph Forman

Siemens Healthcare GmbH
HC DI MR PI TIO CARD

Postbox 32 60
91050 Erlangen
Germany
christoph.forman@siemens.com

For further information,
articles, case studies and keynotes
on the topic of Compressed Sensing
please visit

www.siemens.com/Compressed-Sensing

Exercise Cardiac MRI, a Clinical Reality with Compressed Sensing

Wendy Strugnell, BAppSc(MIT) FSMRT; Aaron Lin, MBChB, FRACP

Richard Slaughter Centre of Excellence in Cardiovascular MRI, The Prince Charles Hospital, Brisbane, Australia

Introduction

Non-invasive assessment of ventricular function plays an important role in the diagnosis and management of cardiac diseases. With its high temporal and spatial resolution, cardiac MRI is considered the most accurate non-invasive tool for providing left ventricular (LV) volumes, ejection fraction (EF) and mass at rest [1–3]. Cardiac MRI is also superior to other imaging modalities for quantitative assessment of the complexly shaped right ventricle (RV) [4–6].

Due to practical and technical limitations of imaging, clinical cardiac assessment is conventionally performed with the patient at rest. However, in many heart diseases, symptoms do not occur at rest and ventricular assessment during exercise is necessary to unmask ventricular dysfunction that is not apparent at rest. Despite recent technological advances across imaging modalities, assessment of dynamic ventricular response during exercise remains challenging. Until now, non-invasive quantitative cardiac assessment during exercise has been performed using echocardiography and nuclear scintigraphy, both of which have significant limitations, particularly in the assessment of the RV. As MRI is superior to other imaging modalities in accuracy and reproducibility of ventricular functional results at rest, there is a clinical need for a reliable MRI assessment of the heart during exercise.

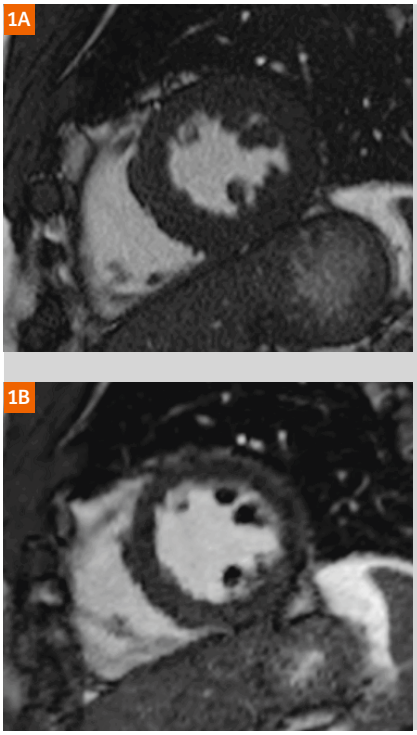

Figure 1: Midventricular short-axis images at end-distole from the conventional bSSFP acquisition (acceleration factor 2) **(1A)** and the high spatial and temporal resolution CS_ bSSFP acquisition (acceleration factor 8) **(1B),** from the same patient.

Limitations of cardiac MRI during exercise

Quantitative MRI assessment of cardiac function requires the acquisition of a stack of ECG-gated, cine ventricular short-axis images [5]. This time-consuming process requires multiple breath-holds to cover the entire ventricle and can be difficult for some patients to complete. This process can be made more challenging by exercise, particularly in patients with cardiac and pulmonary diseases whose baseline exercise and respiratory capacities are limited.

These limitations have driven the search for faster imaging techniques that maintain acceptable image quality and temporal resolution from resting heart rates through to accelerated heart rates during exercise. Real-time MRI is less susceptible to motion caused either by exercising or breathing and can be performed without ECG gating. La Gerche et al. [7] recently demonstrated that when real-time ungated MRI is combined with post hoc analysis incorporating compensation for respiratory motion, accurate biventricular volumes could be measured during maximal exercise. However, the methodology is labor intensive with lengthy post-processing times, and the authors acknowledge that there is significant difficulty in identifying the endocardium at higher levels of exercise. Access to commercially available processing software to enable analysis is another major limitation of this technique. Most real-time sequences also have low temporal resolution, which may affect accuracy at the high heart rates encountered during exercise. Clearly, the pursuit for a fast, clinically feasible MRI technique for evaluating the ventricles during exercise remains.

Compressed sensing MRI

Compressed sensing (CS)[1] was recently proposed as a means to considerably accelerate data acquisition through sparse sampling and reconstructing signals or images from significantly fewer measurements than were traditionally

[1] 510(k) pending. Compressed Sensing is not commercially available. Future availability cannot be guaranteed.

thought necessary [8, 9]. Using incoherent sparse sampling, nonlinear reconstruction algorithms and iterative processing, these methods reconstruct undersampled data from significantly fewer measurements whilst maintaining in-plane spatial resolution [10]. Cardiac MRI is ideally suited to CS techniques. Vincenti et al. [11] demonstrated that the application of CS to cardiac imaging enabled several-fold acceleration and achieved a cine acquisition of the whole heart in one breath-hold. With local institutional review board approval, we recently tested a prototype, ECG-triggered balanced steady-state free precession cine sequence with compressed sensing (CS_bSSFP)[1] (net acceleration of 8) against the conventional bSSFP sequence (net acceleration of 2) on clinical patients using comparable parameters for spatial and temporal resolution. We concluded that accurate and reproducible volumetric quantifications equaling those of conventional bSSFP could be achieved in the assessment of the left ventricle at rest in various cardiac disease states at significantly shorter acquisition times [12] (Fig. 1).

Exercise cardiac MRI

Patients with cardiac and pulmonary diseases typically have limited exercise tolerance and breath-hold capacity. Quantitation of ventricular function by cardiac MRI during exercise requires:

- Fast acquisition covering the whole ventricle to avoid fatigue from exercise (maximum total exercise time 15 minutes);
- Short duration of breath-holds to improve patient compliance and to minimize heart rate recovery during suspension of exercise;
- ECG gating to enable segmented data in discrete cardiac phases for ventricular analysis using commercially available software;
- Acceptable spatial resolution to delineate ventricular borders for analysis; and
- Sufficient temporal resolution for accurate determination of end-diastole and end-systole at high heart rates.

To meet all the above requirements, the prototype CS_bSSFP protocol was modified for use under exercise conditions. Typical imaging parameters are given in Table 1. A net acceleration factor of 11.5 was achieved which enables whole heart coverage in one or two breath-holds (5–7 s duration depending on heart rate), with in-plane spatial resolution of 2 mm2 and temporal resolution in the order of 20 ms. CS_bSSFP images in the LV short-axis (SAX) and modified RV SAX [13] are shown in Figure 2.

Exercise MRI protocol

Pre-MRI exercise testing
Prior to the exercise cardiac MRI, a cardiopulmonary exercise test (CPET) is performed outside the MRI room using a portable metabolic system (Metamax, Cortex BXB, Leipzig, Germany) and an MRI cycle ergometer (Lode, Groningen, The Netherlands). The maximal workload achievable

by the patient is determined and then used to calculate the sub-maximal workloads for exercise cardiac MRI. Typically, this is between 25–60 W.

During CPET, the patient is coached by the physiotherapist to hold their breath without valsalva breathing. This is to reduce the potential for intra-thoracic pressure increasing

	bSSFP	CS_bSSFP1
TR (ms)	3	2.53
TE (ms)	1.25	1
Field-of-view (mm)	380 x 290	380 x 312
Image Matrix	304 x 232	192 x 192
Spatial resolution (mm)	1.25 x 1.25	1.98 x 1.98
Temporal resolution (ms)	~30	~20
Slice thickness/gap (mm)	8 mm / 2 mm	8 mm / 2 mm
Flip angle (°)	70	70
Bandwidth (Hz/pixel)	914	898
Heartbeats per slice	14–20	1 or 2*
Cardiac phases	30	18–25*
ECG triggering	Retrospective	Prospective
Breath-holds	10	1 or 2*
Breath-hold duration (s)	10	5–7*

**Heart rate dependent*

Table 1: Imaging parameters of conventional bSSFP and CS_bSSFP1 sequences.

Figure 2: Midventricular LV short-axis and modified RV short-axis images from the highly accelerated CS_bSSFP acquisition (net acceleration 11.5) at end-diastole from the same patient.

during breath-hold, which in turn could cause reduced venous return and cardiac output.

MRI protocol
After a recovery period, the patient is positioned in the MRI scanner (1.5T, MAGNETOM Aera). ECG and blood oxygen saturation (SPO^2) monitoring is used throughout the examination under the supervision of a cardiologist. After cardiac localizers are obtained, both LV short axis and modified RV short axis stacks are acquired at rest and two pre-determined submaximal workloads (Rest: 0 W, Exercise 1: 25 W and Exercise 2: 40–60 W). In order to achieve steady-state exercise response, subjects cycle at each workload for 3 minutes prior to image acquisition. Between breath-holds, subjects resume cycling for 45 s to return to steady-state exercise response (Fig. 3).

Exercise MRI Analysis
Image analysis is performed off-line using cvi[42] software (Circle Cardiovascular Imaging, Calgary, Canada) and all standard measurements of cardiac function are obtained.

3

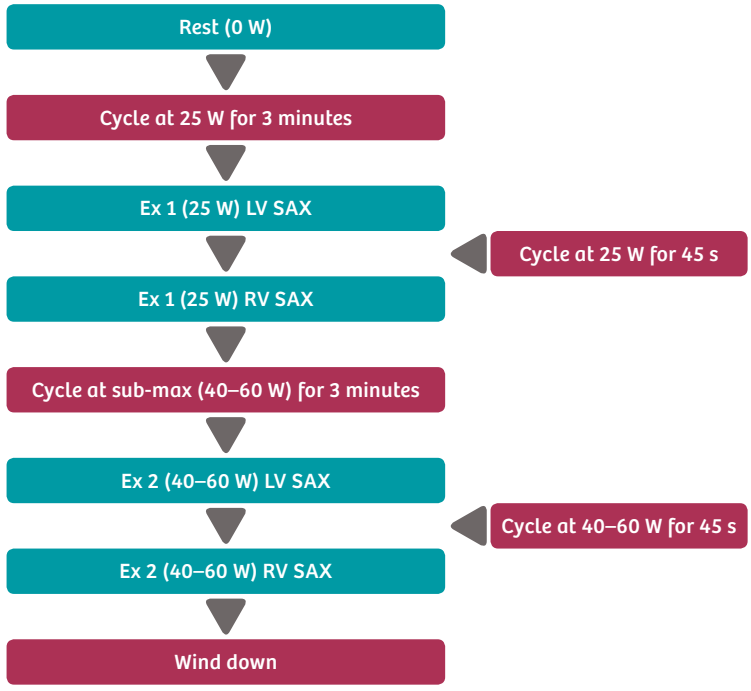

Figure 3: Exercise cardiac MRI study procedure.

Clinical feasibility

In pilot testing, we demonstrated that this exercise MRI protocol is feasible in patients, healthy controls and in well-trained athletes, with clinically acceptable image quality (Fig. 4). Exercise ergometry within the MRI scanner is well tolerated and breath-holds during image acquisition are achievable at submaximal exertion. Quantitative ventricular data and dynamic ventricular response during exercise can be determined using the ultrafast prototype CS_bSSFP sequence.

Clinical applications and potential

Insights from analysis of pressure-volume loops have demonstrated that a ventricle that adapts well is able to increase its contractility to match the chronic increase in afterload and its preservation is important in maintaining ventricular efficiency [14]. Ventricular systolic function adaptation to afterload can be tested dynamically to determine a contractile reserve, the capacity to increase contractility at a given level of loading. Contractile reserve has been shown to be a strong prognostic predictor in patients with left heart failure [15].

Assessment of RV function during exercise may provide an early indication of RV dysfunction and add incremental value in the clinical assessment of patients with right heart disease. In the setting of a chronic pressure overload state such as in pulmonary arterial hypertension (PAH), RV contractile reserve may be a more sensitive marker of hemodynamic ventricular dysfunction.

Currently, there is limited data on RV function during exercise and RV contractile reserve, largely due to the limitations of imaging during exercise. In a small study of pulmonary arterial hypertension (PAH) patients and normal controls, we demonstrated that although having near-normal ventricular function at rest, PAH patients were unable to increase their RV contractile function during exercise [16] (Fig. 5).

Exercise MRI also has the potential to predict adverse surgical outcomes in patients with congenital heart disease undergoing valve replacement surgery. The surgical outcome is likely to be better in patients with a ventricle shown to have contractile reserve. Exercise MRI may enable better-informed decisions about the timing of surgical and therapeutic interventions by detecting early ventricular impairment during exercise (particularly in the right ventricle). By providing information on ventricular contractile reserve, exercise MRI may facilitate improved prognostication of patients and has the potential to predict adverse surgical outcomes.

Conclusions

We have demonstrated that a highly accelerated imaging sequence using compressed sensing can facilitate clinically useful dynamic assessment of biventricular response during exercise with a reliability that was not previously possible.

4A
0 W – 70 bpm

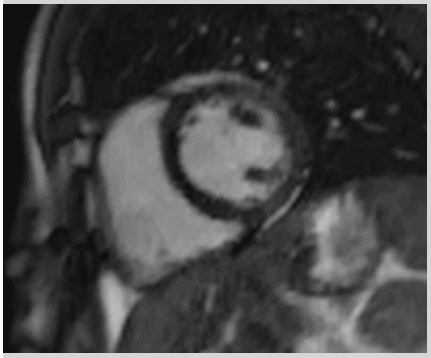

4B
25 W – 90 bpm

4C
60 W – 110 bpm

Figure 4A–C: Midventricular LV short-axis images at rest and two submaximal workloads at end-diastole using the CS_bSSFP acquisition in a male control.

4D
0 W – 60 bpm

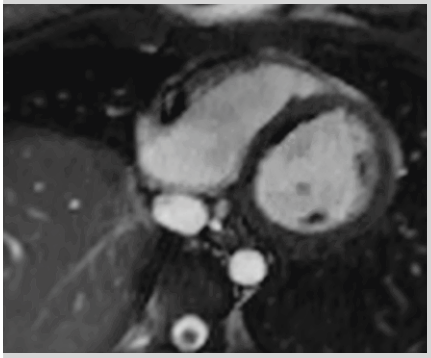

4E
25 W – 70 bpm

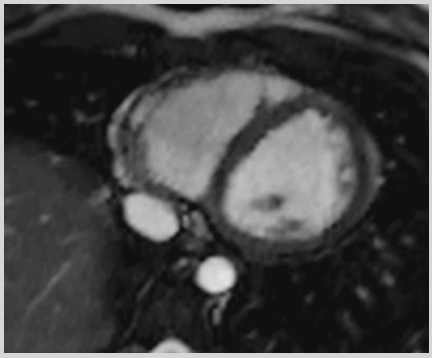

4F
60 W – 90 bpm

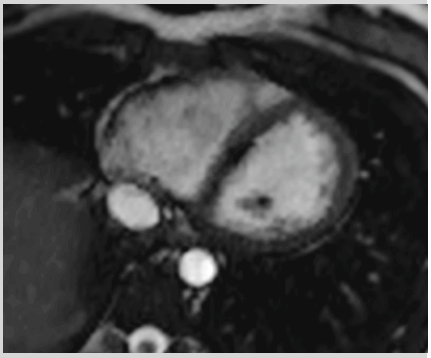

Figure 4D–F: Midventricular modified RV short-axis images at rest and two submaximal workloads at end-diastole using the CS_bSSFP acquisition in a female control.

5A
PAH vs Controls

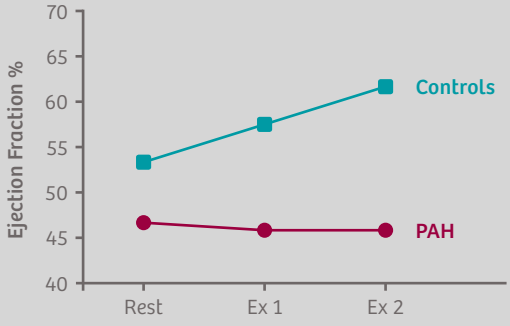

5B
Rest: 0 W

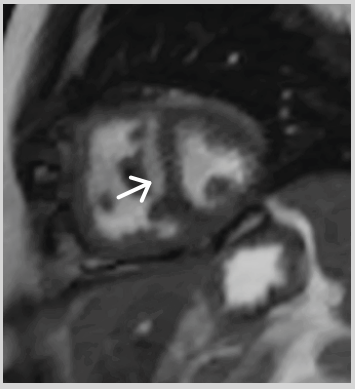

5C
Exercise: 40 W

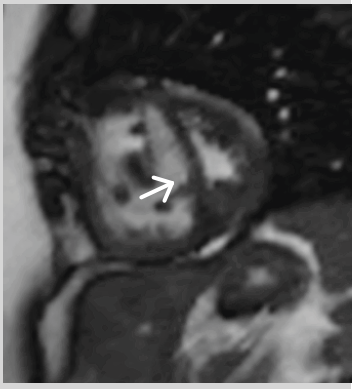

Early diastole

Figure 5A: Exercise MRI unmasks RV dysfunction not evident at rest in patients with pulmonary arterial hypertension (PAH): Despite having near-normal RV function at rest, PAH patients were unable to increase their RV contractile function during exercise.

Figure 5B,C: Midventricular LV short-axis images showing a left-ward deviation of the interventricular septum in early diastole during sub-maximal workload in a pulmonary arterial hypertension patient.

Acknowledgments

- Dr Benjamin Schmitt, Collaboration Manager & Scientific Team Leader MR, Siemens Healthcare ANZ, for technical support with CS sequence.
- Dr Richard Slaughter, Radiologist, for clinical advice and expertise.
- Mr Andrew Trotter for assistance with MR protocol development and clinical implementation.
- Professor Norman Morris and Ms Helen Seale (physiotherapists) for assistance with exercise protocol development and clinical implementation.
- The Prince Charles Hospital Foundation for support to purchase the MRI cycle ergometer and ongoing support for the exercise MRI program.
- Staff of the Richard Slaughter Centre of Excellence in Cardiovascular MRI for their continued support and dedication.

References

1 Grothues F, Smith GC, Moon JC, Bellenger NG, Collins P, Klein HU, et al. Comparison of interstudy reproducibility of cardiovascular magnetic resonance with two-dimensional echocardiography in normal subjects and in patients with heart failure or left ventricular hypertrophy. The American journal of cardiology. 2002;90(1):29-34.

2 Gardner BI, Bingham SE, Allen MR, Blatter DD, Anderson JL. Cardiac magnetic resonance versus transthoracic echocardiography for the assessment of cardiac volumes and regional function after myocardial infarction: an intrasubject comparison using simultaneous intrasubject recordings. Cardiovascular ultrasound. 2009;7:38.

3 Rayatzadeh H, Patel SJ, Hauser TH, Ngo LL, Shaw JL, Tan A, et al. Volumetric left ventricular ejection fraction is superior to 2-dimensional echocardiography for risk stratification of patients for primary prevention implantable cardioverter-defibrillator implantation. The American journal of cardiology. 2013;111(8):1175-9.

4 Jiang, L., Handschumacher, M.D., Hibberd, M.G., et al. (1994). Three-dimensional Echocardiographic Reconstruction of Right Ventricular Volume: In Vitro Comparison with Two-dimensional Methods. J. Am. Soc. Echocardiography. 7:150-158.

5 Pennell, D.J. (2002). Ventricular Volume and Mass by CMR. J. Cardiovasc. Magn. Reson. 4(4):507-513.

6 Niwa, K., Uchishiba, M., Aotsuka, H., Tobita, K., Matsuo, K., Fujiwara, T., Tateno, S., Hamada, H. (1996). Measurement of Ventricular Volumes by Cine Magnetic Resonance Imaging in Complex Congenital Heart Disease with Morphologically Abnormal Ventricles. Am. Heart Journal. 131(3):567-575.

7 La Gerche A, Claessen G, Van de Bruaene A, et al. Cardiac MRI: a new gold standard for ventricular volume quantification during high-intensity exercise. Circulation. Cardiovascular imaging. Mar 1 2013;6(2):329-338.

8 Donoho D. Compressed sensing. IEEE Transactions on Information Theory. 2006;Vol. 52:1289–1306.

9 Candes E, Romberg J, and Tao T. Robust uncertainty principles: Exact signal reconstruction from highly incomplete frequency information. IEEE Transactions on Information Theory. 2006;Vol. 52:489–509.

10 Lustig M, Donoho D, Pauly JM. Sparse MRI: The application of compressed sensing for rapid MR imaging. Magnetic resonance in medicine : official journal of the Society of Magnetic Resonance in Medicine / Society of Magnetic Resonance in Medicine. Dec 2007;58(6):1182-1195.

11 Vincenti G, Monney P, Chaptinel J, Rutz T, Coppo S, Zenge MO, et al. Compressed sensing single-breath-hold CMR for fast quantification of LV function, volumes, and mass. JACC Cardiovascular imaging. 2014;7(9):882-92.

12 Lin ACW, Strugnell WE, Riley R, Schmitt B, Zeng M, Schmidt M, et al. High Resolution Cine Imaging with Compressed Sensing for Accelerated Clinical Left Ventricular Evaluation. JMRI 2016 (under review/revision).

13 Strugnell WE, Slaughter RE, Riley RA, Trotter AJ, Bartlett H. Modified RV short axis series–a new method for cardiac MRI measurement of right ventricular volumes. Journal of cardiovascular magnetic resonance : official journal of the Society for Cardiovascular Magnetic Resonance. 2005;7(5):769-774.

14 Kuehne T, Yilmaz S, Steendijk P, et al. Magnetic resonance imaging analysis of right ventricular pressure-volume loops: in vivo validation and clinical application in patients with pulmonary hypertension. Circulation. Oct 5 2004;110(14):2010-2016.

15 Haddad F, Vrtovec B, Ashley EA, Deschamps A, Haddad H, Denault AY. The concept of ventricular reserve in heart failure and pulmonary hypertension: an old metric that brings us one step closer in our quest for prediction. Current opinion in cardiology. Mar 2011;26(2):123-131.

16 Lin ACW, Strugnell WE, Seale H, Schmitt B, Schmidt M, O'Rouke R, et al. Exercise Cardiac MRI Derived Right Ventriculo-Arterial Coupling Ratio Detects Early Right Ventricular Maladaptation in Pulmonary Arterial Hypertension. ERJ 2016 (in press).

Contact

Ms Wendy Strugnell

Richard Slaughter Centre of Excellence
in Cardiovascular Magnetic Resonance Imaging

The Prince Charles Hospital
627 Rode Rd
Chermside QLD 4032
Australia
Phone: +61-7-3139 6849
wendy.strugnell@health.qld.gov.au

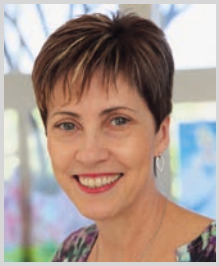

Wendy Strugnell

Aaron Lin

Cardiovascular Magnetic Resonance – an Effective Approach in Cardiology also Suitable for Very Sick Patients. Case Examples

Stephanie Funk, M.D.; Edyta Blaszczyk, M.D.; Agnieszka Toepper, M.D.; Jeanette Schulz-Menger, M.D.

Working Group Cardiac MRI, Experimental and Clinical Research Center, a cooperation between the Charité Medical Faculty and the Max-Delbrück Center for Molecular Medicine and HELIOS Clinic Berlin Buch, Department of Cardiology and Nephrology, Berlin, Germany

Background

Cardiovascular Magnetic Resonance (CMR) is able to provide unique information regarding myocardial tissue differentiation on top of a comprehensive examination of basic cardiac function. It is meanwhile included in as many as 29 guidelines of the European Society of Cardiology [1]. Nevertheless, it is not routinely used in all locations nor is its versatility exploited.

An obstacle faced by the CMR scan is the perception that it is difficult and lengthy. However, the development of more robust and faster techniques have significantly reduced the scan-time over recent years. Depending on the indication, a scan time can range between 5 and 45 minutes (see table 1). Of course, difficult cases, such as congenital heart disease, or unusual cases may take longer. Medical doctors often mistakenly believe that CMR is unsuitable for very sick patients even though it can provide unique information for further therapy guidance. However, recent developments allow CMR for patients unable to hold their breath as well as in arrhythmias, notably due to real-time- and motion-corrected imaging techniques. Currently, even though high-end image quality may be slightly impaired, most clinical requests can be covered. It is crucial here to focus on the clinical need of such patients as all areas of clinical practice are covered. Real-time cines are already available in clinical routine. Furthermore, multi-slice LGE images are available as non-breath-hold techniques. Motion-corrected perfusion imaging allows stress-perfusion in free-breathing.

Indication	Average scan time in minutes
Left and right ventricular function	5
Angiography	10
Inflammatory disease	20–30
Viability assessment	20–30
Adenosine perfusion	15–45
Valvular disorders	10–30
Cardiac masses	10–60
Congenital Heart Disease	20–60
Cardiomyopathies	20–60

Table 1: Average scan time in routine CMR indications.

There is no doubt that CMR can easily perform an assessment of coronary artery disease (CAD) in a well-standardized fashion [2]. However, a unique feature of CMR is that it can differentiate myocardial tissue, including the detection of irreversible changes such as necrosis, fibrosis and fat infiltration, as well as reversible injury such as edema. Quantitative parametric mapping techniques have added significantly to other contrast-enhanced and non-contrast-enhanced imaging techniques [3–5]. Back in 2009, the German Pilot phase of the EuroCMR-registry highlighted the high percentage of referrals due to non-ischemic cardiomyopathies (CMP) and inflammatory diseases [6], which was confirmed by our own data [7].

A relatively new technique allows the robust differentiation of fatty infiltration in fat/water separated images [8]. Very tiny fatty infiltrations are detectable in patients with muscular dystrophy. The sequence allows also the differentiation of bright signal as induced by fibrosis (LGE-imaging) and fat, which will hopefully bring the non-invasive tissue differentiation back in the guidelines of arrhythmogenic cardiomyopathies.

A significant advantage of CMR is that it enables the early detection of myocardial injury in preserved ejection fraction, allowing a decision on therapy to be taken sooner.

The following cases illustrate the potential speed of a CMR examination and its high-quality differentiation of tissue even in very sick patients. All scans were performed at a 1.5 Tesla MAGNETOM Avanto^{fit}.

Case 1: Muscular dystrophy

A 43-year-old man was referred to our university cardiologic outpatient clinic due to muscular dystrophy. He had been diagnosed with Limb-Girdle Muscular Dystrophy Type 2I by use of molecular genetic testing a couple of months previously.

Muscular dystrophy is a heterogeneous group characterized by progressive skeletal muscle wasting and weakness. Cardiac involvement is a frequently encountered finding in general, but currently not described in all entities. It may lead to life-limiting heart failure and arrhythmias in primary myopathies.

There is evidence that undetected arrhythmias in neuromuscular diseases cause earlier clinical impairment than other cardiac diseases. Therefore indications for device implantations in muscular dystrophies must be more rigorous than in other cardiac disorders. A sooner prophylactic implant of a cardioverter-defibrillator (ICD) is required because of the individual's high risk of sudden cardiac arrest [9].

Our patient was severely disabled, wheelchair-bound for 30 years and unable to take care of himself. He had partial movement in one hand only, enabling him to direct his fully electronic wheel chair. The biopsy of his skeletal muscles showed inclusion-body myositis.

The patient complained about palpitations. No syncope was reported. Echocardiography did not reveal any abnormalities, but due to his body size (BMI = 33.27 kg/m^2 BSA 2.34 m^2) and the upright position, ultrasound conditions were impaired. However, a 24-hour ECG revealed a short episode (five heart beats) of non-sustained VT (HF 150 beats per minute (bpm)). Apart from obesity, he had no risk factors for coronary artery disease (RR 130/90, no diabetes, non-smoker, cholesterol 158 mg/dl, LDL 52 mg/dl, no family history of early heart disease).

We performed a CMR to detect potential myocardial injury. The patient wasn't able to stay long in the scanner due to muscle pain, dyspnea and skeletal muscle contracture. His breath-holding capability was impaired.

The left ventricular function was normal (Figs. 1A, B as well as 2-chamber view cine in the online-data supplement).

However, extensive epicardial fat with subepicardial and intramural fatty replacement of the myocardium was detected. Application of fat-water separated imaging [8] allowed the differentiation of fat mimicking ibrosis in fibrosis imaging by LGE (Figs. 1C–H).

In principle, our patient qualified for an ICD implantation. But due to his co-morbidity and the severe fatty replacement of the myocardium, the decision was challenging. The patient was reluctant for any kind of surgery. Finally a loop-recorder was implanted pending a further decision.

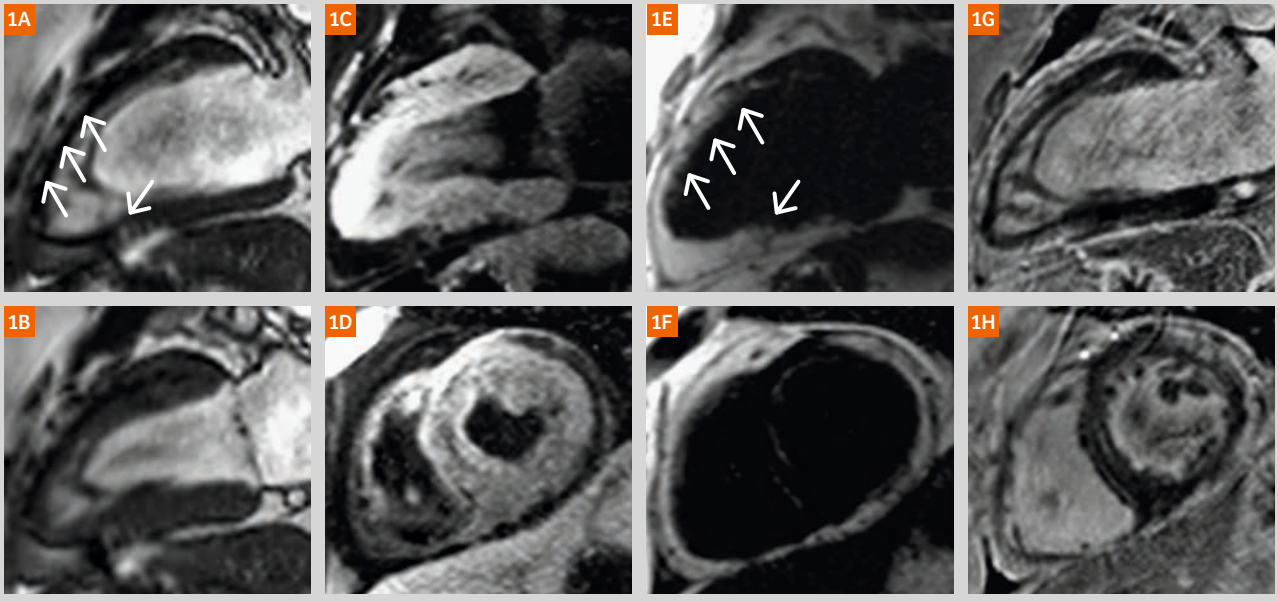

Figure 1: 43-year-old patient with Limb-Girdle Muscular Dystrophy Type 2I and normal LV function (LVEF 57%). Assessment of function and wall motion by cine Steady-State Free Precession (SSFP) in 2-chamber view in end-diastole **(1A)** and end-systole **(1B)** with no wall motion abnormality, but with already visible myocardium structure abnormality (arrows).

Tissue differentiation: All following images are given in the 2-chamber view and in a midventricular short axis. Fat/water imaging shows extensive epicardial fat with subepicardial and intramural fatty replacement of the myocardium in bright **(1C, D)** and accordingly dark signal (arrows) **(1E, F).** Fibrosis imaging (LGE) shows a bright signal indicating scar and fatty replacement **(1G, H).** Only the combination of LGE and fat imaging allows the differentiation of tissue character.

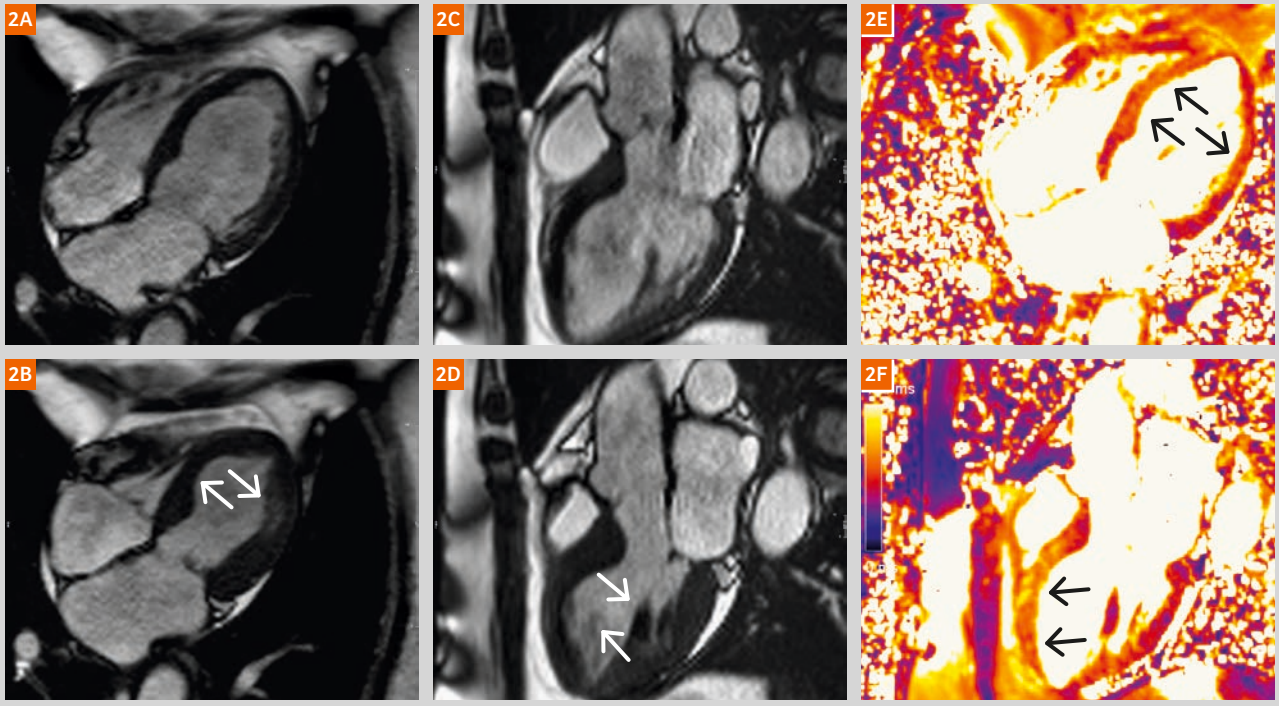

Figure 2: 71-year-old patient with takotsubo cardiomyopathy. Assessment of function and regional wall motion abnormalities using cine-SSFP showing 4-chamber view in end-diastole **(2A)** and end-systole **(2B)** as well as 3-chamber view in end-diastole **(2C)** and end-systole **(2D)** showing the midventricular akinesia (arrows).

Tissue differentiation: Assessment of edema applying T2 mapping showing the T2 maps of the 4-chamber view **(2E)** and 3-chamber view **(2F)**. Regional edema can be detected as it has longer T2 times (75 ms) (arrows).

Case 2: Takotsubo cardiomyopathy

A 71-year-old female patient was admitted to the intensive care unit (ICU) after experiencing left-sided hemiplegia caused by a brain tumor. The newly diagnosed tumor was a metastasis of a sigmoid adenocarcinoma.

Initially, the patient presented with tachycardia and elevated troponin T. The ECG showed negative T-waves indicating a myocardial injury.

A CMR was performed for myocardial tissue differentiation including inflammation. As the patient had increasing difficulties with the repeated breath-holding, the examination had to be fast, yet precise. Therefore, for inflammatory assessment, T2 mapping replaced T2-weighted imaging, since T2 mapping is shorter and less sensitive to motion-artifacts.

Breath-held late enhancement images for fibrosis imaging were not diagnostic. As the patient could not hold her breath repeatedly, artifacts occurred. Thus we used multi-sliced non-breath-hold sequences.

The patient had a mid-range reduced ejection fraction with a midventricular akinesia septal and lateral (Figs. 2A–D). In the area of the wall motion abnormalities an edema was detectable (Figs. 2E, F). As a potential sign of inflammatory reaction the patient also showed pleural effusion. This, however, could also have been a sign of the volume loading administered at the ICU.

There was no fibrosis in the late gadolinium-enhancement images.

We diagnosed an inverse takotsubo cardiomyopathy (TTC) with midventricular akinesia and edema. The stressor in this case was probably the cerebral tumor. As previously described, certain cerebral disorders, especially subarachnoid hemorrhage, can induce TTC [10, 11]. An edema in the region of a large wall motion abnormality without any focal fibrosis is a typical finding of TTC [12].

CMR is able to detect inflammatory reactions even in very sick patients using these techniques. The lack of scar in a region with a large wall motion abnormality is prognostically-relevant information and helps to guide patients in an early stage of disease.

Case 3: Suspicion for acute myocarditis

A 70-year-old male patient was referred to the MR-Unit from the ICU of an external hospital with heart failure symptoms with congestion and pneumonia. He presented with an AV-dissociation with a high escape rhythm and was supported by a temporary pacemaker.

Coronary artery disease was ruled out in the external hospital. Heart failure and rhythm problems despite lack of coronary heart disease were suggestive for myocarditis as the most presumptive cause and he was admitted to confirm the diagnosis.

The temporary pacemaker could be removed for the scan as the patient presented with high escape rhythm with heart frequency between 40–50 bpm, and an experienced cardiologist performed the scan. The pacemaker lead was taken away directly before the scan and the patient was monitored by ECG, POX and O_2-saturation. The latter was between 80% and 90%. Due to pneumonia he was supported by oxygen. Despite this support he was not able to follow the breath-hold commands. CMR was therefore conducted in free-breathing and the standard techniques had to be replaced.

Instead of steady-state free precession cine (Fig. 3A) we used real-time cine sequences (Fig. 3B) to assess left ventricular function. T2 mapping was used instead of T2-weighted images for the evaluation of edema (Figs. 3C, D). For the detection of scars and fibrosis, post-contrast T1 mapping (Figs. 3E, F) and a multi-slice free breathing protocol (Fig. 3G) were used. A breath-held PSIR (Fig. 3H) showed too many artifacts.

The examination was performed without complications.

A dilated left ventricle with a slightly reduced systolic function was diagnosed. The T2 maps showed prolonged times septal and inferoseptal (67 ms) being suggestive of an edema in these areas (Figs. 3C, D). There were multiple focal fibrosis, but none in the region of the described edema. As the patient had suffered a myocarditis years before, the fibrosis was defined as a sign of this previous myocarditis. However, the edema suggested an additional ongoing inflammation.

The interim finding was that the arrhythmia could be caused by the old scar or by the active inflammation. As the patient was suffering from pneumonia with a myocardial involvement, the decision was to wait until recovery from pneumonia and then to decide about a pacemaker implantation.

Case 4: Suspicion of coronary artery disease

A 42-year-old female with shortness of breath and atypical thoracical pain was referred to the MR-Unit for adenosine stress CMR to exclude significant coronary artery disease. She had a known X-ray contrast media allergy and a chronic fatigue syndrome (not able to perform ergometric testing). Due to claustrophobia-related self-premedication with

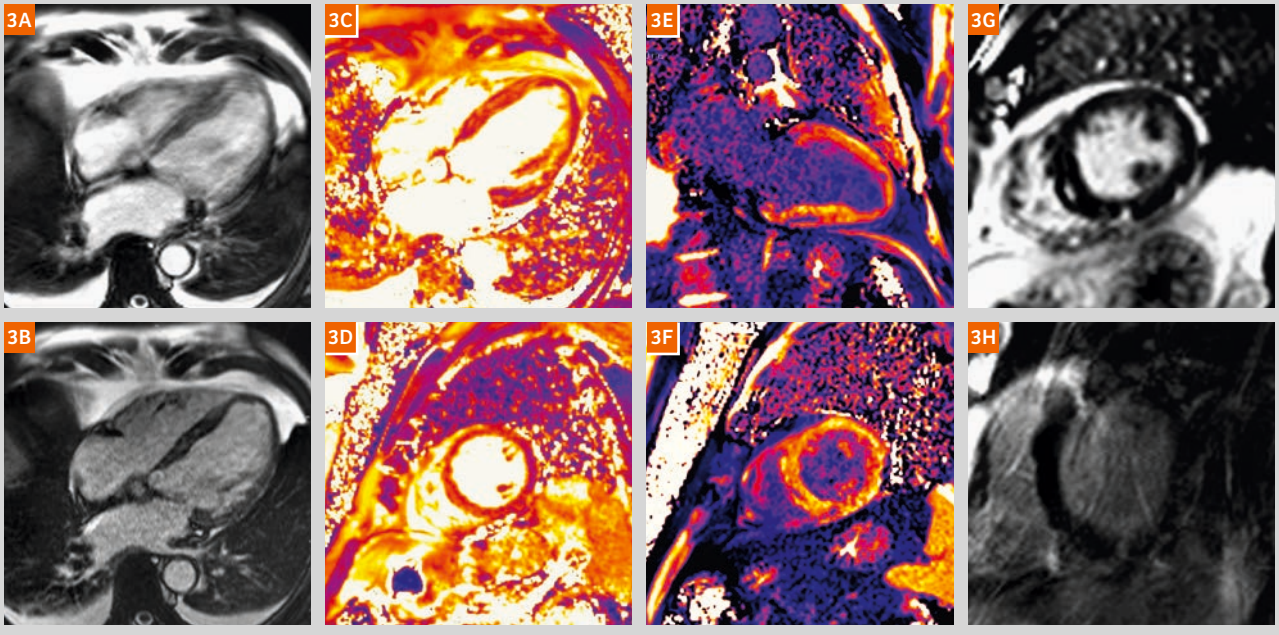

Figure 3: 70-year-old male patient with suspicion for acute myocarditis. He had a temporary pacemaker due to AV dissociation, which was removed for the examination. He was not able to hold his breath and his heart rate was 50 bpm. Segmented cine SSFP were not sufficient **(3A),** real cine time technique was applied **(3B)** showing LV dilatation and slightly reduced LV function (47%).

Tissue differentiation: T2 mapping showed prolonged times (67 ms) being suggestive of an edema in these areas **(3C, D).** T1 mapping **(3E, F)** was increased (1050 ms) indicating fibrosis. Free-breathing focal fibrosis imaging (LGE) was performed after single dose contrast application using overview technique **(3G),** as breath-held PSIR failed **(3H).**

4A

Scan protocol

Localiser	Function LAX	Stress perfusion	Function SAX	LGE overview
1 min	3 min	6 min	4 min	1 min

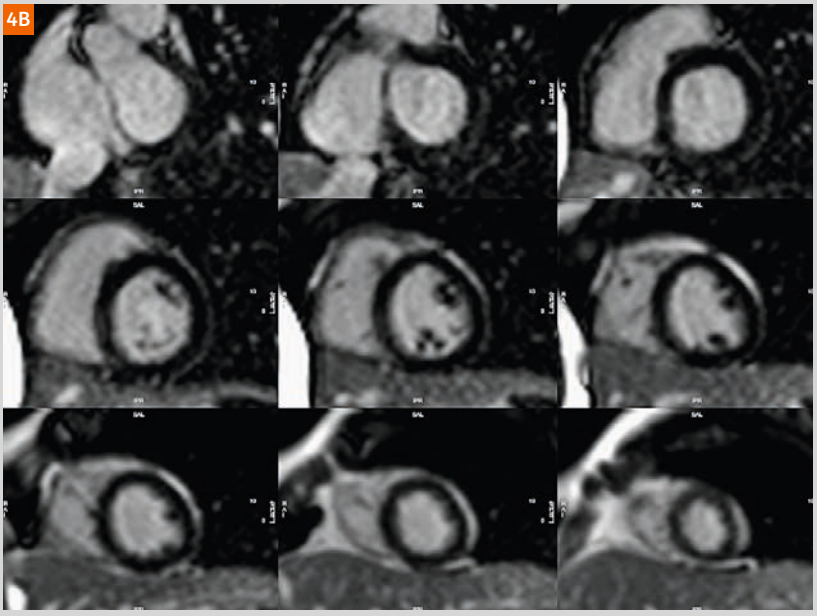

Figure 4:
42-year-old female patient with suspicion of coronary artery disease and severe claustrophobia was referred for exclusion of CAD based on an intermediate pre-test probability. She received a shortened adenosine protocol **(4A).** Scan time: approximately 15 minutes. Her anatomy did not allow a stress echo-cardiography and due to her age ionizing radiation was avoided. In the non-breath-hold stress perfusion with motion correction **(4C)** ischemia could be ruled out. The non-breath-hold late gadolinium enhancement technique showed no fibrosis or scar **(4B).**

cumulative 20 mg diazepam oral and an ongoing anxiety she was not able to follow the breathing instructions. The MRI protocol was shortened to the essential steps as follows: localizer, cardiac function (long axis), adenosine stress, cardiac function (short axis) and LGE in overview technique (multi-slice, free-breathing) after a single dose of contrast media application. The whole examination in free-breathing was completed in 15 minutes (Fig. 4A).

In the examination we saw neither signs of cardiac ischemia nor any fibrosis or scars (Figs. 4B, C). Therefore, we could rule out a coronary heart disease.

Conclusion

We perform over 3,000 clinical and research CMR examinations per year, mainly at one 1.5T scanner on in- and out-patients alike. Both groups include patients with arrhythmias including atrial fibrillation. In nearly all of them we reach diagnostic image quality. The in-patients are significantly sicker. The preparation of ICU-patients is more time-consuming, but the scan-time is usually shorter since we focus heavily on the main questions. CMR often helps with further therapy guidance, especially for very sick patients with inconclusive findings from routine assessment.

There is a strong need for fast and robust techniques. Standardized protocols are an excellent base for a dedicated and focused scan.

At the last SCMR board meeting the view was expressed that CMR will give more definitive, relevant, and actionable answers than other non-invasive imaging techniques. A CMR exam provides comprehensive information and has superior diagnostic and prognostic power, without the need for radiation.

Furthermore, there are CMR-only capabilities including virtual heart biopsy, high-resolution perfusion imaging and advanced blood flow analysis. This also applies for sick patients.

References

1 von Knobelsdorff-Brenkenhoff F, Schulz-Menger J. Role of cardiovascular magnetic resonance in the guidelines of the European Society of Cardiology. Journal of cardiovascular magnetic resonance: official journal of the Society for Cardiovascular Magnetic Resonance. 2016;18:6. doi: 10.1186/s12968-016-0225-6. PubMed PMID: 26800662; PubMed Central PMCID: PMC4724113.

2 Kramer CM, Barkhausen J, Flamm SD, Kim RJ, Nagel E, Society for Cardiovascular Magnetic Resonance Board of Trustees Task Force on Standardized P. Standardized cardiovascular magnetic resonance

(CMR) protocols 2013 update. Journal of cardiovascular magnetic resonance : official journal of the Society for Cardiovascular Magnetic Resonance. 2013;15:91. doi: 10.1186/1532-429X-15-91. PubMed PMID: 24103764; PubMed Central PMCID: PMC3851953.

3 Moon JC, Messroghli DR, Kellman P, Piechnik SK, Robson MD, Ugander M, et al. Myocardial T1 mapping and extracellular volume quantification: a Society for Cardiovascular Magnetic Resonance (SCMR) and CMR Working Group of the European Society of Cardiology consensus statement. Journal of cardiovascular magnetic resonance : official journal of the Society for Cardiovascular Magnetic Resonance. 2013;15:92. doi: 10.1186/1532-429X-15-92. PubMed PMID: 24124732; PubMed Central PMCID: PMC3854458.

4 Bulluck H, Maestrini V, Rosmini S, Abdel-Gadir A, Treibel TA, Castelletti S, et al. Myocardial T1 mapping. Circulation journal : official journal of the Japanese Circulation Society. 2015;79(3): 487-94. doi: 10.1253/circj.CJ-15-0054. PubMed PMID: 25746524.

5 Wassmuth R, Schulz-Menger J. Cardiovascular magnetic resonance imaging of myocardial inflammation. Expert review of cardiovascular therapy. 2011;9(9):1193-201. doi: 10.1586/erc.11.118. PubMed PMID: 21932962.

6 Bruder O, Schneider S, Nothnagel D, Dill T, Hombach V, Schulz-Menger J, et al. EuroCMR (European Cardiovascular Magnetic Resonance) registry: results of the German pilot phase. Journal of the American College of Cardiology. 2009;54(15):1457-66. doi: 10.1016/j.jacc.2009.07.003. PubMed PMID: 19682818.

7 von Knobelsdorff-Brenkenhoff F, Bublak A, El-Mahmoud S, Wassmuth R, Opitz C, Schulz-Menger J. Single-centre survey of the application of cardiovascular magnetic resonance in clinical routine. European heart journal cardiovascular Imaging. 2013;14(1):62-8. doi: 10.1093/ehjci/jes125. PubMed PMID: 22736714.

8 Kellman P, Hernando D, Arai AE. Myocardial Fat Imaging. Current cardiovascular imaging reports. 2010;3(2):83-91. doi: 10.1007/s12410-010-9012-1. PubMed PMID: 20401158; PubMed Central PMCID: PMC2850992.

9 European Society of C, European Heart Rhythm A, Brignole M, Auricchio A, Baron-Esquivias G, Bordachar P, et al. 2013 ESC guidelines on cardiac pacing and cardiac resynchronization therapy: the task force on cardiac pacing and resynchronization therapy of the European Society of Cardiology (ESC). Developed in collaboration with the European Heart Rhythm Association (EHRA). Europace: European pacing, arrhythmias, and cardiac electrophysiology: journal of the working groups on cardiac pacing, arrhythmias, and cardiac cellular electrophysiology of the European Society of Cardiology. 2013;15(8):1070-118. doi: 10.1093/europace/eut206. PubMed PMID: 23801827.

10 Finsterer J, Wahbi K. CNS disease triggering Takotsubo stress cardiomyopathy. International journal of cardiology. 2014;177(2): 322-9. doi: 10.1016/j.ijcard.2014.08.101. PubMed PMID: 25213573.

11 Abd TT, Hayek S, Cheng JW, Samuels OB, Wittstein IS, Lerakis S. Incidence and clinical characteristics of takotsubo cardiomyopathy post-aneurysmal subarachnoid hemorrhage. International journal of cardiology. 2014;176(3):1362-4. doi: 10.1016/j.ijcard.2014.07.279. PubMed PMID: 25125015.

12 Eitel I, Lucke C, Grothoff M, Sareban M, Schuler G, Thiele H, et al. Inflammation in takotsubo cardiomyopathy: insights from cardiovascular magnetic resonance imaging. European radiology. 2010;20(2):422-31. doi: 10.1007/s00330-009-1549-5. PubMed PMID: 19705125.

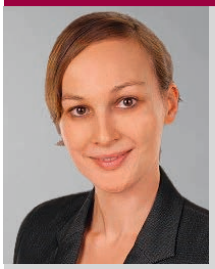

Stephanie Funk

Edyta Blaszczyk

Agnieszka Toepper

Jeanette Schulz-Menger

Contact

Professor Dr. Jeanette Schulz-Menger

University Medicine Berlin,
Charité Campus Buch, ECRC

HELIOS Clinics Berlin Buch,
Department for Cardiology and Nephrology

Schwanebecker Chaussee 50
13125 Berlin
Germany
Phone: +49 30 040153536
jeanette.schulz-menger@charite.de

Stress-Mapping for the Assessment of Myocardial Ischemia: New Potential Clinical Applications of Parametric Mapping

Juliano L. Fernandes, M.D., Ph.D., MBA[1]; Vanessa M. Ferreira, SB, M.D., D.Phil., FRCPC[2]; Stefan K. Piechnik, M.Sc.E.E., Ph.D. (Cantab) D.Sc.[3]

[1] Research Physician, Jose Michel Kalaf Research Institute, Cardiologist, Radiologia Clinica de Campinas, Campinas, Brazil
[2] Deputy Clinical Director, Oxford Centre for Clinical Magnetic Resonance Research, Associate Professor of Cardiovascular Medicine, Honorary Consultant Cardiologist, Division of Cardiovascular Medicine, Radcliffe Department of Medicine, University of Oxford, John Radcliffe Hospital, Oxford, Oxfordshire, UK
[3] Head of Advanced Cardiovascular Imaging Analysis, Associate Professor of Biomedical Imaging, Oxford Centre for Clinical Magnetic Resonance Research, Division of Cardiovascular Medicine, Radcliffe Department of Medicine, University of Oxford, John Radcliffe Hospital, Oxford, Oxfordshire, UK

Abstract

Parametric mapping has been used to differentiate common pathological changes in the myocardium at rest, with identification of variations in the extracellular compartments of the heart. While most of the interest has been drawn to studying interstitial changes of the myocardium, these techniques also allow us to study the physiology and pathology associated with the intravascular compartment of the extracellular space. Sensitive to changes in myocardial blood volume and flow, as well as oxygen extraction fraction and possibly oxygen consumption rate, quantitative mapping has potential new clinical applications waiting to be explored. With the addition of pharmacologic vasodilation, stress and rest T1 mapping has been shown to be useful in differentiating ischemic, infarcted and normal myocardium, as well as in assessing coronary vasodilatory reserve in patients without significant coronary artery disease. T2 mapping, based on previous oxygenation-sensitive cardiovascular magnetic resonance studies using relative signal intensity changes, may allow direct quantification of myocardial demand and confirmation of pharmacological vasodilation before contrast injection. Stress-mapping may allow for new and complimentary information to be extracted in addition to current protocols used in clinical cardiovascular magnetic resonance, without the need for gadolinium-based contrast agents (GBCA).

Introduction

Parametric mapping evaluation of the heart has developed significantly over recent years, allowing for direct quantitative measurement of myocardial T1, T2 and T2* [1]. Since the introduction of the first high-resolution pulse sequences for cardiac mapping, the focus of most studies has been directed at analyzing the underlying tissue composition and structure of the myocardium and extracellular space, using these parameters as surrogate markers for diffuse fibrosis, collagen, amyloid, edema, iron and fat deposition [2]. Despite the important clinical applications developed from these studies, T1 and T2 relaxation times also reflect the intravascular components of blood in the myocardium: myocardial blood flow (MBF) and volume regulation by exercise or pharmacologically induced vasodilation and capillary recruitment may change the extracellular water content or relative amounts of deoxyhemoglobin, thereby altering these mapping parameters.

Key points

1. Stress-mapping using current T1 and T2 parametric mapping sequences allows for assessment of myocardial tissue during stress, reflecting changes in the myocardial intravascular components.
2. Native T1 mapping has been shown to differentiate ischemic, infarcted and normal myocardium after stress without the need for gadolinium-based contrast agents.
3. T2 mapping might be useful to investigate myocardium oxygenation-sensitive changes during stress, with potential applications for identifying the effectiveness of pharmacological vasodilation and possible areas of ischemia.

Most studies with parametric mapping of the heart have been performed during rest conditions when the impact of the above factors may not have a significant influence on the measured relaxation times at rest. However, after vasodilation, myocardial blood volume (MBV), which constitutes only approximately 10% of the total myocardial volume at rest [3], may double with maximal blood flow [4, 5]. Along with changes in MBV, oxygen extraction fraction (OEF) is also significantly affected by vasodilation, with up to a 70% difference observed with hyperemia [6, 7], resulting in reduced deoxyhemoglobin concentration. MBV and MBF

	Rate-Pressure Product	MBF	MBV	OEF	MVO_2
Difference from resting conditions	40% to 60%	200% to 300%	30% to 100%	-40% to -70%	30% to 60%

CMR = cardiovascular magnetic resonance; MBF = myocardial blood flow; MBV = myocardial blood volume; OEF = oxygen extraction fraction; MVO_2 = oxygen consumption ratio

Table 1: Effects of pharmacological vasodilation on myocardial parameters measured by CMR.

(variables relating to myocardial oxygen supply) together with OEF and oxygen consumption rate (MVO_2) (relating to myocardial oxygen demand) have been estimated by CMR non-invasively using different techniques and validated against other methods, with significant changes during stress conditions (Table 1) [6–10].

Prior publications have demonstrated the early use of parametric techniques to assess the effects of vasodilatory stress in the myocardium [6, 11–15]. These older techniques lacked current technology employed in recent mapping sequences, and suffered from lower spatial resolution, longer acquisition times and significant susceptibility artifacts. The use of more recent parametric mapping sequences to assess changes in myocardial supply and demand variables during stress imaging is a fairly new development [16–19]. In the next sections, we will discuss some of the potential applications of T1 and T2 stress-mapping and current clinical scenarios in which these techniques may be applied.

Adenosine stress and rest myocardial T1 mapping

What is T1 mapping?

T1 (or spin-lattice) relaxation time is a magnetic resonance property that describes how quickly the longitudinal component of magnetization returns to thermal equilibrium. In simple systems, this process may be defined mathematically using Bloch equations in an idealized manner. Although basic Bloch equations may not completely characterize the complexity of living tissues and their *in vivo* environment, T1 relaxations times may be measured for the purpose of quantitative tissue characterization.

Measured T1 relaxation times may be affected by intrinsic tissue properties and its extrinsic environment, depending on the chosen method. As in most quantitative approaches, each tissue type is expected to have a normal range of T1 values, deviation from which may indicate disease or a change in physiology. In particular, increased free water content in tissue, such as edema, will significantly prolong T1 relaxation times, whereas significant iron and fat content typically lower T1 relaxation times [20]. Myocardial T1 values may be measured using a number of T1 mapping sequences, including those based on inversion-recovery, saturation-recovery, or a hybrid approach [21–24]. Current evidence demonstrates that myocardial T1 values can be measured within a tight normal range, with clinically-relevant sensitivity to changes in a wide range of cardiac diseases [20].

How T1 mapping can be used for the detection of myocardial ischemia – basic principles

Native, or pre-contrast, T1 times reflect a composite signal from both the intracellular and extracellular space, the latter of which includes the interstitial and intravascular compartments. MBV, from the intravascular compartment, constitutes 10% of the total myocardial volume at rest [3], and contributes to the resting myocardial T1 through the partial volume of blood [25]. In normal myocardium supplied by normal, unobstructed coronary arteries, there is significant coronary vasodilatory reserve, which can be elicited with administration of adenosine vasodilator stress.

While coronary vasodilation is usually associated with increased coronary flow, the increase in vascular cross-sectional area also increases intramyocardial blood volume. Given that blood T1 is typically much longer than myocardial T1, this is expected to increase myocardial T1. Using conventional adenosine vasodilatory stress protocols, a 6% increase in myocardial T1 during vasodilator stress has been reported in normal volunteers both at 1.5 and 3T [17].

Stress and rest T1 mapping in patients with coronary artery disease

In patients with coronary artery disease (CAD), the resting T1 in areas of chronic myocardial infarction is typically significantly elevated compared to normal myocardium, and shows no change in T1 during vasodilatory stress [17] (Figure 1). Interestingly, ischemic myocardium subtended by significant coronary stenosis have compensatory downstream coronary vasodilation even at rest, and this is detectable as mildly elevated resting myocardial T1 values, but do not show further coronary vasodilatory response during stress, and, thus, no change in stress myocardial T1 [17]. Accordingly, adenosine stress and rest T1 mapping may be used to distinguish normal, infarcted and ischemic myocardium, without the need for gadolinium contrast agents, due to their distinctive rest and stress T1 profiles [17].

Stress and rest T1 mapping in patients without obstructive CAD

Adenosine stress and rest T1 mapping may also be used to assess coronary vasodilatory reserve in patients without obstructive CAD. It has been shown that in patients with severe aortic stenosis, but without significant CAD on angiography, increased coronary blood flow and

vasodilation is present at rest due to the increased demands of the pressure-overloaded and hypertrophied myocardium [26–28]. This expansion in the myocardial intravascular compartment is detectable using adenosine stress and rest T1 mapping, manifest as an elevated resting myocardial T1, but achieving the same maximal stress T1 response when compared to normal individuals [16]. Interestingly, this diminished stress T1 response normalizes 7 months after aortic valve replacement with relief of the pressure overload. This observation supports the notion that, in severe AS, increased resting myocardial T1 may predominantly reflect the changes in intravascular compartment, rather than solely from the presence of diffuse myocardial fibrosis in the interstitial compartment as previously believed. Stress and rest T1 mapping appear to hold promise for assessing coronary vascular function and vasodilatory reserve also in the absence of obstructive CAD.

Caveats and limitations

As for any novel MR technique, the biological mechanisms of native and stress T1 are not yet fully elucidated. Although the normal stress T1 response of 6% appears to be conserved across commonly applied field strengths within a single technique [17], this may not be directly applicable for other confounds or methods without further validation studies. The change in stress and rest T1 is relatively modest at 6% compared to the typical repeat variability of T1 measures of ~2%; much further work is required to make it into a clinically-robust diagnostic method. In view of the dynamic heart rate range encountered during physiologic and pharmacologic stress, it is recommended to use methods free of heart-rate dependency for stress T1 mapping. MOLLI techniques that exhibit heart-rate dependency appear to show lower stress T1 responses [18]. Saturation-based techniques [23] have little heart-rate dependency, and with ongoing improvements in SNR [29], maybe also find application in stress T1 mapping.

Future directions and implications

Adenosine stress and rest T1 mapping shows promise for the detection of ischemia, and the assessment of coronary reserve and, perhaps, the health of the micro-coronary circulation without the need for gadolinium contrast agents. Stress and rest T1 mapping is an area of active research, including validation against quantitative perfusion measures, invasive coronary measurements and diagnostic performance in a range of cardiac conditions. The effects of exercise, other pharmacological stress agents, as well as caffeine and other known modulators of vascular reactivity on T1 may be explored to determine clinical applicability. Over time, collective evidence will allow better understanding of the mechanisms for the observed changes for this emerging technique and its clinical utility.

T2 mapping

BOLD imaging and T2/T2* maps

T2 and T2* changes underlie the Blood Oxygenation Level Dependent (BOLD) contrast mechanism through a complex

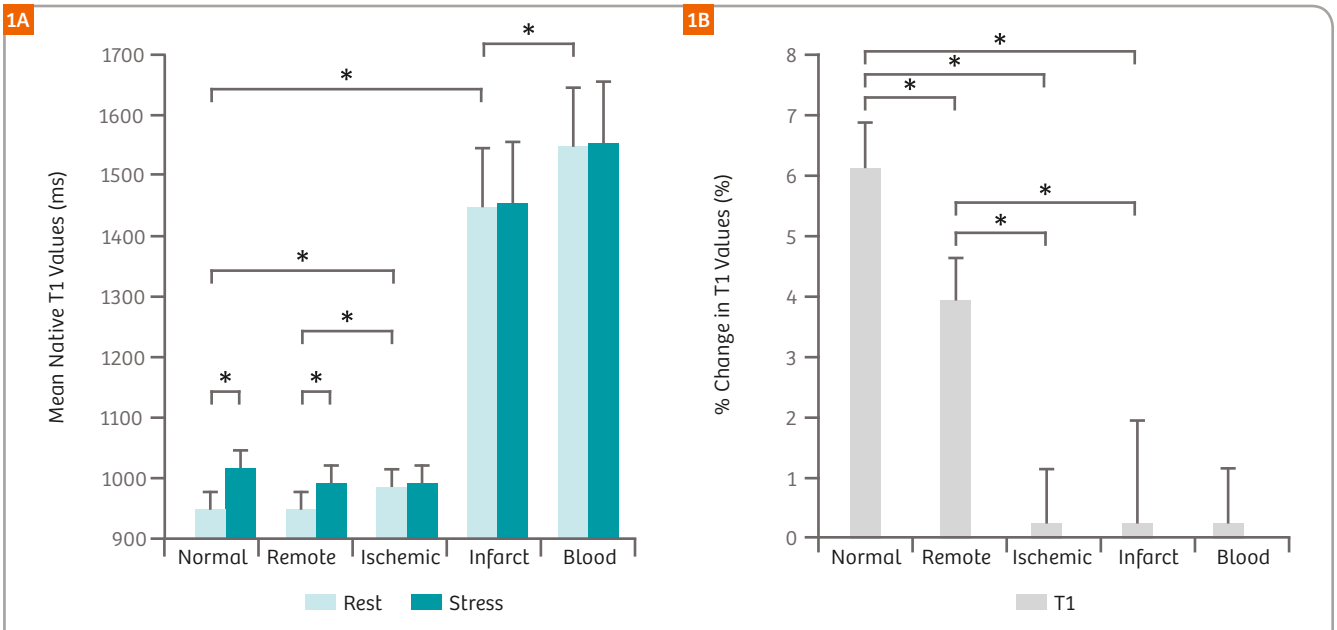

Figure 1: Myocardial T1 at rest and during adenosine stress at 1.5T. **(1A)** T1 values at rest in normal and remote tissue were similar and significantly lower than in ischemic regions. Infarct T1 was the highest of all myocardial tissue, but lower than the reference left ventricular blood pool of patients. During adenosine stress, normal and remote myocardial T1 increased significantly from baseline, while T1 in ischemic and infarcted regions remained relatively unchanged. **(1B)** Relative T1 reactivity (T1) in the patient's remote myocardium was significantly blunted compared to normal, and completely abolished in ischemic and infarcted regions. All data indicate mean ± 1 SD. *p < 0.05. *(Adapted from Liu A. et al. JACC: Cardiovascular Imaging 2016; 9 (1):27-36 originally published by Elsevier and shared under a Creative Commons license https://creativecommons.org/licenses/by/4.0/legalcode.)*

2

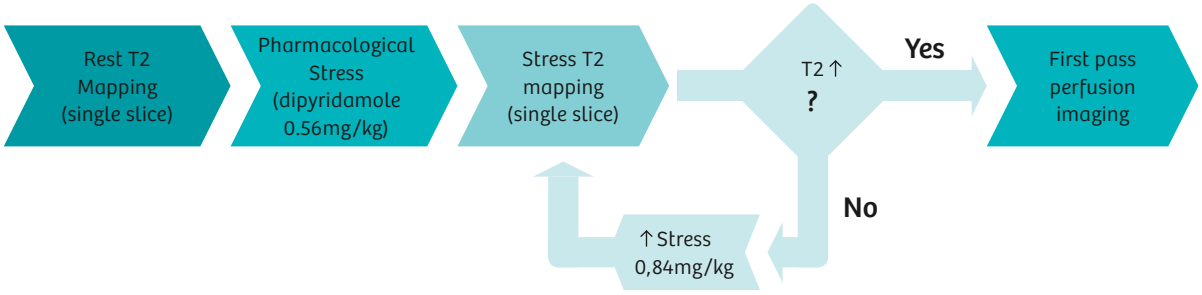

Figure 2: Stress-mapping protocol using T2 mapping to identify effective vasodilation and increase in T2 values in the myocardium. If T2 does not increase, this would prompt a review of the stress protocol, in this case with increment in the value of dipyridamole from the original 0.56 mg/kg to 0.84 mg/kg. Light blue color highlights the novel elements inserted into the standard stress imaging protocol.

relationship between tissue metabolic demands, oxygen delivery (MBF) and myocardial blood oxygen levels (MBV, mainly capillary and venous) [9, 13, 30]. Oxygenation-sensitive CMR has been used for many years to reflect changes in the intrinsic contrast properties of deoxygenated hemoglobin with most of the previous work using BOLD T2-weighted images or T2* imaging but not specific T2 parametric maps [31]. BOLD imaging relies on the fact that with vasodilation and maintenance of oxygen demand, there will be a decrease in the levels of de-oxygenated hemoglobin in the venous capillary bed resulting in an increase in T2 or T2* values. Considering a doubling of the MBV during vasodilation with a reduction of 40 to 70% of the OEF (the other components of the extravascular space being stable), the changes in T2/T2* will predominantly reflect the increase in intravascular signal, resulting in a reported global myocardial T2/T2* increase of 10–18% [9]. With ischemia, the effect is exactly the opposite, with an increase in de-oxygenated hemoglobin and a consequent decrease in T2/T2* values in that myocardial segment. These effects are highly dependent on the field strength, and at 3 Tesla the sensitivity to changes can triple [32].

Initial attempts at measuring changes in the content of de-oxygenated hemoglobin in the heart with T2 imaging used either T2-weighted turbo spin echo techniques or direct T2 measurements based on spin echo methods [33]. However, these techniques have been hampered by the long acquisition times, susceptibility artifacts and limitations such as residual blood signal, motion, heart rate dependency, irregular rhythms or surface coil positioning. To circumvent these problems, T2 maps based on T2-prepared steady-state free precession imaging were developed with further improvements in motion correction or free-breathing acquisitions [34–36]. These sequences provide practical T2 maps that can be acquired in a single breath hold or during free breathing, and provide accurate and reproducible T2 values of the myocardium [37]. Most of the clinical applications of these newer T2 mapping approaches have been directed to edema imaging, with BOLD T2 imaging having been performed using signal intensity evaluation but not direct T2 measurements [31]. While direct T2* mapping has been shown to differentiate vasodilatory states from rest, as well as ischemic from normal myocardial segments, despite the increased sensitivity at 3T, susceptibility artifacts have somewhat limited the use of T2* mapping for BOLD imaging [12].

Clinical applications

Clinical demonstrations of direct T2 maps for stress imaging have not yet been fully developed but initial work has validated their use with the purpose of measuring myocardial oxygenation [6]. Recently, a protocol was devised to use a commercially available T2 mapping sequence in a routine 3 Tesla CMR exam for ischemia evaluation [19]. Given the previous evidence of the sensitivity of T2 mapping to detect changes induced by vasodilation, we hypothesized that we could predict the effectiveness of vasodilatory stimulus using dipyridamole before the injection of contrast for first-pass perfusion. For comparison, we used the identification of splenic switch-off as a marker of the effectiveness of the pharmacological stimulus as published by Manisty *et al.* [38]. In short, visual assessment of spleen perfusion allowed the identification of patients who were understressed and did not demonstrate qualitative attenuation of signal during stress versus rest. While this allows for post-exam assessment of pharmacological inadequate stimulus, it only provides this information after contrast has been injected and the stress stimulus has already been terminated, not allowing any action for protocol optimization such as increasing the dose of adenosine or dipyridamole before first-pass perfusion [39]. The stress protocol used for this study is shown in Figure 2. Given the intrinsic lack of contrast needed to detect vasodilation changes with T2 mapping, any action needed to adjust stress induction could be taken before injection of contrast. The T2 map sequence used for the study is shown in Figure 3, and is used to acquire one short-axis slice with a single breath-hold using three T2-preparation times, non-rigid motion correction and generation of an immediate in-line pixel-wise T2 map based on automated curve fitting. This protocol was applied in fifty patients and we found that there was a significant inverse correlation between changes in myocardial T2 values and splenic signal intensity.

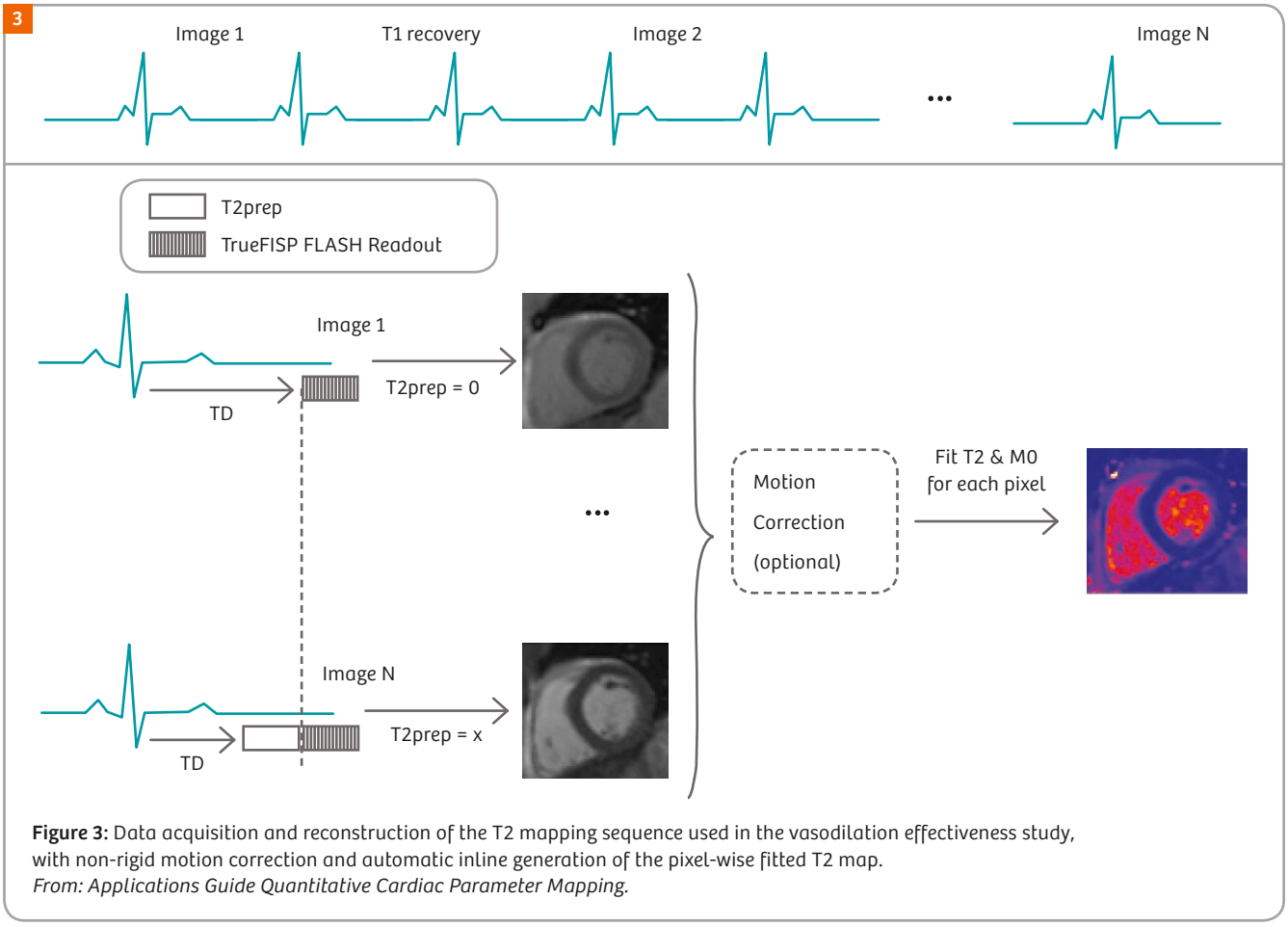

Figure 3: Data acquisition and reconstruction of the T2 mapping sequence used in the vasodilation effectiveness study, with non-rigid motion correction and automatic inline generation of the pixel-wise fitted T2 map.
From: Applications Guide Quantitative Cardiac Parameter Mapping.

A change of more than 2.5% or 1.0 ms in the resting T2 value after stress had a sensitivity of 81.4% and specificity of 100% to detect patients with visually positive spleen switch-off. An example of a patient with positive and negative effective vasodilation compared to the splenic switch-off sign is shown in Figure 4. The mean difference in T2 values before and after stress of + 10.6% found in our study is in line with previous papers that used T2* mapping and showed similar degrees of changes after vasodilatory stimulus [9, 11, 14, 15]. In comparison to changes seen in other non-ischemic myocardial segments using T2 signal intensity comparisons at 3 Tesla, the differences were similar to remote segments in CAD patients (9.95 ± 1.1%) but lower than in normal volunteers (17.0 ± 1.1%) possibly reflecting an already subclinical impaired vascular function in patients with risk factors versus normals [39].

Future studies

While this study did not include a specific evaluation of T2 map changes with stress in ischemic versus non-ischemic segments, we believe that future studies using stress T2 mapping could reproduce the positive findings described previously of a comparison of T2 signal intensity pre- and post-stress. Given the practical and rather simple application of stress-mapping in routine protocols, even with current single slice 2D acquisitions it would be feasible to acquire 3 short-axis slices and one long-axis slice of the left ventricle as is done in perfusion imaging during stress in a short period of time, even in addition to traditional first-pass contrast images. Improvements in 3D acquisitions [40, 41] could result in whole-heart T2 coverage with acceptable acquisition times and then allow for evaluation of all myocardial segments improving spatial coverage while keeping high-resolution images and minimizing heart rate dependency. Finally, while ischemia detection has always been associated with stress induction, it has been shown that BOLD imaging can differentiate myocardial ischemic segments versus normal segments even at rest using systolic and diastolic ratios determined by signal intensity values [42]. More recently, Arnold *et al.* also demonstrated that the use of signal intensity BOLD images could be used to discriminate myocardial segments perfused by anatomically significantly obstructed coronary arteries without the need for stress [43]. Neither study assessed absolute quantification of T2 or T2* values so it remains to be proven if direct parametric mapping can also be helpful in identifying ischemia even at rest.

Conclusions

The use of currently available parametric maps after vasodilatory stress allows for the potential detection of

4

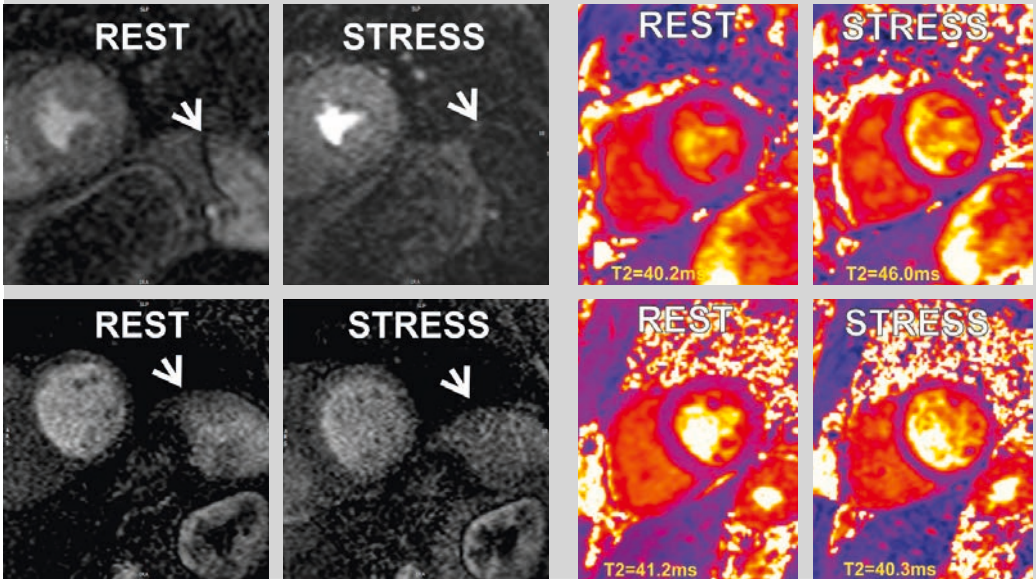

Figure 4:
In the top row, an example of a patient with positive spleen switch-off and an increase in post stress T2 from 40.2 ms at baseline to 46.0 ms after vasodilation (14.4% increase). In the bottom row, a patient with negative switch-off and no significant changes in septal T2 values from a baseline of 41.2 ms to 40.3 ms (-2.2%).

ischemic and infarcted myocardium segments, assessment of the effectiveness of the pharmacological stress induction and opens the possibility of studying different parameters of myocardial supply and demand with high accuracy. With the added advantage of not needing contrast agents, stress-mapping might also be useful for patients with impaired kidney function or who cannot receive these agents for other reasons. Given the previously demonstrated discrepancies between myocardial flow and true myocardial ischemia [8], stress imaging using parametric maps may also offer a new tool on the CMR armamentarium, complementary to current sequences with addition of new physiological information.

References

1 Salerno M, Kramer CM. Advances in parametric mapping with CMR imaging. JACC Cardiovasc Imaging. 2013;6:806-22.
2 Schelbert EB, Messroghli DR. State of the Art: Clinical Applications of Cardiac T1 Mapping. Radiology. 2016;278:658-76.
3 Judd RM, Levy BI. Effects of barium-induced cardiac contraction on large- and small-vessel intramyocardial blood volume. Circ Res. 1991;68:217-25.
4 Crystal GJ, Downey HF, Bashour FA. Small vessel and total coronary blood volume during intracoronary adenosine. Am J Physiol. 1981;241:H194-201.
5 McCommis KS, Zhang H, Goldstein TA, Misselwitz B, Abendschein DR, Gropler RJ, Zheng J. Myocardial blood volume is associated with myocardial oxygen consumption: an experimental study with cardiac magnetic resonance in a canine model. JACC Cardiovasc Imaging. 2009;2:1313-20.
6 McCommis KS, O'Connor R, Lesniak D, Lyons M, Woodard PK, Gropler RJ, Zheng J. Quantification of global myocardial oxygenation in humans: initial experience. J Cardiovasc Magn Reson. 2010;12:34.
7 Zheng J, Wang J, Rowold FE, Gropler RJ, Woodard PK. Relationship of apparent myocardial T2 and oxygenation: towards quantification of myocardial oxygen extraction fraction. J Magn Reson Imaging. 2004;20:233-41.
8 Karamitsos TD, Leccisotti L, Arnold JR, Recio-Mayoral A, Bhamra-Ariza P, Howells RK, Searle N, Robson MD, Rimoldi OE, Camici PG, Neubauer S, Selvanayagam JB. Relationship between regional myocardial oxygenation and perfusion in patients with coronary artery disease: insights from cardiovascular magnetic resonance and positron emission tomography. Circ Cardiovasc Imaging. 2010;3:32-40.
9 Foltz WD, Huang H, Fort S, Wright GA. Vasodilator response assessment in porcine myocardium with magnetic resonance relaxometry. Circulation. 2002;106:2714-9.
10 Zhang H, Gropler RJ, Li D, Zheng J. Assessment of myocardial oxygen extraction fraction and perfusion reserve with BOLD imaging in a canine model with coronary artery stenosis. J Magn Reson Imaging. 2007;26:72-9.
11 Beache GM, Herzka DA, Boxerman JL, Post WS, Gupta SN, Faranesh AZ, Solaiyappan M, Bottomley PA, Weiss JL, Shapiro EP, Hill MN. Attenuated myocardial vasodilator response in patients with hypertensive hypertrophy revealed by oxygenation-dependent magnetic resonance imaging. Circulation. 2001;104:1214-7.
12 Manka R, Paetsch I, Schnackenburg B, Gebker R, Fleck E, Jahnke C. BOLD cardiovascular magnetic resonance at 3.0 tesla in myocardial ischemia. J Cardiovasc Magn Reson. 2010;12:54.
13 Vohringer M, Flewitt JA, Green JD, Dharmakumar R, Wang J, Jr., Tyberg JV, Friedrich MG. Oxygenation-sensitive CMR for assessing vasodilator-induced changes of myocardial oxygenation. J Cardiovasc Magn Reson. 2010;12:20.
14 Wacker CM, Bock M, Hartlep AW, Beck G, van Kaick G, Ertl G, Bauer WR, Schad LR. Changes in myocardial oxygenation and perfusion under pharmacological stress with dipyridamole: assessment using T*2 and T1 measurements. Magn Reson Med. 1999;41:686-95.
15 Wacker CM, Hartlep AW, Pfleger S, Schad LR, Ertl G, Bauer WR. Susceptibility-sensitive magnetic resonance imaging detects human myocardium supplied by a stenotic coronary artery without a contrast agent. J Am Coll Cardiol. 2003;41:834-40.
16 Mahmod M, Piechnik SK, Levelt E, Ferreira VM, Francis JM, Lewis A, Pal N, Dass S, Ashrafian H, Neubauer S, Karamitsos TD. Adenosine stress native T1 mapping in severe aortic stenosis: evidence for a role of the intravascular compartment on myocardial T1 values. J Cardiovasc Magn Reson. 2014;16:92.

17 Liu A, Wijesurendra RS, Francis JM, Robson MD, Neubauer S, Piechnik SK, Ferreira VM. Adenosine Stress and Rest T1 Mapping Can Differentiate Between Ischemic, Infarcted, Remote, and Normal Myocardium Without the Need for Gadolinium Contrast Agents. JACC Cardiovasc Imaging. 2016;9:27-36.
18 Kuijpers D, Prakken NH, Vliegenthart R, van Dijkman PR, van der Harst P, Oudkerk M. Caffeine intake inverts the effect of adenosine on myocardial perfusion during stress as measured by T1 mapping. Int J Cardiovasc Imaging. 2016;32:1545-53.
19 Fernandes JL, Fioravante LA, Mazo PE, Greiser A, Strecker R. Use of T2 Maps for Rapid Prediction of Stress Effectiveness before the injection of contrast in myocardial perfusion studies at 3.0T. J Cardiovasc Magn Reson. 2016;18(Suppl1):Q53.
20 Ferreira VM, Piechnik SK, Robson MD, Neubauer S, Karamitsos TD. Myocardial Tissue Characterization by Magnetic Resonance Imaging: Novel Applications of T1 and T2 Mapping. J Thorac Imaging. 2014;29:147-54.
21 Messroghli DR, Greiser A, Frohlich M, Dietz R, Schulz-Menger J. Optimization and validation of a fully-integrated pulse sequence for modified look-locker inversion-recovery (MOLLI) T1 mapping of the heart. J Magn Reson Imaging. 2007;26:1081-1086.
22 Piechnik SK, Ferreira VM, Dall'Armellina E, Cochlin LE, Greiser A, Neubauer S, Robson MD. Shortened Modified Look-Locker Inversion recovery (ShMOLLI) for clinical myocardial T1-mapping at 1.5 and 3 T within a 9 heartbeat breathhold. J Cardiovasc Magn Reson. 2010;12:69.
23 Chow K, Flewitt JA, Green JD, Pagano JJ, Friedrich MG, Thompson RB. Saturation recovery single-shot acquisition (SASHA) for myocardial T1 mapping. Magn Reson Med. 2013:n/a-n/a.
24 Roujol S, Weingärtner S, Foppa M, Chow K, Kawaji K, Ngo LH, Kellman P, Manning WJ, Thompson RB, Nezafat R. Accuracy, Precision, and Reproducibility of Four T1 Mapping Sequences: A Head-to-Head Comparison of MOLLI, ShMOLLI, SASHA, and SAPPHIRE. Radiology. 2014;272:683-689.
25 Piechnik SK, Ferreira VM, Lewandowski AJ, Ntusi NAB, Banerjee R, Holloway C, Hofman MBM, Sado DM, Maestrini V, White SK, Lazdam M, Karamitsos T, Moon JC, Neubauer S, Leeson P, Robson MD. Normal variation of magnetic resonance T1 relaxation times in the human population at 1.5 T using ShMOLLI. J Cardiovasc Magn Reson. 2013;15.
26 Rajappan K, Rimoldi OE, Dutka DP, Ariff B, Pennell DJ, Sheridan DJ, Camici PG. Mechanisms of coronary microcirculatory dysfunction in patients with aortic stenosis and angiographically normal coronary arteries. Circulation. 2002;105:470-6.
27 Marcus ML, Doty DB, Hiratzka LF, Wright CB, Eastham CL. Decreased coronary reserve: a mechanism for angina pectoris in patients with aortic stenosis and normal coronary arteries. N Engl J Med. 1982;307:1362-6.
28 Marcus ML, Koyanagi S, Harrison DG, Doty DB, Hiratzka LF, Eastham CL. Abnormalities in the coronary circulation that occur as a consequence of cardiac hypertrophy. Am J Med. 1983;75:62-6.
29 Chow K, Spottiswoode BS, Pagano JJ, Thompson RB. Improved precision in SASHA T(1)mapping with a variable flip angle readout. J Cardiovasc Magn Reson. 2014;16:M9-M9.
30 Li D, Dhawale P, Rubin PJ, Haacke EM, Gropler RJ. Myocardial signal response to dipyridamole and dobutamine: demonstration of the BOLD effect using a double-echo gradient-echo sequence. Magn Reson Med. 1996;36:16-20.
31 Friedrich MG, Karamitsos TD. Oxygenation-sensitive cardiovascular magnetic resonance. J Cardiovasc Magn Reson. 2013;15:43.
32 Dharmakumar R, Arumana JM, Tang R, Harris K, Zhang Z, Li D. Assessment of regional myocardial oxygenation changes in the presence of coronary artery stenosis with balanced SSFP imaging at 3.0 T: theory and experimental evaluation in canines. J Magn Reson Imaging. 2008;27:1037-45.
33 Abdel-Aty H, Simonetti O, Friedrich MG. T2-weighted cardiovascular magnetic resonance imaging. J Magn Reson Imaging. 2007;26:452-9.
34 Huang TY, Liu YJ, Stemmer A, Poncelet BP. T2 measurement of the human myocardium using a T2-prepared transient-state TrueFISP sequence. Magn Reson Med. 2007;57:960-6.
35 Giri S, Chung YC, Merchant A, Mihai G, Rajagopalan S, Raman SV, Simonetti OP. T2 quantification for improved detection of myocardial edema. J Cardiovasc Magn Reson. 2009;11:56.
36 Kellman P, Aletras AH, Mancini C, McVeigh ER, Arai AE. T2-prepared SSFP improves diagnostic confidence in edema imaging in acute myocardial infarction compared to turbo spin echo. Magn Reson Med. 2007;57:891-7.
37 Wassmuth R, Prothmann M, Utz W, Dieringer M, von Knobelsdorff-Brenkenhoff F, Greiser A, Schulz-Menger J. Variability and homogeneity of cardiovascular magnetic resonance myocardial T2-mapping in volunteers compared to patients with edema. J Cardiovasc Magn Reson. 2013;15:27.
38 Manisty C, Ripley DP, Herrey AS, Captur G, Wong TC, Petersen SE, Plein S, Peebles C, Schelbert EB, Greenwood JP, Moon JC. Splenic Switch-off: A Tool to Assess Stress Adequacy in Adenosine Perfusion Cardiac MR Imaging. Radiology. 2015;276:732-40.
39 Karamitsos TD, Ntusi NA, Francis JM, Holloway CJ, Myerson SG, Neubauer S. Feasibility and safety of high-dose adenosine perfusion cardiovascular magnetic resonance. J Cardiovasc Magn Reson. 2010;12:66.
40 van Heeswijk RB, Piccini D, Feliciano H, Hullin R, Schwitter J, Stuber M. Self-navigated isotropic three-dimensional cardiac T2 mapping. Magn Reson Med. 2015;73:1549-54.
41 Yang HJ, Sharif B, Pang J, Kali A, Bi X, Cokic I, Li D, Dharmakumar R. Free-breathing, motion-corrected, highly efficient whole heart T2 mapping at 3T with hybrid radial-cartesian trajectory. Magn Reson Med. 2016;75:126-36.
42 Tsaftaris SA, Zhou X, Tang R, Li D, Dharmakumar R. Detecting myocardial ischemia at rest with cardiac phase-resolved blood oxygen level-dependent cardiovascular magnetic resonance. Circ Cardiovasc Imaging. 2013;6:311-9.
43 Arnold JR, Jerosch-Herold M, Karamitsos TD, Francis JM, Bhamra-Ariza P, Sarwar R, Choudhury R, Selvanayagam JB, Neubauer S. Detection of Coronary Stenosis at Rest Using BOLD-CMR. JACC Cardiovasc Imaging. 2016.

Contact

Juliano L. Fernandes, M.D., Ph.D., MBA

Radiologia Clinica de Campinas

Av Jose de Souza Campos 840
Campinas – SP – Brazil – 13092-123
jlaraf@terra.com.br

Juliano L. Fernandes

Vanessa M. Ferreira

Stefan K. Piechnik

Combined ^{18}F-FDG PET/MR for Enhanced Imaging of Active Cardiac Sarcoidosis

Nicolas A. Karakatsanis, Ph.D., MEng; Marc R. Dweck, M.D., Ph.D.; Ronan Abgral, M.D., Ph.D.; Maria Giovanna Trivieri, M.D., Ph.D.; Philip M. Robson, Ph.D.; Jason C. Kovacic, M.D., Ph.D.; Zahi A. Fayad, Ph.D.

Translational and Molecular Imaging Institute, Icahn School of Medicine at Mount Sinai, New York, NY, USA

Introduction

Sarcoidosis is a multisystem disease characterized by granuloma formation, inflammation and fibrosis most commonly affecting the lungs and mediastinal lymph nodes [1]. Cardiac involvement is under-diagnosed but is the leading cause of death amongst patients with sarcoidosis [2–6]. Early intervention with steroids appears to improve prognosis [7], making the accurate and early diagnosis of subclinical but active cardiac sarcoidosis an important clinical goal. Unfortunately establishing this important diagnosis remains a major clinical challenge [8, 9].

Cardiac magnetic resonance (MR) imaging with late gadolinium enhancement (LGE) has recently been introduced for visualizing the pattern of myocardial injury due to cardiac sarcoidosis [10, 11]. However, LGE cannot differentiate between active disease and old chronic scarring, thus limiting the specificity of CMR-based active sarcoidosis assessments. On the other hand, positron emission tomography (PET) imaging with ^{18}F-Fludeoxyglucose (^{18}F-FDG)[1], has recently been used to identify regions of increased myocardial inflammation in patients with active cardiac sarcoidosis [12–14]. However, glucose is the predominant source of energy consumed by the myocardium, and high non-specific physiological uptake of ^{18}F-FDG can often lead to false positive identification of active myocardial disease. Although dietary restrictions in the 12 hours prior to PET imaging may switch the heart from glucose to free-fatty acid metabolism and effectively suppress physiological ^{18}F-FDG uptake in the myocardium, this strategy is not always successful [14–16].

Recently, hybrid PET/MR systems have become clinically available [17–19]. The simultaneous hybrid PET/MR Biograph mMR system (Siemens Healthcare, Erlangen, Germany) combines a sensitive PET scanner with a 3T MR system to enable spatial co-registration of complementary imaging data from the two modalities [20]. Simultaneous acquisition of PET and MR data allows disease activity measured by PET to be precisely overlaid on the pattern of injury in the myocardium determined by MR from a single scan session [21]. Moreover, by replacing CT with MR, PET/MR is associated with a lower radiation dose, which is important, especially in chronic conditions such as cardiac sarcoidosis, where follow-up would be desirable [17].

Recent studies in our institution have investigated the use of MR/PET for evaluating cardiac disease [21, 22] including cardiac sarcoidosis by assessing the overlap between ^{18}F-FDG PET activity and the pattern of myocardial injury on LGE MR. We have investigated the potential of combined PET/MR to differentiate between active and inactive cardiac sarcoid as well as identifying false-positive PET indications, due to inadequate physiological ^{18}F-FDG myocardial uptake suppression [22, 23].

[1] The full prescribing information for the Fludeoxyglucose F18 injection can be found at page 37.

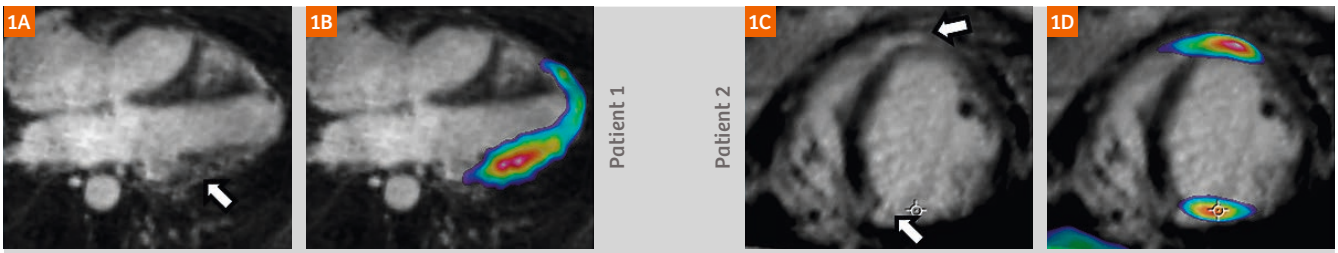

Figure 1: From left to right: **(1A, C)** LGE MR images showed elevated LGE signal at the lateral and anteroseptal wall for patient 1 (62-year-old male) and patient 2 (63-year-old female) respectively. **(1B, D)** Matched ^{18}F-FDG PET fused with previous LGE MR images showed high ^{18}F-FDG uptake overlapping with the LGE pattern of injury.

Optimized PET/MR imaging protocol for cardiac sarcoidosis assessment

In this article, we present four clinical exams where initial diagnosis for active cardiac sarcoidosis was unclear when either LGE MR or ^{18}F-FDG PET exams were evaluated independently [22, 23]. All participating subjects had a previous history of proven extra-cardiac sarcoidosis and/or clinical symptoms to suggest cardiac sarcoid involvement. Patients gave written informed consent and were screened for contra-indications before undergoing PET/MR imaging.

Dynamic PET data were acquired across a single bed position centered over the heart in list mode for a period of 90 min beginning 10 min after 5 MBq/kg ^{18}F-FDG injection. The collected PET data were then histogrammed into a single scan time window corresponding to a delayed 40–100 min post-injection period. Subsequently the PET data were reconstructed with an iterative ordinary Poisson Ordered Subset Expectation Maximization (OP-OSEM) algorithm using 3 iterations, 21 subsets and a resolution modeling method optimized for the Biograph mMR system. An MR-based attenuation correction method was employed for the PET data based on 4-tissue class segmentation of a standard breath-hold 3D Dixon VIBE MR sequence. Attenuation from the body transmit coil and spine array, but not from the flexible chest array, were included in the attenuation map.

Cardiac MRI, performed simultaneously with the dynamic PET acquisition, included

i) TrueFISP cine images, acquired in the long-axis (2-chamber, 4-chamber) of the left ventricle, followed by

ii) a complete short-axis stack for assessment of cardiac volume and function, and

iii) inversion recovery-prepared spoiled gradient echo late gadolinium enhanced imaging, 10–15 minutes post injection of 0.2 mmol/kg Multi Hance (Bracco imaging, Milan, Italy) in short- and long-axis views [24]. Inversion times were optimized to null normal myocardium with images repeated in two separate phase-encoding directions to exclude artifact.

Enhancing cardiac sarcoid diagnosis with simultaneous PET/MR imaging

In patients 1 and 2, elevated ^{18}F-FDG uptake (at later times >60 min post tracer injection) co-localized with the pattern of late gadolinium enhancement observed on MRI (Fig. 1). The coincidental observation of both increased ^{18}F-FDG-PET activity and evidence of myocardial injury on late gadolinium enhancement strongly suggests the presence of active cardiac sarcoidosis. Target-to-background (TBR) values were calculated as mean standard uptake values (SUV) in regions-of-interest (ROI) drawn over the area of myocardial injury divided by the mean blood pool SUV value in the left ventricular cavity. Mean ^{18}F-FDG TBR in areas of myocardial injury were 2.2 (patient 1) and 2.0 (patient 2).

Conversely, overlap of PET and LGE was not observed in patients 3 and 4 (Fig. 2). In patient 3 transmural scarring in a coronary distribution affecting the anteroseptum was observed on LGE MR but with no evidence of increased ^{18}F-FDG PET uptake in this region. This finding was felt to be consistent with a chronic and silent myocardial infarction. By contrast, patient 4 demonstrated avid and diffuse ^{18}F-FDG uptake throughout the entire left ventricular myocardium in the absence of any evidence of myocardial injury on LGE MR. Given that cardiac sarcoidosis is a focal disease process this was felt likely to represent failed suppression of the physiological ^{18}F-FDG uptake [25]. This hypothesis was supported by the very high TBR values (6.3 60–90 min post injection) in this patient compared to subjects 1 and 2. However, more evidence is needed to be able to differentiate the true- from the false-positive cardiac sarcoid ^{18}F-FDG assessments in the absence of positive LGE MR signal.

Future prospects for cardiac PET/MR imaging

This preliminary study has demonstrated the clinical potential of simultaneous PET/MR imaging in the evaluation of active cardiac sarcoidosis. PET and MR images can be accurately aligned allowing a diagnosis of active cardiac sarcoidosis to be made with confidence when increased

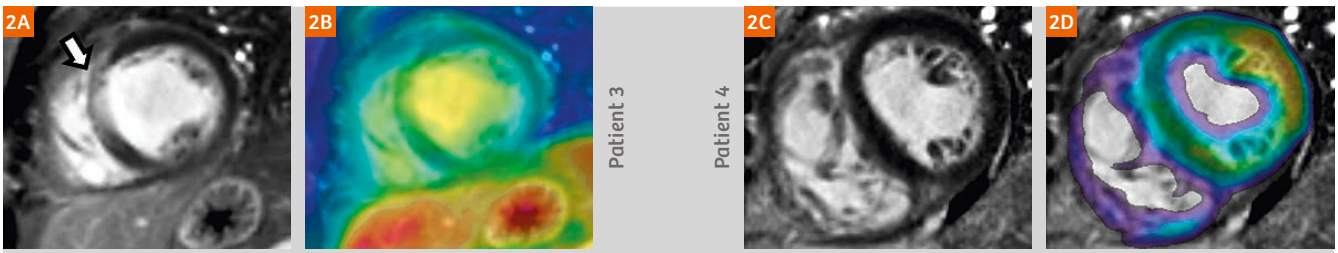

Figure 2: (2A, B) Patient 3 (50-year-old female), short-axis LGE MR showed transmural LGE on the anteroseptum, while fused PET/MR images demonstrated absence of high ^{18}F-FDG uptake on the same region. **(2C, D)** Patient 4 (42-year-old male) LGE MR showed absence of LGE on the myocardial wall. Fused PET/MR images indicated diffused intense ^{18}F-FDG uptake.

^{18}F-FDG uptake co-localizes with the pattern of injury on late gadolinium enhancement MRI. Moreover this approach can help differentiate this pattern from non-active cardiac sarcoid LGE signal or false positive ^{18}F-FDG uptake due to failed myocardial suppression.

References

1 Baughman, R.P., Teirstein, A.S., Judson, M.A., Rossman, M.D., Yeager Jr, H., Bresnitz, E.A., De Palo, L, Hunninghake, G., Iannuzzi, M.C., Johns, C.J. and McLennan, G. 2001. Clinical characteristics of patients in a case control study of sarcoidosis. Am J Resp Crit Care Med, 164(10), pp.1885-1889.

2 Kim, J.S., Judson, M.A., Donnino, R., Gold, M., Cooper, L.T., Prystowsky, E.N. and Prystowsky, S., 2009. Cardiac sarcoidosis. Am Heart J, 157(1), pp.9-21.

3 Iannuzzi, M.C. and Fontana, J.R., 2011. Sarcoidosis: clinical presentation, immunopathogenesis, and therapeutics. Jama, 305(4), pp.391-399.

4 Silverman, K.J., Hutchins, G.M. and Bulkley, B.H., 1978. Cardiac sarcoid: a clinicopathologic study of 84 unselected patients with systemic sarcoidosis.Circulation, 58(6), pp.1204-1211.

5 Hunninghake, G.W., Costabel, U., Ando, M., Baughman, R., Cordier, J.F., Du Bois, R., Eklund, A., Kitaichi, M., Lynch, J., Rizzato, G. and Rose, C., 1999. ATS/ERS/WASOG statement on sarcoidosis. J WASOG/World Assoc Sarc Other Granul Disord, 16(2), p.149.

6 Morgenthau, A.S. and Iannuzzi, M.C., 2011. Recent advances in sarcoidosis. CHEST, 139(1), pp.174-182.

7 Uemura, A., Morimoto, S.I., Hiramitsu, S., Kato, Y., Ito, T. and Hishida, H., 1999. Histologic diagnostic rate of cardiac sarcoidosis: evaluation of endomyocardial biopsies. Am Heart J, 138(2), pp.299-302.

8 Frank, H. and Globits, S., 1999. Magnetic resonance imaging evaluation of myocardial and pericardial disease. J Mag Res Imag, 10(5), pp.617-626.

9 Yamagishi, H., Shirai, N., Takagi, M., Yoshiyama, M., Akioka, K., Takeuchi, K. and Yoshikawa, J., 2003. Identification of cardiac sarcoidosis with 13N-NH3/18F-FDG PET. J Nucl Med, 44(7), pp.1030-1036.

10 Patel, M.R., Cawley, P.J., Heitner, J.F., Klem, I., Parker, M.A., Jaroudi, W.A., Meine, T.J., White, J.B., Elliott, M.D., Kim, H.W. and Judd, R.M., 2009. Detection of myocardial damage in patients with sarcoidosis.Circulation, 120(20), pp.1969-1977.

11 Tadamura, E., Yamamuro, M., Kubo, S., Kanao, S., Saga, T., Harada, M., Ohba, M., Hosokawa, R., Kimura, T., Kita, T. and Togashi, K., 2005. Effectiveness of delayed enhanced MRI for identification of cardiac sarcoidosis: comparison with radionuclide imaging. Am J Roentgen, 185(1), pp.110-115.

12 Youssef, G., Leung, E., Mylonas, I., Nery, P., Williams, K., Wisenberg, G., Gulenchyn, K.Y., DaSilva, J., Birnie, D., Wells, G.A. and Beanlands, R.S., 2012. The use of 18F-FDG PET in the diagnosis of cardiac sarcoidosis: a systematic review and metaanalysis including the Ontario experience.J Nucl Med, 53(2), pp.241-248.

13 Soussan, M., Augier, A., Brillet, P.Y., Weinmann, P. and Valeyre, D., 2014. Functional imaging in extrapulmonary sarcoidosis: FDG-PET/CT and MR features. Clin Nucl Med, 39(2), pp.e146-e159.

14 Manabe, O., Yoshinaga, K., Ohira, H. and Oyama-Manabe, N., 2016. Usefulness of 18F-FDG PET in Diagnosing Cardiac Sarcoidosis. InPerspectives on Nuclear Medicine for Molecular Diagnosis and Integrated Therapy (pp. 209-216). Springer Japan.

15 Tang, R., Wang, J.T.Y., Wang, L., Le, K., Huang, Y., Hickey, A.J. and Emmett, L., 2016. Impact of patient preparation on the diagnostic performance of 18F-FDG PET in cardiac sarcoidosis: A systematic review and meta-analysis. Clin Nucl Med, 41(7), pp.e327-e339.

16 Hulten, E., Aslam, S., Osborne, M., Abbasi, S., Bittencourt, M.S. and Blankstein, R., 2016. Cardiac sarcoidosis—state of the art review. Cardiov Diagn Therapy, 6(1), p.50.

17 Pichler, B.J., Kolb, A., Nägele, T. and Schlemmer, H.P., 2010. PET/MRI: paving the way for the next generation of clinical multimodality imaging applications. J Nucl Med, 51(3), pp.333-336

18 Ratib, O. and Nkoulou, R., 2014. Potential applications of PET/MR imaging in cardiology. J Nucl Med, 55(Supplement 2), pp.40S-46S.

19 Ohira, H., Birnie, D.H., Pena, E., Bernick, J., Mc Ardle, B., Leung, E., Wells, G.A., Yoshinaga, K., Tsujino, I., Sato, T. and Manabe, O., 2016. Comparison of 18F-fluorodeoxyglucose positron emission tomography (FDG PET) and cardiac magnetic resonance (CMR) in corticosteroid-naive patients with conduction system disease due to cardiac sarcoidosis. Eur J Nucl Med Mol Imag, 43(2), pp.259-269

20 Delso, G., Fürst, S., Jakoby, B., Ladebeck, R., Ganter, C., Nekolla, S.G., Schwaiger, M. and Ziegler, S.I., 2011. Performance measurements of the Siemens mMR integrated whole-body PET/MR scanner. J Nucl Med, 52(12), pp.1914-1922

21 Schneider, S., Batrice, A., Rischpler, C., Eiber, M., Ibrahim, T. and Nekolla, S.G., 2014. Utility of multimodal cardiac imaging with PET/MRI in cardiac sarcoidosis: implications for diagnosis, monitoring and treatment. Eur Heart J, 35(5), pp.312-312.

22 Abgral, R., Dweck, M.R., Robson, P.M., Trivieri, M.G., Karakatsanis, N.A., Sanz, J., Contreras, J., Fuster, V., Padilla, M., Kovacic, J.C. and Fayad, Z.A., 2016. Usefulness of combined FDG-PET/MR to diagnose active cardiac sarcoidosis. J Nucl Med, 57(suppl 2), pp.1668-1668.

23 Abgral, R., Dweck, M.R., Robson, P.M., Trivieri, M.G., Karakatsanis, N.A., Mani, V., Padilla, M., Miller, M., Lala, A., .Sanz, J., Narula, J., Fuster, V., Contreras, J., Kovacic, J.C. and Fayad, Z.A., 2016. Clinical Utility of Combined FDG-PET/MR to Assess Myocardial Disease J Am Coll Cardiol Img (in press) doi: 10.1016/j.jcmg.2016.02.029

24 Kellman, P. and Arai, A.E., 2012. Cardiac imaging techniques for physicians: late enhancement. J Mag Res Imag, 36(3), pp.529-542

25 Williams, G. and Kolodny, G.M., 2008. Suppression of myocardial 18F-FDG uptake by preparing patients with a high-fat, low-carbohydrate diet. Am J Roentg, 190(2), pp.W151-W156

Contact

Zahi A. Fayad, Ph.D, FAHA, FACC, FISMRM

Icahn School of Medicine at Mount Sinai

Mount Sinai Endowed Chair in Medical Imaging and Bioengineering

Professor of Radiology and Medicine (Cardiology)

Director, Translational and Molecular Imaging Institute

Director, Cardiovascular Imaging Research

Vice-Chair for Research, Department of Radiology

One Gustave L. Levy Place
Box 1234
New York, NY 10029-6574
USA
Phone: +1 212 824 8452
Fax: +1 240 368 8096
zahi.fayad@mssm.edu

HIGHLIGHTS OF PRESCRIBING INFORMATION

These highlights do not include all the information needed to use Fludeoxyglucose F 18 Injection safely and effectively. See full prescribing information for Fludeoxyglucose F 18 Injection. Fludeoxyglucose F 18 Injection, USP For intravenous use Initial U.S. Approval: 2005

RECENT MAJOR CHANGES

Warnings and Precautions (5.1, 5.2)	7/2010
Adverse Reactions (6)	7/2010

INDICATIONS AND USAGE

Fludeoxyglucose F18 Injection is indicated for positron emission tomography (PET) imaging in the following settings:

- Oncology: For assessment of abnormal glucose metabolism to assist in the evaluation of malignancy in patients with known or suspected abnormalities found by other testing modalities, or in patients with an existing diagnosis of cancer.
- Cardiology: For the identification of left ventricular myocardium with residual glucose metabolism and reversible loss of systolic function in patients with coronary artery disease and left ventricular dysfunction, when used together with myocardial perfusion imaging.
- Neurology: For the identification of regions of abnormal glucose metabolism associated with foci of epileptic seizures (1).

DOSAGE AND ADMINISTRATION

Fludeoxyglucose F 18 Injection emits radiation. Use procedures to minimize radiation exposure. Screen for blood glucose abnormalities.

- In the oncology and neurology settings, instruct patients to fast for 4 to 6 hours prior to the drug's injection. Consider medical therapy and laboratory testing to assure at least two days of normoglycemia prior to the drug's administration (5.2).
- In the cardiology setting, administration of glucose-containing food or liquids (e.g., 50 to 75 grams) prior to the drug's injection facilitates localization of cardiac ischemia (2.3).

Aseptically withdraw Fludeoxyglucose F 18 Injection from its container and administer by intravenous injection (2).

The recommended dose:

- for adults is 5 to 10 mCi (185 to 370 MBq), in all indicated clinical settings (2.1).
- for pediatric patients is 2.6 mCi in the neurology setting (2.2).

Initiate imaging within 40 minutes following drug injection; acquire static emission images 30 to 100 minutes from time of injection (2).

DOSAGE FORMS AND STRENGTHS

Multi-dose 30mL and 50mL glass vial containing 0.74 to 7.40 GBq/mL (20 to 200 mCi/mL) Fludeoxyglucose F 18 Injection and 4.5mg of sodium chloride with 0.1 to 0.5% w/w ethanol as a stabilizer (approximately 15 to 50 mL volume) for intravenous administration (3).

CONTRAINDICATIONS

None

WARNINGS AND PRECAUTIONS

- Radiation risks: use smallest dose necessary for imaging (5.1).
- Blood glucose adnormalities: may cause suboptimal imaging (5.2).

ADVERSE REACTIONS

Hypersensitivity reactions have occurred; have emergency resuscitation equipment and personnel immediately available (6).

To report SUSPECTED ADVERSE REACTIONS, contact PETNET Solutions, Inc. at 877-473-8638 or FDA at 1-800-FDA-1088 or www.fda.gov/medwatch.

USE IN SPECIFIC POPULATIONS

Pregnancy Category C: No human or animal data. Consider alternative diagnostics; use only if clearly needed (8.1).

- Nursing mothers: Use alternatives to breast feeding (e.g., stored breast milk or infant formula) for at least 10 half-lives of radioactive decay, if Fludeoxyglucose F 18 Injection is administered to a woman who is breast-feeding (8.3).
- Pediatric Use: Safety and effectiveness in pediatric patients have not been established in the oncology and cardiology settings (8.4).

See 17 for PATIENT COUNSELING INFORMATION

Revised: 1/2011

FULL PRESCRIBING INFORMATION: CONTENTS*

* Sections or subsections omitted from the full prescribing information are not listed.

FULL PRESCRIBING INFORMATION

1 INDICATIONS AND USAGE

Fludeoxyglucose F 18 Injection is indicated for positron emission tomography (PET) imaging in the following settings:

1.1 Oncology

For assessment of abnormal glucose metabolism to assist in the evaluation of malignancy in patients with known or suspected abnormalities found by other testing modalities, or in patients with an existing diagnosis of cancer.

1.2 Cardiology

For the identification of left ventricular myocardium with residual glucose metabolism and reversible loss of systolic function in patients with coronary artery disease and left ventricular dysfunction, when used together with myocardial perfusion imaging.

1.3 Neurology

For the identification of regions of abnormal glucose metabolism associated with foci of epileptic seizures.

2 DOSAGE AND ADMINISTRATION

Fludeoxyglucose F 18 Injection emits radiation. Use procedures to minimize radiation exposure. Calculate the final dose from the end of synthesis (EOS) time using proper radioactive decay factors. Assay the final dose in a properly calibrated dose calibrator before administration to the patient [see Description (11.2)].

2.1 Recommended Dose for Adults

Within the oncology, cardiology and neurology settings, the recommended dose for adults is 5 to 10 mCi (185 to 370 MBq) as an intravenous injection.

2.2 Recommended Dose for Pediatric Patients

Within the neurology setting, the recommended dose for pediatric patients is 2.6 mCi, as an intravenous injection. The optimal dose adjustment on the basis of body size or weight has not been determined [see Use in Special Populations (8.4)].

2.3 Patient Preparation

- To minimize the radiation absorbed dose to the bladder, encourage adequate hydration. Encourage the patient to drink water or other fluids (as tolerated) in the 4 hours before their PET study.
- Encourage the patient to void as soon as the imaging study is completed and as often as possible thereafter for at least one hour.
- Screen patients for clinically significant blood glucose abnormalities by obtaining a history and/or laboratory tests [see Warnings and Precautions (5.2)]. Prior to Fludeoxyglucose F 18 PET imaging in the oncology and neurology settings, instruct patient to fast for 4 to 6 hours prior to the drug's injection.
- In the cardiology setting, administration of glucose-containing food or liquids (e.g., 50 to 75 grams) prior to Fludeoxyglucose F18 Injection facilitates localization of cardiac ischemia

2.4 Radiation Dosimetry

The estimated human absorbed radiation doses (rem/mCi) to a newborn (3.4 kg), 1-year old (9.8 kg), 5-year old (19 kg), 10-year old (32 kg), 15-year old (57 kg), and adult (70 kg) from intravenous administration of Fludeoxyglucose F 18 Injection are shown in Table 1. These estimates were calculated based on human[2] data and using the data published by the International Commission on Radiological Protection[4] for Fludeoxyglucose ^{18}F. The dosimetry data show that there are slight variations in absorbed radiation dose for various organs in each of the age groups. These dissimilarities in absorbed radiation dose are due to developmental age variations (e.g., organ size, location, and overall metabolic rate for each age group). The identified critical organs (in descending order) across all age groups evaluated are the urinary bladder, heart, pancreas, spleen, and lungs.

Table 1. Estimated Absorbed Radiation Doses (rem/mCi) After Intravenous Administration of Fludeoxyglucose F-18 Injection[a]

Organ	Newborn	1-year old	5-year old	10-year old	15-year old	Adult
	(3.4 kg)	(9.8 kg)	(19 kg)	(32 kg)	(57 kg)	(70 kg)
Bladder wall[b]	4.3	1.7	0.93	0.60	0.40	0.32
Heart wall	2.4	1.2	0.70	0.44	0.29	0.22
Pancreas	2.2	0.68	0.33	0.25	0.13	0.096
Spleen	2.2	0.84	0.46	0.29	0.19	0.14
Lungs	0.96	0.38	0.20	0.13	0.092	0.064
Kidneys	0.81	0.34	0.19	0.13	0.089	0.074
Ovaries	0.80	0.8	0.19	0.11	0.058	0.053
Uterus	0.79	0.35	0.19	0.12	0.076	0.062
LLI wall *	0.69	0.28	0.15	0.097	0.060	0.051
Liver	0.69	0.31	0.17	0.11	0.076	0.058
Gallbladder wall	0.69	0.26	0.14	0.093	0.059	0.049
Small intestine	0.68	0.29	0.15	0.096	0.060	0.047
ULI wall **	0.67	0.27	0.15	0.090	0.057	0.046
Stomach wall	0.65	0.27	0.14	0.089	0.057	0.047
Adrenals	0.65	0.28	0.15	0.095	0.061	0.048
Testes	0.64	0.27	0.14	0.085	0.052	0.041
Red marrow	0.62	0.26	0.14	0.089	0.057	0.047
Thymus	0.61	0.26	0.14	0.086	0.056	0.044
Thyroid	0.61	0.26	0.13	0.080	0.049	0.039
Muscle	0.58	0.25	0.13	0.078	0.049	0.039
Bone surface	0.57	0.24	0.12	0.079	0.052	0.041
Breast	0.54	0.22	0.11	0.068	0.043	0.034
Skin	0.49	0.20	0.10	0.060	0.037	0.030
Brain	0.29	0.13	0.09	0.078	0.072	0.070
Other tissues	0.59	0.25	0.13	0.083	0.052	0.042

[a] MIRDOSE 2 software was used to calculate the radiation absorbed dose. Assumptions on the biodistribution based on data from Gallagher et al.1 and Jones et al.2

[b] The dynamic bladder model with a uniform voiding frequency of 1.5 hours was used.
*LLI = lower large intestine; **ULI = upper large intestine

2.5 Radiation Safety – Drug Handling

- Use waterproof gloves, effective radiation shielding, and appropriate safety measures when handling Fludeoxyglucose F 18 Injection to avoid unnecessary radiation exposure to the patient, occupational workers, clinical personnel and other persons.
- Radiopharmaceuticals should be used by or under the control of physicians who are qualified by specific training and experience in the safe use and handling of radionuclides, and whose experience and training have been approved by the appropriate governmental agency authorized to license the use of radionuclides.
- Calculate the final dose from the end of synthesis (EOS) time using proper radioactive decay factors. Assay the final dose in a properly calibrated dose calibrator before administration to the patient [see Description (11.2)].
- The dose of Fludeoxyglucose F 18 used in a given patient should be minimized consistent with the objectives of the procedure, and the nature of the radiation detection devices employed.

2.6 Drug Preparation and Administration

Calculate the necessary volume to administer based on calibration time and dose.
Aseptically withdraw Fludeoxyglucose F 18 Injection from its container.
Inspect Fludeoxyglucose F 18 Injection visually for particulate matter and discoloration before administration, whenever solution and container permit.
Do not administer the drug if it contains particulate matter or discoloration; dispose of these unacceptable or unused preparations in a safe manner, in compliance with applicable regulations. Use Fludeoxyglucose F 18 Injection within 12 hours from the EOS.

2.7 Imaging Guidelines

Initiate imaging within 40 minutes following Fludeoxyglucose F 18 Injection administration.
Acquire static emission images 30 to 100 minutes from the time of injection.

3 DOSAGE FORMS AND STRENGTHS

Multiple-dose 30 mL and 50 mL glass vial containing 0.74 to 7.40 GBq/mL (20 to 200 mCi/mL) of Fludeoxyglucose F 18 Injection and 4.5 mg of sodium chloride with 0.1 to 0.5% w/w ethanol as a stabilizer (approximately 15 to 50 mL volume) for intravenous administration.

4 CONTRAINDICATIONS

None

5 WARNINGS AND PRECAUTIONS

5.1 Radiation Risks

Radiation-emitting products, including Fludeoxyglucose F 18 Injection, may increase the risk for cancer, especially in pediatric patients. Use the smallest dose necessary for imaging and ensure safe handling to protect the patient and health care worker [see Dosage and Administration (2.5)].

5.2 Blood Glucose Abnormalities

In the oncology and neurology setting, suboptimal imaging may occur in patients with inadequately regulated blood glucose levels. In these patients, consider medical therapy and laboratory testing to assure at least two days of normoglycemia prior to Fludeoxyglucose F 18 Injection administration.

6 ADVERSE REACTIONS

Hypersensitivity reactions with pruritus, edema and rash have been reported in the post-marketing setting. Have emergency resuscitation equipment and personnel immediately available.

7 DRUG INTERACTIONS

The possibility of interactions of Fludeoxyglucose F 18 Injection with other drugs taken by patients undergoing PET imaging has not been studied.

8 USE IN SPECIFIC POPULATIONS

8.1 Pregnancy

Pregnancy Category C
Animal reproduction studies have not been conducted with Fludeoxyglucose F 18 Injection.
It is also not known whether Fludeoxyglucose F 18 Injection can cause fetal harm when administered to a pregnant woman or can affect reproduction capacity. Consider alternative diagnostic tests in a pregnant woman; administer Fludeoxyglucose F 18 Injection only if clearly needed.

8.3 Nursing Mothers

It is not known whether Fludeoxyglucose F 18 Injection is excreted in human milk. Consider alternative diagnostic tests in women who are breast-feeding. Use alternatives to breast feeding (e.g., stored breast milk or infant formula) for at least 10 half-lives of radioactive decay, if Fludeoxyglucose F 18 Injection is administered to a woman who is breast-feeding.

8.4 Pediatric Use

The safety and effectiveness of Fludeoxyglucose F 18 Injection in pediatric patients with epilepsy is established on the basis of studies in adult and pediatric patients. In pediatric patients with epilepsy, the recommended dose is 2.6 mCi. The optimal dose adjustment on the basis of body size or weight has not been determined. In the oncology or cardiology settings, the safety and effectiveness of Fludeoxyglucose F 18 Injection have not been established in pediatric patients.

11 DESCRIPTION

11.1 Chemical Characteristics

Fludeoxyglucose F 18 Injection is a positron emitting radiopharmaceutical that is used for diagnostic purposes in conjunction with positron emission tomography (PET) imaging. The active ingredient 2-deoxy-2-[^{18}F]fluoro-D-glucose has the molecular formula of $C_6H_{11}{}^{18}FO_5$ with a molecular weight of 181.26, and has the following chemical structure:

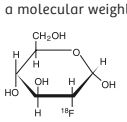

Fludeoxyglucose F 18 Injection is provided as a ready to use sterile, pyrogen free, clear, colorless solution. Each mL contains between 0.740 to 7.40GBq (20.0 to 200 mCi) of 2-deoxy-2-[^{18}F]fluoro-D-glucose at the EOS, 4.5 mg of sodium chloride and 0.1 to 0.5% w/w ethanol as a stabilizer. The pH of the solution is between 4.5 and 7.5. The solution is packaged in a multiple-dose glass vial and does not contain any preservative.

11.2 Physical Characteristics

Fluorine F 18 decays by emitting positron to Oxygen O 16 (stable) and has a physical half-life of 109.7 minutes. The principal photons useful for imaging are the dual 511 keV gamma photons, that are produced and emitted simultaneously in opposite direction when the positron interacts with an electron (Table 2).

Table 2. Pricipal Radiation Emission Data for Fluorine F18

Radiation/Emission	% Per Disintegration	Mean Energy
Positron (b+)	96.73	249.8 keV
Gamma (±)*	193.46	511.0 keV

*Produced by positron annihilation
From: Kocher, D.C. Radioactive Decay Tables DOE/TIC-I 1026, 89 (1981)
The specific gamma ray constant (point source air kerma coefficient) for fluorine F 18 is 5.7 R/hr/mCi (1.35 x 10-6 Gy/hr/kBq) at 1 cm. The half-value layer (HVL) for the 511 keV photons is 4 mm lead (Pb). The range of attenuation coefficients for this radionuclide as a function of lead shield thickness is shown in Table 3. For example, the interposition of an 8 mm thickness of Pb, with a coefficient of attenuation of 0.25, will decrease the external radiation by 75%.

Table 3. Radiation Attenuation of 511 keV Photons by lead (Pb) shielding

Shield thickness (Pb) mm	Coefficient of attenuation
0	0.00
4	0.50
8	0.25
13	0.10
26	0.01
39	0.001
52	0.0001

For use in correcting for physical decay of this radionuclide, the fractions remaining at selected intervals after calibration are shown in Table 4.

Table 4. Physical Decay Chart for Fluorine F18

Minutes	Fraction Remaining
0*	1.000
15	0.909
30	0.826
60	0.683
110	0.500
220	0.250

*calibration time

12 CLINICAL PHARMACOLOGY

12.1 Mechanism of Action

Fludeoxyglucose F 18 is a glucose analog that concentrates in cells that rely upon glucose as an energy source, or in cells whose dependence on glucose increases under pathophysiological conditions. Fludeoxyglucose F 18 is transported through the cell membrane by facilitative glucose transporter proteins and is phosphorylated within the cell to [18F] FDG-6-phosphate by the enzyme hexokinase. Once phosphorylated it cannot exit until it is dephosphorylated by glucose-6-phosphatase. Therefore, within a given tissue or pathophysiological process, the retention and clearance of Fludeoxyglucose F 18 reflect a balance involving glucose transporter, hexokinase and glucose-6-phosphatase activities. When allowance is made for the kinetic differences between glucose and Fludeoxyglucose F 18 transport and phosphorylation (expressed as the ‚'lumped constant'' ratio), Fludeoxyglucose F 18 is used to assess glucose metabolism. In comparison to background activity of the specific organ or tissue type, regions of decreased or absent uptake of Fludeoxyglucose F 18 reflect the decrease or absence of glucose metabolism. Regions of increased uptake of Fludeoxyglucose F 18 reflect greater than normal rates of glucose metabolism.

12.2 Pharmacodynamics

Fludeoxyglucose F 18 Injection is rapidly distributed to all organs of the body after intravenous administration. After background clearance of Fludeoxyglucose F 18 Injection, optimal PET imaging is generally achieved between 30 to 40 minutes after administration. In cancer, the cells are generally characterized by enhanced glucose metabolism partially due to (1) an increase in activity of glucose transporters, (2) an increased rate of phosphorylation activity, (3) a reduction of phosphatase activity or, (4) a dynamic alteration in the balance among all these processes. However, glucose metabolism of cancer as reflected by Fludeoxyglucose F 18 accumulation shows considerable variability. Depending on tumor type, stage, and location, Fludeoxyglucose F 18 accumulation may be increased, normal, or decreased. Also, inflammatory cells can have the same variability of uptake of Fludeoxyglucose F 18.
In the heart, under normal aerobic conditions, the myocardium meets the bulk of its energy requirements by oxidizing free fatty acids. Most of the exogenous glucose taken up by the myocyte is converted into glycogen. However, under ischemic conditions, the oxidation of free fatty acids decreases, exogenous glucose becomes the preferred myocardial sub strate, glycolysis is stimulated, and glucose taken up by the myocyte is metabolized immediately instead of being converted into glycogen. Under these conditions, phosphorylated Fludeoxyglucose F 18 accumulates in the myocyte and can be detected with PET imaging.
In the brain, cells normally rely on aerobic metabolism. In epilepsy, the glucose metabolism varies. Generally, during a seizure, glucose metabolism increases. Interictally, the seizure focus tends to be hypometabolic.

12.3 Pharmacokinetics

Distribution: In four healthy male volunteers, receiving an intravenous administration of 30 seconds in duration, the arterial blood level profile for Fludeoxyglucose F 18 decayed triexponentially. The effective half-life ranges of the three phases were 0.2 to 0.3 minutes, 10 to 13 minutes with a mean and standard deviation (STD) of 11.6 (±) 1.1 min, and 80 to 95 minutes with a mean and STD of 88 (±) 4 min. Plasma protein binding of Fludeoxyglucose F 18 has not been studied.
Metabolism: Fludeoxyglucose F 18 is transported into cells and phosphorylated to [18F]-FDG-6-phosphate at a rate proportional to the rate of glucose utilization within that tissue. [F18]-FDG-6-phosphate presumably is metabolized to 2-deoxy-2-[F18]fluoro-6-phospho-D-mannose([F 18]FDM-6-phosphate).

Fludeoxyglucose F 18 Injection may contain several impurities (e.g., 2-deoxy-2-chloro-D-glucose (ClDG)). Biodistribution and metabolism of ClDG are presumed to be similar to Fludeoxyglucose F 18 and would be expected to result in intracellular formation of 2-deoxy-2-chloro-6-phospho-D-glucose (ClDG-6-phosphate) and 2-deoxy-2-chloro-6-phospho-D-mannose (ClDM-6-phosphate). The phosphorylated deoxyglucose compounds are dephosphorylated and the resulting compounds (FDG, FDM, ClDG, and ClDM) presumably leave cells by passive diffusion. Fludeoxyglucose F 18 and related compounds are cleared from non-cardiac tissues within 3 to 24 hours after administration. Clearance from the cardiac tissue may require more than 96 hours. Fludeoxyglucose F 18 that is not involved in glucose metabolism in any tissue is then excreted in the urine.

Elimination: Fludeoxyglucose F 18 is cleared from most tissues within 24 hours and can be eliminated from the body unchanged in the urine. Three elimination phases have been identified in the reviewed literature. Within 33 minutes, a mean of 3.9% of the administrated radioactive dose was measured in the urine. The amount of radiation exposure of the urinary bladder at two hours post-administration suggests that 20.6% (mean) of the radioactive dose was present in the bladder.

Special Populations: The pharmacokinetics of Fludeoxyglucose F 18 Injection have not been studied in renally-impaired, hepatically impaired or pediatric patients. Fludeoxyglucose F 18 is eliminated through the renal system. Avoid excessive radiation exposure to this organ system and adjacent tissues. The effects of fasting, varying blood sugar levels, conditions of glucose intolerance, and diabetes mellitus on Fludeoxyglucose F 18 distribution in humans have not been ascertained [see Warnings and Precautions (5.2)].

13 NONCLINICAL TOXICOLOGY

13.1 Carcinogenesis, Mutagenesis, Impairment of Fertility

Animal studies have not been performed to evaluate the Fludeoxyglucose F 18 Injection carcinogenic potential, mutagenic potential or effects on fertility.

14 CLINICAL STUDIES

14.1 Oncology

The efficacy of Fludeoxyglucose F 18 Injection in positron emission tomography cancer imaging was demonstrated in 16 independent studies. These studies prospectively evaluated the use of Fludeoxyglucose F 18 in patients with suspected or known malignancies, including non-small cell lung cancer, colo-rectal, pancreatic, breast, thyroid, melanoma, Hodgkin's and non-Hodgkin's lymphoma, and various types of metastatic cancers to lung, liver, bone, and axillary nodes. All these studies had at least 50 patients and used pathology as a standard of truth. The Fludeoxyglucose F 18 Injection doses in the studies ranged from 200 MBq to 740 MBq with a median and mean dose of 370 MBq. In the studies, the diagnostic performance of Fludeoxyglucose F 18 Injection varied with the type of cancer, size of cancer, and other clinical conditions. False negative and false positive scans were observed. Negative Fludeoxyglucose F 18 Injection PET scans do not exclude the diagnosis of cancer. Positive Fludeoxyglucose F 18 Injection PET scans can not replace pathology to establish a diagnosis of cancer. Non-malignant conditions such as fungal infections, inflammatory processes and benign tumors have patterns of increased glucose metabolism that may give rise to false-positive scans. The efficacy of Fludeoxyglucose F 18 Injection PET imaging in cancer screening was not studied.

14.2 Cardiology

The efficacy of Fludeoxyglucose F 18 Injection for cardiac use was demonstrated in ten independent, prospective studies of patients with coronary artery disease and chronic left ventricular systolic dysfunction who were scheduled to undergo coronary revascularization. Before revascularization, patients underwent PET imaging with Fludeoxyglucose F 18 Injection (74 to 370 MBq, 2 to 10 mCi) and perfusion imaging with other diagnostic radiopharmaceuticals. Doses of Fludeoxyglucose F 18 Injection ranged from 74 to 370 MBq (2 to 10 mCi). Segmental, left ventricular, wall-motion assessments of asynergic areas made before revascularization were compared in a blinded manner to assessments made after successful revascularization to identify myocardial segments with functional recovery. Left ventricular myocardial segments were predicted to have reversible loss of systolic function if they showed Fludeoxyglucose F 18 accumulation and reduced perfusion (i.e., flow-metabolism mismatch). Conversely, myocardial segments were predicted to have irreversible loss of systolic function if they showed reductions in both Fludeoxyglucose F 18 accumulation and perfusion (i.e., matched defects). Findings of flow-metabolism mismatch in a myocardial segment may suggest that successful revascularization will restore myocardial function in that segment. However, false-positive tests occur regularly, and the decision to have a patient undergo revascularization should not be based on PET findings alone. Similarly, findings of a matched defect in a myocardial segment may suggest that myocardial function will not recover in that segment, even if it is successfully revascularized. However, false-negative tests occur regularly, and the decision to recommend against coronary revascularization, or to recommend a cardiac transplant, should not be based on PET findings alone. The reversibility of segmental dysfunction as predicted with Fludeoxyglucose F 18 PET imaging depends on successful coronary revascularization. Therefore, in patients with a low likelihood of successful revascularization, the diagnostic usefulness of PET imaging with Fludeoxyglucose F 18 Injection is more limited.

14.3 Neurology

In a prospective, open label trial, Fludeoxyglucose F 18 Injection was evaluated in 86 patients with epilepsy. Each patient received a dose of Fludeoxyglucose F 18 Injection in the range of 185 to 370 MBq (5 to 10 mCi). The mean age was 16.4 years (range: 4 months to 58 years; of these, 42 patients were less than 12 years and 16 patients were less than 2 years old). Patients had a known diagnosis of complex partial epilepsy and were under evaluation for surgical treatment of their seizure disorder. Seizure foci had been previously identified on ictal EEGs and sphenoidal EEGs. Fludeoxyglucose F 18 Injection PET imaging confirmed previous diagnostic findings in 16% (14/87) of the patients; in 34% (30/87) of the patients, Fludeoxyglucose F 18 Injection PET images provided new findings. In 32% (27/87), imaging with Fludeoxyglucose F 18 Injection was inconclusive. The impact of these imaging findings on clinical outcomes is not known. Several other studies comparing imaging with Fludeoxyglucose F 18 Injection results to subsphenoidal EEG, MRI and/or surgical findings supported the concept that the degree of hypometabolism corresponds to areas of confirmed epileptogenic foci. The safety and effectiveness of Fludeoxyglucose F 18 Injection to distinguish idiopathic epileptogenic foci from tumors or other brain lesions that may cause seizures have not been established.

15 REFERENCES

1. Gallagher B.M., Ansari A., Atkins H., Casella V., Christman D.R., Fowler J.S., Ido T., MacGregor R.R., Som P., Wan C.N., Wolf A.P., Kuhl D.E., and Reivich M. "Radiopharmaceuticals XXVII. 18F-labeled 2-deoxy-2-fluoro-d-glucose as a radiopharmaceutical for measuring regional myocardial glucose metabolism in vivo: tissue distribution and imaging studies in animals," J Nucl Med, 1977; 18, 990-6.
2. Jones S.C., Alavi, A., Christman D., Montanez, I., Wolf, A.P., and Reivich M. "The radiation dosimetry of 2 [F-18] fluoro-2-deoxy-D-glucose in man," J Nucl Med, 1982; 23, 613-617.
3. Kocher, D.C. "Radioactive Decay Tables: A handbook of decay data for application to radiation dosimetry and radiological assessments," 1981, DOE/TIC-I 1026, 89.
4. ICRP Publication 53, Volume 18, No. l-4,1987, pages 75-76.

16 HOW SUPPLIED/STORAGE AND DRUG HANDLING

Fludeoxyglucose F 18 Injection is supplied in a multi-dose, capped 30 mL and 50 mL glass vial containing between 0.740 to 7.40 GBq/mL (20 to 200 mCi/mL), of no carrier added 2-deoxy-2-[F 18] fluoro-D-glucose, at end of synthesis, in approximately 15 to 50 mL. The contents of each vial are sterile, pyrogen-free and preservative-free.

NDC 40028-511-30; 40028-511-50

Receipt, transfer, handling, possession, or use of this product is subject to the radioactive material regulations and licensing requirements of the U.S. Nuclear Regulatory Commission, Agreement States or Licensing States as appropriate.

Store the Fludeoxyglucose F 18 Injection vial upright in a lead shielded container at 25°C (77°F); excursions permitted to 15-30°C (59-86°F).

Store and dispose of Fludeoxyglucose F 18 Injection in accordance with the regulations and a general license, or its equivalent, of an Agreement State or a Licensing State.

The expiration date and time are provided on the container label. Use Fludeoxyglucose F 18 Injection within 12 hours from the EOS time.

17 PATIENT COUNSELING INFORMATION

Instruct patients in procedures that increase renal clearance of radioactivity.

Encourage patients to:

- drink water or other fluids (as tolerated) in the 4 hours before their PET study.
- void as soon as the imaging study is completed and as often as possible thereafter for at least one hour.

Manufactured by: PETNET Solutions Inc.
810 Innovation Drive
Knoxville, TN 37932

Distributed by: PETNET Solutions Inc.
810 Innovation Drive
Knoxville, TN 37932

PETNET Solutions

PN0002262 Rev. A

March 1, 2011

Combined ^{18}F-FDG PET/MR in the Diagnostic Work-up of Myocardial Disease

Maria Giovanna Trivieri, M.D., Ph.D.[1,4]; Marc R. Dweck, M.D., Ph.D.[1,2]; Philip M. Robson, Ph.D.[1]; Nicolas A. Karakatsanis, Ph.D.[1]; Ronan Abgral, M.D., Ph.D.[1,3]; Zahi A. Fayad, Ph.D.[1]

[1] Translational and Molecular Imaging Institute, Icahn School of Medicine at Mount Sinai, New York, NY, USA
[2] British Heart Foundation / University Centre for Cardiovascular Science, University of Edinburgh, UK
[3] Department of Nuclear Medicine, European University of Brittany, Centre Hospitalier Régional et Universitaire (CHRU) Brest, France
[4] Cardiovascular Institute, Icahn School of Medicine at Mount Sinai, New York, NY, USA

Introduction

Cardiovascular magnetic resonance (CMR) is an established modality frequently used to diagnose a variety of cardiomyopathic processes. It relies on the characteristic appearances of the myocardium on late gadolinium enhancement (LGE) images coupled with detailed morpho-functional assessment [1, 2]. Positron Emission Tomography (PET) on the other hand, offers information on disease activity and as such is complementary to CMR. In the cardiovascular field, ^{18}F-Fludeoxyglucose (FDG)[1] has been employed to study inflammation in the myocardium [3–5]. PET is usually coupled with computed tomography (CT) to provide anatomical and attenuation information. Consequently, assessment of data from CMR and PET, often collected on different days, must be done by image registration and is often challenging.

With the advent of hybrid PET/MR systems, we have now the unprecedented opportunity to combine the versatility of CMR with functional molecular imaging [6]. The simultaneous acquisition of PET and CMR data enables accurate co-registration of complementary data within the

[1] The full prescribing information for the Fludeoxyglucose F18 injection can be found at page 37.

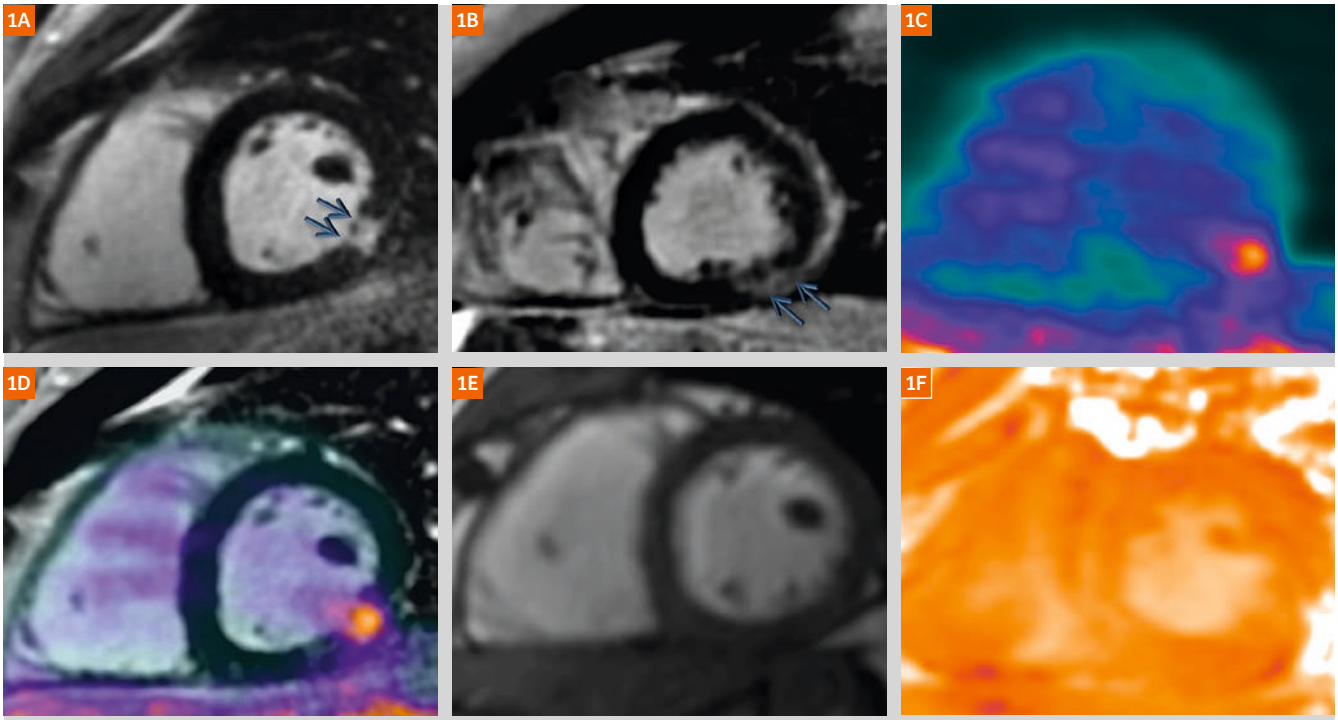

Figure 1: Two-chamber short-axis view of the right and left ventricles showing a discrete area of LGE in the infero-lateral wall (blue arrows) **(1A–B).** Focal increase in FDG nearing the inferior wall of the myocardium and adjacent to the liver as seen in the PET alone **(1C).** Fused FDG-PET/MR images showing increased FDG signal perfectly localized to area of LGE **(1D).** Two-chamber short-axis cine CMR showing mild hypokinesis of the infero-lateral wall **(1E).** Native CMR T2 mapping **(1F).**

myocardium or area of LGE and allows differentiation of the signal in these areas from activity in the blood pool or surrounding tissues. Moreover, compared to PET/CT, PET/MR has the advantage of reducing the radiation exposure.

In this report, we present one clinical case where the addition of PET/MR resolved the initial uncertainty about both the etiology of the clinical presentation and the activity of the underlying disease process.

Clinical presentation

A 50-year-old man without prior medical history was hospitalized for recent onset of chest pain and shortness of breath. On arrival to the Emergency Department, he was found to have elevated cardiac biomarkers (CK and Troponin) and 1–2 mm inferior ST elevation on the ECG. Coronary angiogram was normal. Contrast CT of the chest showed no evidence of pulmonary embolism, pulmonary pathology or lymphadenopathy. A combined PET/MR study was requested to assess for wall motion abnormalities, myocardial damage and inflammation.

PET/MR imaging

Simultaneous PET and MR imaging of the heart was performed on the Biograph mMR hybrid PET/MR system (Siemens Healthcare, Erlangen, Germany) using a flexible 6-channel body arrayed-receiver coil and 6 channels of the 16-ch spine arrayed-receiver coil mounted in the scanner table. Dynamic PET data was acquired in list-mode using a 90 min bedtime, starting 10 min following administration of 5 MBq/kg of ^{18}F-FDG. The last 30 min were binned to produce a static image for evaluation. The MR protocol included long and short-axis cine imaging, late gadolinium enhancement (10 min following administration 0.02 mmol/kg Multihance (Bracco Diagnostics, Milan, Italy)) and native T2 mapping. Image analysis was performed on fused, co-registered static PET and CMR LGE images. In preparation for the scan, the patient was asked to follow a carbohydrate-free and high-fat diet for 24 hours, and fast for at least 12 hours prior to the study, to suppress the high physiological uptake of ^{18}F-FDG naturally present in the myocardium.

Findings

CMR revealed normal biventricular size. Mild hypokinesis was observed in the mid infero-lateral wall but overall systolic function was preserved (EF 60%). On LGE imaging, there was a very discrete area of subepicardial/transmural myocardial scar in the mid infero-lateral wall (Figs. 1A, B and E); this pattern was felt to be consistent with a diagnosis of myocarditis rather than myocardial infarction. When the PET data was viewed in isolation, a focal area of increased ^{18}F-FDG uptake was observed near the inferior wall of the myocardium, although it was adjacent to the liver and not clear that it was originating from the myocardium (Fig. 1C). After image fusion with CMR, the increased PET activity perfectly co-localized with the region of injury on LGE (Fig. 1D) allowing us to report active myocardial inflammation in that area with confidence. By contrast, no clear increase in signal was observed on the T2 mapping images in this region (Fig. 1F).

Impression

In the absence of coronary artery disease and prior medical history, our PET/MR findings were felt to be consistent with a diagnosis of active myocarditis.

Conclusion

Simultaneous acquisition of PET and MR data offers valuable and complementary clinical information. On the same scan, the pattern of injury can be carefully co-localised to disease activity providing a unique method for combining anatomical and dynamic functional imaging. With the rapid development of novel PET radiotracers and CMR techniques for imaging the function and structure of the heart, hybrid PET/MR systems have the potential to further improve diagnostic accuracy and provide insight into the variety of molecular pathways and mechanisms underlying myocardial disease in our patients.

References

1 Fieno, D.S., et al., Contrast-enhanced magnetic resonance imaging of myocardium at risk: distinction between reversible and irreversible injury throughout infarct healing. J Am Coll Cardiol, 2000. 36(6): p. 1985-91.
2 Kim, R.J., et al., Relationship of MRI delayed contrast enhancement to irreversible injury, infarct age, and contractile function. Circulation, 1999. 100(19): p. 1992-2002.
3 Dweck, M.R., et al., Imaging of coronary atherosclerosis – evolution towards new treatment strategies. Nat Rev Cardiol, 2016.
4 Rudd, J.H., et al., Imaging atherosclerotic plaque inflammation with [18F]-fluorodeoxyglucose positron emission tomography. Circulation, 2002. 105(23): p. 2708-11.
5 Abgral, R., et al., Clinical Utility of Combined FDG-PET/MR to Assess Myocardial Disease. JACC Cardiovasc Imaging, 2016.
6 Vesey, A.T., M.R. Dweck, and Z.A. Fayad, Utility of Combining PET and MR Imaging of Carotid Plaque. Neuroimaging Clin N Am, 2016. 26(1): p. 55-68.

Contact

Zahi A. Fayad, Ph.D, FAHA, FACC, FISMRM

Icahn School of Medicine at Mount Sinai

Mount Sinai Endowed Chair in Medical Imaging and Bioengineering

Professor of Radiology and Medicine (Cardiology)

Director, Translational and Molecular Imaging Institute

Director, Cardiovascular Imaging Research

Vice-Chair for Research, Department of Radiology

One Gustave L. Levy Place
Box 1234
New York, NY 10029-6574
USA
Phone: +1 212 824 8452
Fax: +1 240 368 8096
zahi.fayad@mssm.edu

Free-breathing Late Enhancement Imaging: Phase Sensitive Inversion Recovery (PSIR) with Respiratory Motion Corrected (MOCO) Averaging

Peter Kellman; Hui Xue; Michael S. Hansen

National Heart, Lung, and Blood Institute, National Institutes of Health, DHHS, Bethesda, MD, USA

Introduction

Late gadolinium enhancement (LGE) has become a gold standard in myocardial viability assessment [1, 2] providing excellent depiction of myocardial infarction (MI) and macroscopic scarring. The use of late enhancement in the diagnosis of ischemic heart disease and in guiding revascularization therapy has gained wide acceptance. More recently, late enhancement has been playing a broader role in characterizing fibrosis in non-ischemic cardiomyopathies [3,4], and in measurement of scar resulting from treatment of cardiac arrhythmias using radiofrequency ablation [5]. As the use of late enhancement imaging has matured and as the span of applications has widened, clinicians are examining late enhancement images for more subtle indication of fibrosis and the demands on image quality have grown [6].

Breath-held (BH), segmented FLASH has been the gold standard for LGE for many years [7] and is widely used with great success when patients are cooperative and can hold their breath. In instances where poor breath-holding results in ghost artifacts, single shot SSFP imaging has been used as an alternative. However, while single shot imaging mitigates ghosting artifacts, it generally has compromised spatial resolution and image quality compared to BH FLASH. Therefore, the single shot approaches are less sensitive to detection of subtle LGE and to detection of small lesions [8]. The development of PSIR LGE with respiratory motion corrected (MOCO) averaging[1] [6, 9, 10] has led to a free-breathing (FB) approach which achieves the robustness of single shot approaches and the resolution and image quality of BH segmented FLASH. In addition to elimination of ghosting artifacts due to poor breath-holds (Fig. 1), the PSIR MOCO LGE is inherently less sensitive to arrhythmias.

In addition to being easier on the patients, free-breathing PSIR MOCO LGE eliminates pauses between BH slices and is therefore faster to acquire than a BH stack. Free-breathing, MOCO LGE greatly simplifies the clinical workflow, particularly since LGE is typically at the end of the study where patient compliance is frequently a problem. PSIR MOCO LGE has been demonstrated to improve the image quality in both pediatric[2] [11] and adult populations [12]. It has been shown to make a significant improvement in the most vulnerable population of sick patients [12].

1

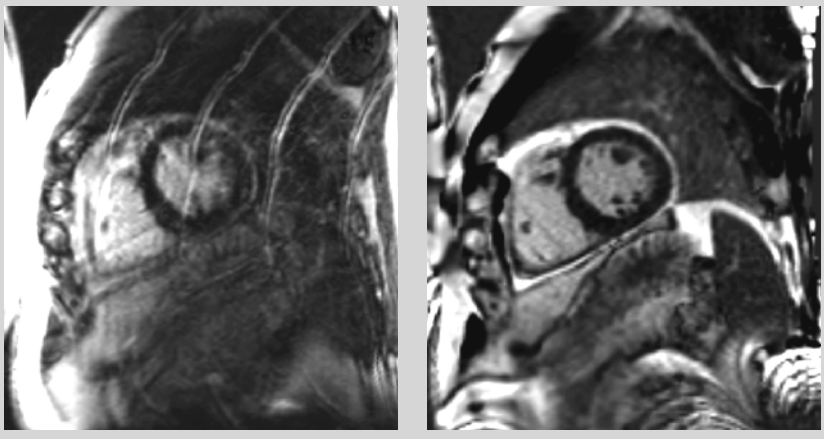

Figure 1: Free-breathing, MOCO PSIR LGE images eliminate ghosting artifacts and achieve high SNR by means of respiratory motion corrected averaging [6].

[1] The product is still under development and not commercially available yet. Its future availability cannot be ensured.

[2] MR scanning has not been established as safe for imaging fetuses and infants less than two years of age. The responsible physician must evaluate the benefits of the MR examination compared to those of other imaging procedures.

In a study of 390 consecutive patients [12], it was concluded that: "Myocardial infarction detection and quantification are similar between MOCO-LGE and BH-LGE when BH-LGE can be acquired well, but BH-LGE quality deteriorates with patient vulnerability. Acquisition time, image quality, diagnostic confidence, and the number of successfully scanned patients are superior with MOCO-LGE, which extends LGE-based risk stratification to include patients with vulnerability confirmed by outcomes." A number of sites have adopted PSIR MOCO LGE as their sole means of LGE imaging and combined they have been performing over 10,000 studies annually for the past several years.

Respiratory MOCO averaging can offer SNR improvements well beyond what is possible using BH FLASH by further increasing the number of averages. Therefore, with PSIR MOCO LGE, higher spatial resolution or thinner slices are achievable in clinical practice. Furthermore, PSIR MOCO LGE has been integrated with dark blood PSIR to provide improved contrast of subendocardial MI with the adjacent bright blood pool.

Free-breathing approach

Motion correction may be used to correct respiratory motion [9, 10] in the case of free-breathing acquisition, or diaphragmatic drift in the case of breath-holding. The SNR for individual single shot PSIR-SSFP images is slightly worse than segmented PSIR-FLASH due to the increase in bandwidth, despite the increase in flip angle. However, the SNR of single shot PSIR-SSFP may be significantly improved by averaging multiple repeated measurements (Fig. 2). Typically, using 8 PSIR images acquired in 16 heartbeats provides an SNR comparable or better than the FLASH protocol for approximately the same duration and may be extended to a larger number of averages since the acquisition is not breath-held. Parallel imaging at higher acceleration factors may be used to reduce the imaging duration in diastole to achieve higher spatial resolution or reduce motion blur at higher heart rates. Use of non-rigid motion correction provides correction over the full FOV in a fully automated fashion. Selective averaging may be used to discard images that do not meet similarity criteria due to through plane motion [10]. This retrospective image based navigator strategy is robust and simple to use, thereby eliminating the complexity and unreliability of prospective navigators.

Key points/implications:

- Free-breathing imaging is easier for the patient
- Improves clinical workflow
- Free-breathing imaging reduces artifacts
- Improves diagnostic quality
- Is highly effective for the most vulnerable population

2

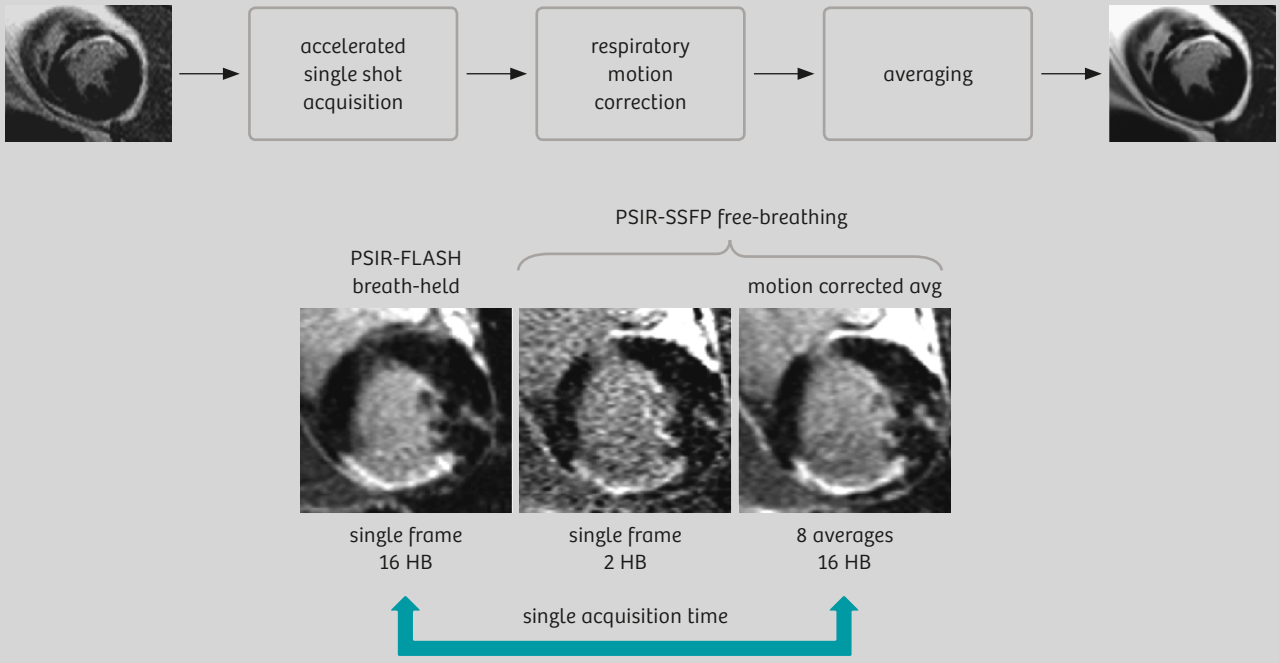

Figure 2: Respiratory motion corrected averaging strategy using accelerated single shot imaging to mitigate artifacts and motion corrected averaging to increase SNR [6].

Imaging protocols

PSIR MOCO LGE has been integrated with a number of imaging protocols to include SSFP, FLASH, and multi-echo GRE for water fat separated LGE, and dark blood (DB) PSIR LGE (Fig. 3). Typical parameters for these protocols are listed in Table 1. Additionally, early gadolinium enhancement (EGE) protocols use reduced averaging for more rapid multi-slice coverage, and higher spatial resolution protocols (e.g. 256 x 224 or 320 x 244) use higher parallel imaging acceleration (PAT) factors and increased averaging.

3

Figure 3: Simplified diagram of sequence for PSIR LGE with interleaved acquisition of IR and PD images on alternate heartbeats (top) and dark blood (DB) PSIR LGE using IR-T2 RF preparation. Readout may be single-shot SSFP, FLASH, or multi-echo GRE for water fat separated PSIR LGE imaging.

	Bright Blood (BB)		Dark Blood (DB)	Fat Water (FW)
Preparation	Inversion Preparation		Inversion Preparation & T2 preparation	Inversion Preparation
Readout (single shot)	SSFP FA_{IR} = 50° FA_{PD} = 8°	FLASH FA_{IR} = 10° FA_{PD} = 5°	SSFP FA_{IR} = 50° FA_{PD} = 8°	3-echo GRE (FA_{IR} = 25°, FA_{PD} = 5°) monopolar readout
Typical FOV / resolution	360 x 270 mm² 1.4 x 1.9 x 8 mm³			360 x 270 mm² 1.4 x 2.2 x 8 mm³
Matrix size	256 x 144 (parallel imaging factor 2)			256 x 123 (parallel imaging factor 3)
Number of acquired measurements	8		16	9
T2 prep TE	n/a		10–40 ms	n/a
TE / TR	1.2/2.8 ms	1.25/3.1 ms	1.2/2.8 ms	(1.5,3.8, 6.1)/7.2 ms
ECG triggering	Inversions every 2 RR (HR < 90 bpm) Inversions every 3 RR (HR > 90 bpm)			

Table 1: Typical imaging parameters for various PSIR LGE MOCO protocols.

PSIR motion corrected averaging

Non-rigid image registration is used to correct respiratory motion between repeated measurements acquired during normal free-breathing PSIR LGE imaging [6, 9, 10]. The motion correction (MOCO) is done independently for the IR and proton density (PD) images and the MOCO averaged complex images are co-registered prior to the PSIR demodulation step (Fig. 4, current implementation). The non-rigid image registration corrects in-plane motion and through-plane motion is dealt with by discarding 50% of the acquired measurements which are most dissimilar. The selection of the reference frame used for image registration as well as which frames to be discarded is based on the similarity of frames as estimated from a global mean square difference metric [10]. In this way, the retrospective image-based strategy averages the most frequent respiratory phase which is typically at end-expiration. The co-registered MOCO PD image is used for both PSIR demodulation, which preserves the sign of the IR signal by removing the background phase, as well as for correcting the surface coil intensity roll-off (Fig. 5). To improve the reliability of IR/PD co-registration which is critical for both PSIR demodulation and surface coil intensity correction, a volume preserving non-rigid co-registration is used to deal with the challenge of different contrasts between IR and PD images.

In dark blood imaging protocols SNR is typically lower due to T2 weighting and more averages are needed compared to the bright blood PSIR MOCO protocol. Likewise, for higher spatial resolution with higher PAT factors and smaller voxels, the loss in SNR in raw images may be compensated for by increased averaging.

Implementation

The PSIR MOCO implementation has evolved over the last several years and has achieved high quality and reliability used at a large number of sites in their clinical workflow. Initial off-line implementations [9, 10] were quickly moved to the scanner as works-in-progress (WIP) packages as part

4

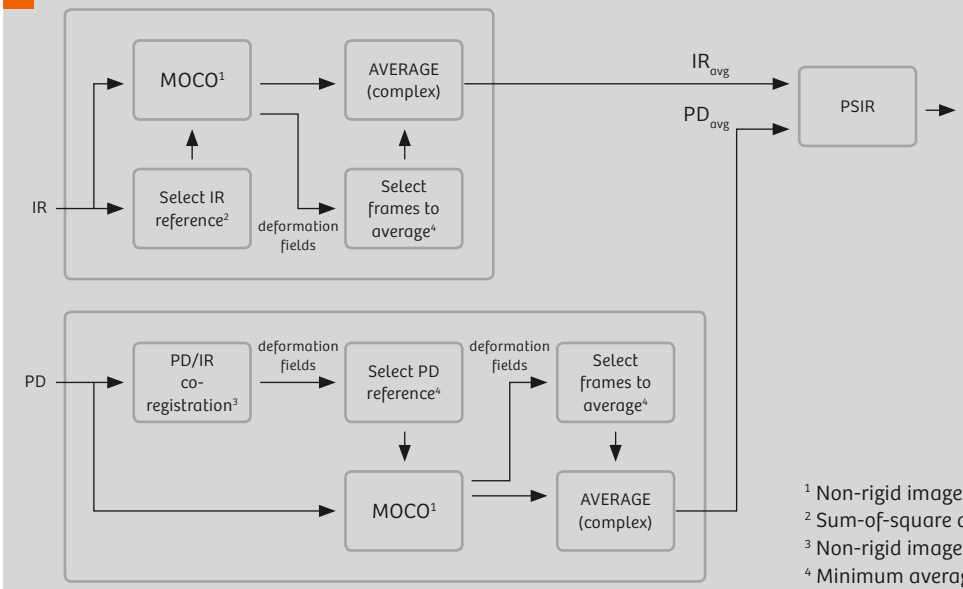

Figure 4:
Current strategy for free-breathing, respiratory motion corrected averaging and PSIR demodulation.

[1] Non-rigid image registration
[2] Sum-of-square difference method
[3] Non-rigid image registration with volume preservation
[4] Minimum average deformation method

5

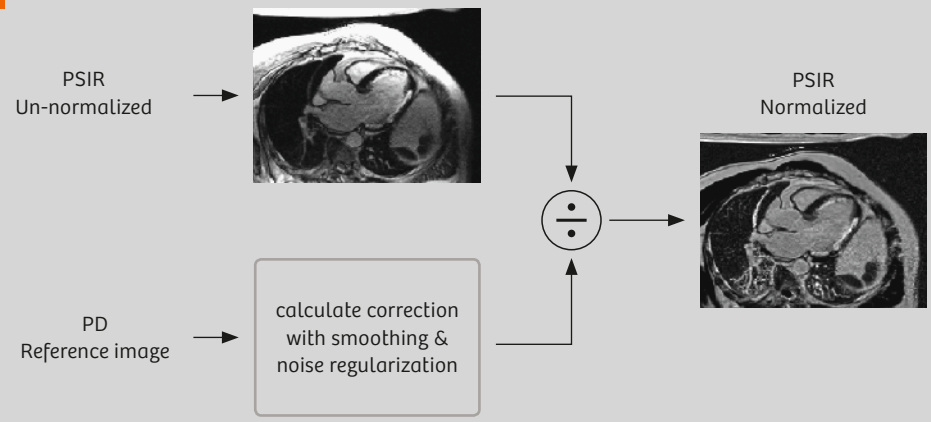

Figure 5:
Correction of surface coil intensity roll-off used the proton density (PD) magnitude image after MOCO averaging.

of co-development between NIH and Siemens under a cooperative research and development agreement (CRADA). Initial WIPs began in 2007 with WIP 373 (*syngo* MR B13A) for MAGNETOM Avanto and Espree, and were re-released with various improvements over the ensuing years.

Initial implementations applied respiratory MOCO and averaging directly to the individual single shot SSFP images, and significant through plane motion was dealt with by discarding frames as described above. Subsequent development applied MOCO averaging independently to the IR and PD, and performed the PSIR between IR and PD after motion corrected averaging. This mitigated artifacts arising due to respiratory motion between IR and PD. Early versions would output a number of intermediate series to include the raw images, MOCO images, as well the averages. As the development matured, the final versions output only the MOCO average.

A recent development has been the implementation of the PSIR MOCO reconstruction using the Gadgetron image reconstruction framework [13]. The Gadgetron framework provides increased speed and 'on-the-fly' reconstruction for multi-slice acquisitions. On-the-fly reconstruction immediately starts the computation when the image acquisition of the first slice is completed. For a scan covering multiple slices, this scheme allows image display during the acquisition of a stack of slices. Gadgetron software may be installed on the *syngo* MR E11 platforms (1.5T MAGNETOM Aera, 3T MAGNETOM Skyra and Prisma) to run on the scanner's image reconstruction computer (MARS) or may be run on an external computer connected over the network (currently a C2P with NIH research collaboration partners). Using on-the-fly reconstruction, the time to complete the full stack of slices (9 slices/8 measurements) is approximately 6 or 8 seconds after completion of the acquisition, when performed on a 24 core external Linux PC or 16 core MARS, respectively. For on-the-fly reconstruction, all measurements for a given slice are acquired consecutively (inner loop).

PSIR MOCO LGE

Free-breathing PSIR MOCO LGE protocols are now widely used at a number of clinical research sites. At many of these sites, the free-breathing protocol is used exclusively since it saves time and provides excellent quality. Examples of late enhancement for a wide range of patterns (Fig. 6) in both ischemic and non-ischemic heart disease illustrate that PSIR MOCO provides excellent image quality and high spatial resolution to detect small focal enhancement as well as more subtle enhancement.

The typical acquisition of a SAX stack of 9-slices (Fig. 7) is acquired in 9 slices × 8 measurements × 2 RR = 144 heart beats = 2:24 min at 60 bpm. The reconstruction is performed 'on-the-fly' and is completed within 10 seconds of the end of scan. Long axis views may be prescribed individually or as multi-slice. When prescribing long axis views off of free-breathing SAX images, the long axis may be at a different respiratory position and possibly not optimal. Some sites find it simpler to prescribe a parallel stack of 3 long axis slices for each view (Fig. 8) to ensure acquisition of the best position.

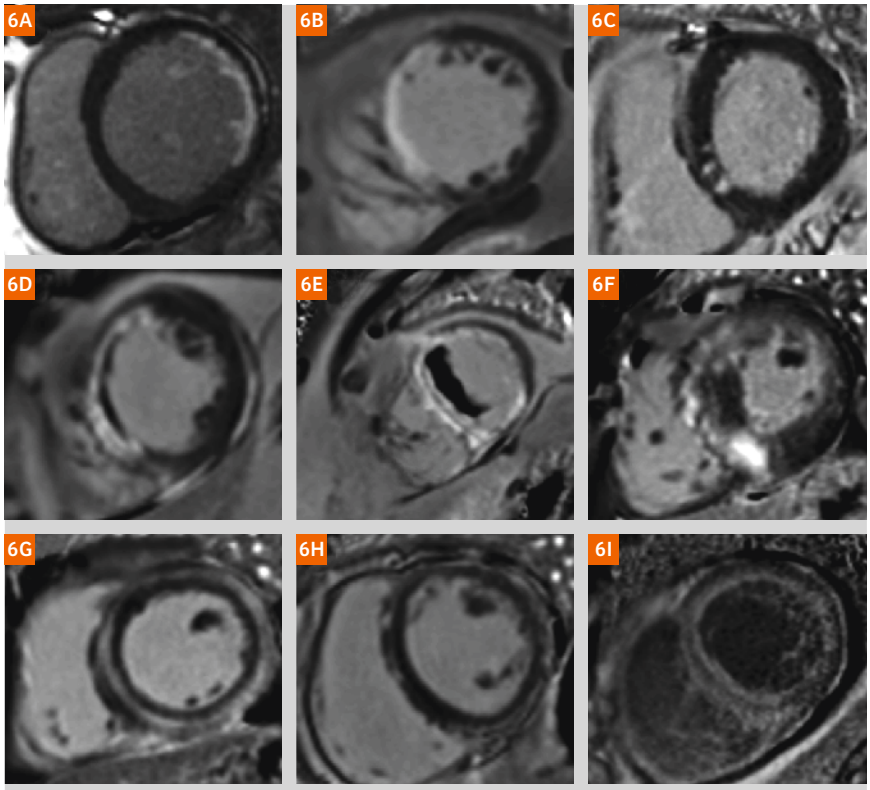

Figure 6: Examples of free-breathing PSIR MOCO LGE images illustrating the a variety of late enhancement patterns: **(6A)** sub-endocardial chronic MI, **(6B)** transmural chronic MI, **(6C)** small focal scar, **(6D)** acute MI with dark core due to microvascular obstruction (MVO), **(6E)** MI with thrombus, **(6F)** heterogeneous focal enhancement in a patient with HCM, **(6G)** mid-wall enhancement in patient with myocarditis, **(6H)** sub-epicardial enhancement in patient with myocarditis, and **(6I)** subendocardial fibrosis in patient with amyloidosis.

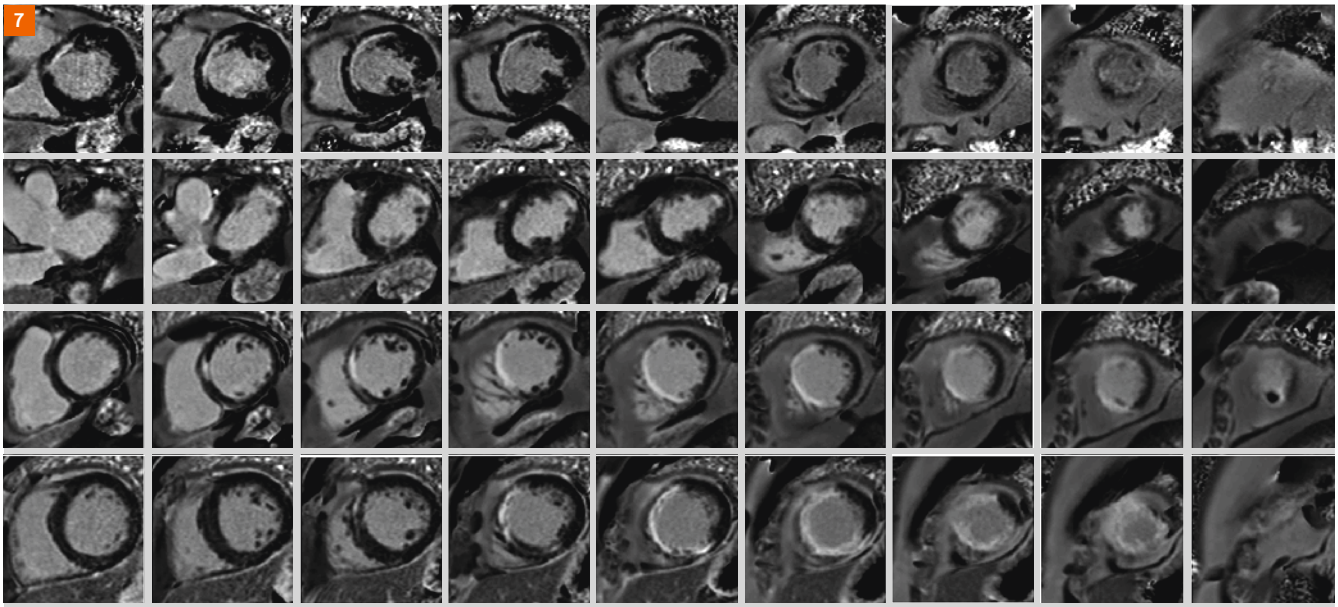

Figure 7: Examples of free-breathing acquisition of stacks of 9 short axis slices using PSIR MOCO LGE acquired and reconstructed on-the-fly in approximately 2.5 min, depending on heart rate.

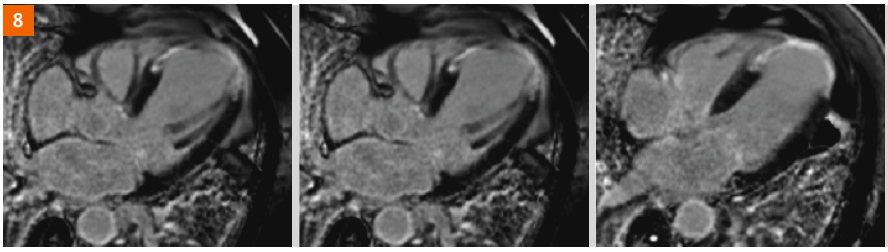

Figure 8: Example of free-breathing acquisition of a stack of 3 parallel long axis slices to ensure that the 4-chamber view is correctly obtained when prescribed off images that are potentially at a different respiratory position.

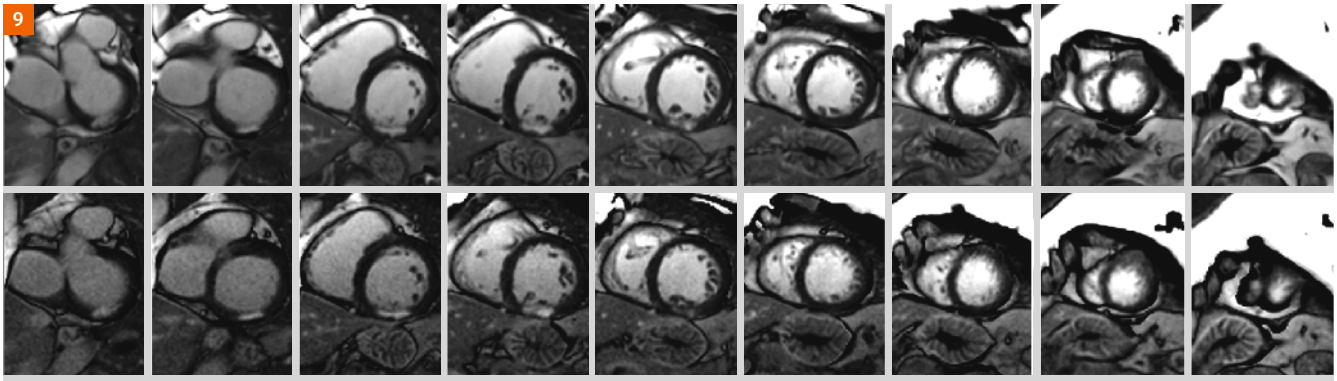

Figure 9: Comparison of 9 slice short axis stack acquired at 3T using the free-breathing PSIR MOCO LGE with SSFP (top) and FLASH (bottom) readouts, respectively.

The PSIR MOCO protocol most frequently used is the SSFP based protocol. A FLASH based protocol has also been tested, and is beneficial in situations with large off-resonance variations that are difficult to shim. There is a reduction in SNR that may be compensated by increased averaging. A comparison of SSFP and FLASH protocols at 3T is shown in Fig. 9 using the same averaging (protocols in Table 1).

Early enhancement imaging

Early gadolinium enhancement (EGE) during the phase between 1–5 minutes following gadolinium administration is often more sensitive to detection of edema, thrombus, or microvascular obstruction (MVO). MVO may be less apparent for LGE when the gadolinium may reach the MI core. Furthermore, in the case of acute MI, the early enhancement may show the area at risk since the edematous tissue will experience a more rapid early enhancement than the central core. Similarly the edematous region in acute myocarditis is more conspicuous in early phase.

The free-breathing PSIR MOCO LGE protocol may be used for EGE without tiring the patient. The EGE may use the same LGE protocol, or may use a reduced number of averages, e.g. 4, in order that a full SAX stack can be acquired in just over minute, in cases where better time resolution is desired.

Dark Blood PSIR LGE

Late-enhancement imaging typically achieves excellent contrast between infarcted and normal myocardium. However, the contrast between the MI and the blood pool is frequently suboptimal. A large fraction of infarctions caused by coronary artery disease are sub-endocardial and thus adjacent to the blood pool. The contrast between the blood and MI in the inversion recovery (IR) image depends on variables such as contrast agent dosage, time from gadolinium administration, clearance rate, and imaging parameters. Blood velocity may also have a role in the contrast, even though non-slice-selective IR is used. Therefore, as a result of mechanisms that are not fully characterized or controlled, it is not infrequent that sub-endocardial MIs are difficult to detect or clearly delineate.

A dark blood (DB) LGE may be achieved by combining a T2 preparation [14–16] with IR. In these schemes, the myocardial signal is reduced relative to the blood signal thereby reducing the inversion times to null the myocardium. In this way, it is possible to null both the myocardium and the blood at the same time. The order of the T2 and IR preparations may be applied as T2-IR [16] or IR-T2 [14]. Both of these previously reported schemes used a FLASH readout. We combined an IR-T2 with a single shot SSFP readout and respiratory motion corrected averaging to achieve the acceptable SNR while maintaining the desired spatial and temporal resolution. In this manner, imaging is conducted free-breathing which has benefits for image quality, patient comfort, and clinical workflow. Furthermore, by using a PSIR reconstruction [17] the blood signal may be made darker than the myocardium (i.e. negative signal values) thereby providing contrast between the blood and both the MI and remote myocardium [15].

Dark blood LGE schemes provide contrast between the MI and the blood pool at the expense of SNR. However, the SNR cost of the proposed DB may be recovered by increased averaging. The DB PSIR MOCO LGE protocol in Table 1 achieves comparable contrast-to-noise ratio (CNR) between the MI and myocardium as the conventional bright blood protocol.

Free-breathing, dark blood PSIR LGE imaging has been demonstrated to improve the visualization of subendocardial MI and fibrosis in cases with low contrast with adjacent blood pool (Fig. 10). The proposed method also improves visualization of thin walled fibrous structures such as atrial walls and valves, as well as papillary muscles.

Fat water separated late enhancement

Lipomatous metaplasia is prevalent in chronic myocardial infarction (MI) [18] and other nonischemic cardiomyopathies. Using conventional late enhancement imaging, it is difficult to discriminate between fibrosis and intramyocardial fat since both have low T1 and appear bright. Furthermore, the presence of fat may create image

10

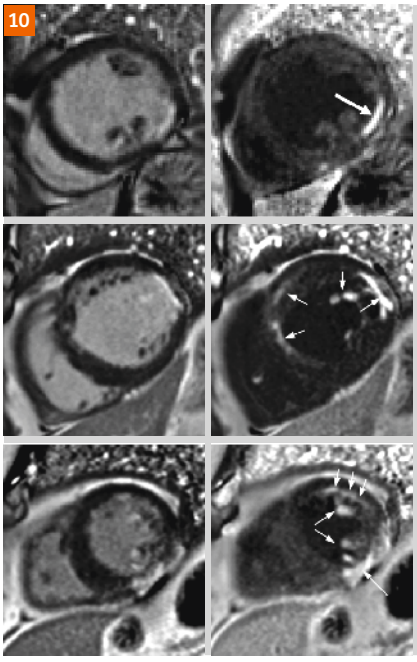

Figure 10: Examples of bright blood (left) and dark blood (DB) (right) PSIR MOCO LGE illustrating improved contrast between subendocardial MI and blood pool. The areas of scar indicated by LGE are more conspicuous on the DB PSIR images (see arrows) and in some cases might have been missed entirely in the bright blood PSIR images.

11

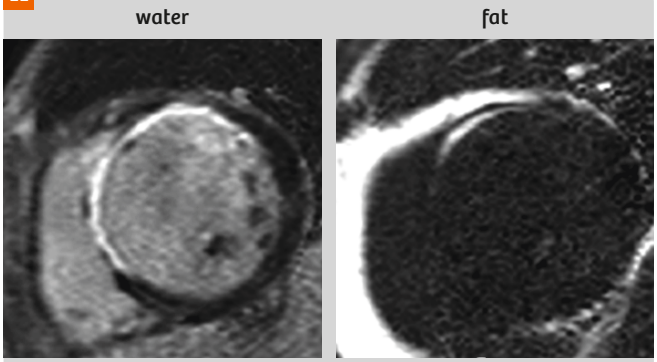

Figure 11: Patient with chronic MI in anteroseptal region with lipomatous metaplasia seen in fat-water separated PSIR MOCO LGE [19].

12

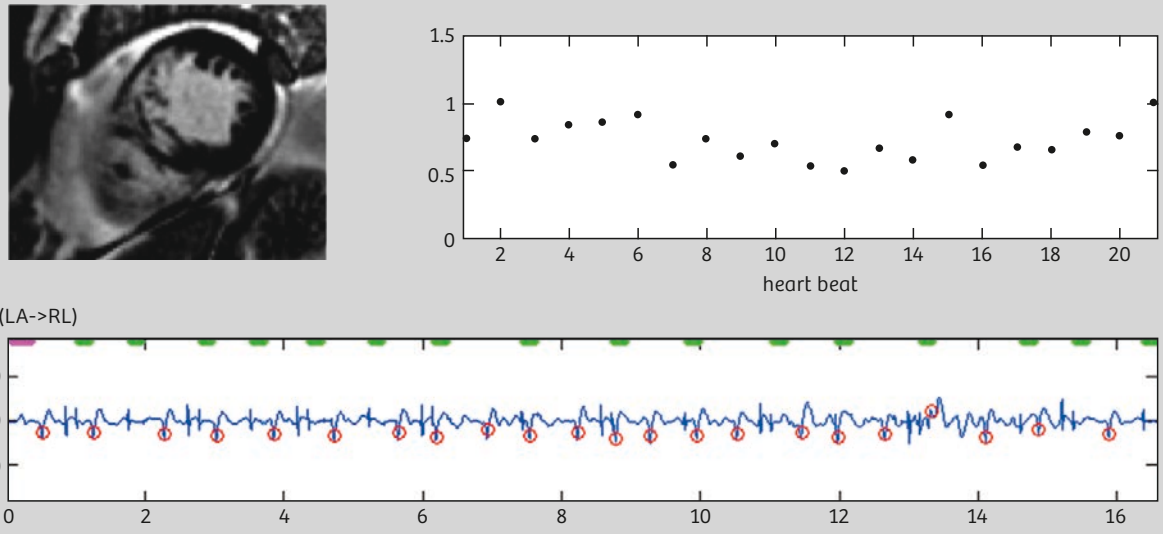

Figure 12: Free-breathing, PSIR MOCO LGE in patient with chronic MI in atrial fibrillation (shown at SCMR 2014 Annual Scientific Meeting, Real-time imaging: in case of atrial fibrillation, Kellman P).

artifacts due to the chemical shift of fat or the bright epicardial fat signal may obscure the sub-epicardium. Using fat-water separated late-enhancement imaging it is possible to distinguish the fibrosis from fat with improved sensitivity and to avoid erroneous tissue classification [19]. Detecting the presence of fibrofatty infiltration or other intramyocardial fat may have diagnostic value. The presence of intramyocardial fat may form a substrate for arrhythmias due to the lower electrical conductivity of fat. It has been shown that fibrofatty infiltration of the myocardium is associated with sudden death, and therefore noninvasive detection could have prognostic value. Fat water separated imaging may be performed free-breathing [20] with multi-echo PSIR MOCO LGE (Table 1). An example of lipomatous metaplasia in chronic MI is shown in Figure 11. It is also used to improve visualization of pericardial disease and in general mass characterization.

Insensitive to arrhythmias

The free-breathing PSIR MOCO LGE imaging based on single shot imaging is inherently insensitive to arrhythmias since it is free from ghosting artifacts experienced with breath-held segmented acquisitions. In patients with arrhythmias during scanning, there may be some variation in the cardiac phase of repeated measurements depending on the precise nature of the variation. It is possible to retrospectively discard heart beats outside of specified criteria, however in practice the MOCO average has been found to be relatively insensitive to a large variation in RR intervals and is even robust in subjects with atrial fibrillation (Fig. 12). Furthermore, some patients experience arrhythmias that are brought on or worsened by breath-holding, and are in sinus rhythm during normal free-breathing.

Discussion

The free-breathing approach to LGE using PSIR MOCO performs reliably with excellent image quality. The image is often better than breath-held LGE in the most vulnerable population that cannot breath-hold [12] and for pediatric subjects[3] [11]. The paradigm shift to free-breathing CMR has benefits to the clinical workflow in terms of speed, ease of use, and patient comfort. A number of other free-breathing protocols that incorporate retrospective MOCO have been recently developed and allow for a complete free-breathing CMR study to include real-time cine function [21, 22], T2-SSFP [23], T2* mapping [24], and myocardial perfusion mapping [25]. These afford a significant reduction in overall exam time when combined. The PSIR MOCO LGE has been adopted at a number of sites as the new standard and is widely used.

Acknowledgements

We would like to acknowledge our colleagues at Siemens, in particular Xiaoming Bi and Randall Kroeker, for their role in development of the PSIR MOCO LGE WIP, and to our numerous clinical collaborators for their insights and clinical examples: Andrew E. Arai, W. Patricia Bandettini, Erik B. Schelbert, James C. Moon, Marianna Fontana, Martin Ugander, Patricia Feuchter, Cavan McGurk, Sofie Olsson, Jenny Rasck, Sarah Anderson, and Christine Mancini.

Supported by the National Heart, Lung and Blood Institute, National Institutes of Health by the Division of Intramural Research.

[3] MR scanning has not been established as safe for imaging fetuses and infants less than two years of age. The responsible physician must evaluate the benefits of the MR examination compared to those of other imaging procedures.

References

1 Fieno DS, Kim RJ, Chen E, Lomasney JW, Klocke FJ, Judd RM. Contrast-Enhanced Magnetic Resonance Imaging of Myocardium at Risk Distinction Between Reversible and. 2000;36:1985–91.
2 Kim RJ, Fieno DS, Parrish TB, Harris K, Chen E-L, Simonetti O, et al. Relationship of MRI Delayed Contrast Enhancement to Irreversible Injury, Infarct Age, and Contractile Function. Circulation. 1999;100:1992–2002.
3 Bohl S, Wassmuth R, Abdel-Aty H, Rudolph A, Messroghli D, Dietz R, et al. Delayed enhancement cardiac magnetic resonance imaging reveals typical patterns of myocardial injury in patients with various forms of non-ischemic heart disease. Int. J. Cardiovasc. Imaging. 2008;24:597–607.
4 Hunold P, Schlosser T, Vogt FM, Eggebrecht H, Schmermund A, Bruder O, et al. Myocardial Late Enhancement in Contrast-Enhanced Cardiac MRI: Distinction Between Infarction and Non-Infarction-Related Disease. AJR. Am. J. Roentgenol. 2005;184:1420–6.
5 Vergara GR, Marrouche NF. Tailored management of atrial fibrillation using a LGE-MRI based model: from the clinic to the electrophysiology laboratory. J. Cardiovasc. Electrophysiol. 2011;22:481–7.
6 Kellman P, Arai AE. Cardiac imaging techniques for physicians: Late enhancement. J. Magn. Reson. Imaging. 2012;36:529–42.
7 Kim RJ, Shah DJ, Judd RM. How We Perform Delayed Enhancement Imaging. J. Cardiovasc. Magn. Reson. 2003;5:505–14.
8 Lee D, Wu E, Chung Y, Simonetti O, Elliot M, Holly T, et al. Comparison Between Single Shot TrueFISP and Segmented TurboFLASH for the Detection of Myocardial Infarction. J. Cardiovasc. Magn. Reson. 2003;5:79–80.
9 Kellman P, Larson AC, Hsu L-Y, Chung Y-C, Simonetti OP, McVeigh ER, et al. Motion-corrected free-breathing delayed enhancement imaging of myocardial infarction. Magn. Reson. Med. 2005;53:194–200.
10 Ledesma-Carbayo MJ, Kellman P, Hsu L-Y, Arai AE, McVeigh ER. Motion corrected free-breathing delayed-enhancement imaging of myocardial infarction using nonrigid registration. J. Magn. Reson. Imaging. 2007;26:184–90.
11 Olivieri L, Cross R, O'Brien KJ, Xue H, Kellman P, Hansen MS. Free-breathing motion-corrected late-gadolinium-enhancement imaging improves image quality in children. Pediatr. Radiol. Pediatric Radiology; 2016;46:983–90.
12 Piehler KM, Wong TC, Puntil KS, Zareba KM, Lin K, Harris DM, et al. Free-Breathing, Motion-Corrected Late Gadolinium Enhancement Is Robust and Extends Risk Stratification to Vulnerable Patients. Circ. Cardiovasc. Imaging. 2013;6:423–32.
13 Hansen MS, Sørensen TS. Gadgetron: an open source framework for medical image reconstruction. Magn. Reson. Med. 2013;69:1768–76.
14 Basha T, Roujol S, Kissinger K V, Goddu B, Manning WJ, Nezafat R. Black blood late gadolinium enhancement using combined T2

magnetization preparation and inversion recovery. J. Cardiovasc. Magn. Reson. BioMed Central Ltd; 2015;17:O14.
15 Kellman P, Xue H, Olivieri LJ, Cross RR, Grant EK, Fontana M, Ugander M, Moon JC, Hansen MS. Dark blood Late Enhancement Imaging. J. Cardiovasc. Magn. Reson. 2016; In press.
16 Liu C-Y, Wieben O, Brittain JH, Reeder SB. Improved delayed enhanced myocardial imaging with T2-Prep inversion recovery magnetization preparation. J. Magn. Reson. Imaging. 2008;28:1280–6.
17 Kellman P, Arai AE, Mcveigh ER, Aletras AH. Phase-Sensitive Inversion Recovery for Detecting Myocardial Infarction Using Gadolinium-Delayed Hyperenhancement. Magn. Reson. Med. 2002;383:372–83.
18 Mordi I, Radjenovic A, Stanton T, Gardner RS, McPhaden A, Carrick D, et al. Prevalence and Prognostic Significance of Lipomatous Metaplasia in Patients With Prior Myocardial Infarction. JACC. Cardiovasc. Imaging. American College of Cardiology Foundation; 2014;1–2.
19 Kellman P, Hernando D, Arai AE. Myocardial Fat Imaging. Curr. Cardiovasc. Imaging Rep. 2010;3:83–91.
20 Kellman P, Hernando D, Shah S, Chefdhotel C, Liang Z-P, Arai A. Free-breathing, single shot fat-water separated cardiac imaging with motion corrected averaging. ISMRM 2010 Sci. Meet. 2010;18:3662.
21 Kellman P, Chefd'hotel C, Lorenz CH, Mancini C, Arai AE, McVeigh ER. Fully automatic, retrospective enhancement of real-time acquired cardiac cine MR images using image-based navigators and respiratory motion-corrected averaging. Magn. Reson. Med. 2008;59:771–8.
22 Xue H, Kellman P, LaRocca G, Arai AE, Hansen MS. High spatial and temporal resolution retrospective cine cardiovascular magnetic resonance from shortened free breathing real-time acquisitions. J. Cardiovasc. Magn. Reson. 2013;15:102.
23 Kellman P, Aletras AH, Mancini C, McVeigh ER, Arai AE. T2-prepared SSFP improves diagnostic confidence in edema imaging in acute myocardial infarction compared to turbo spin echo. Magn. Reson. Med. 2007;57:891–7.
24 Kellman P, Xue H, Spottiswoode BS, Sandino CM, Hansen MS, Abdel-Gadir A, et al. Free-breathing T2* mapping using respiratory motion corrected averaging. J. Cardiovasc. Magn. Reson. 2015;17:3.
25 Xue H, Hansen MS, Nielles-vallespin S, Arai AE, Kellman P. Inline quantitative myocardial perfusion flow mapping. JCMR/ISMRM Workshop. 2016;18:4–6.

Contact

Peter Kellman

National Heart, Lung, and Blood Institute

National Institutes of Health, DHHS

10 Center Drive MSC-1061
Bethesda, MD 20892
USA
kellman@nih.gov

Differential Diagnosis of Claudication: Cystic Adventitial Degeneration of the Popliteal Artery – Diagnosis by a Combination of MR Angiography and Anatomical Sequences

Benjamin Henninger, M.D.

Department of Radiology, Medical University of Innsbruck, Innsbruck, Austria

Case report

A 40-year-old female patient presented at the Department of Vascular Surgery with typical claudication during physical activity after a walking distance of maximum 200 meters. She complained of pain in the right calf that relieved after a short rest. At clinical examination the pulses of the lower extremities were unremarkable at both sides, the oscillogram at rest did not show any pathologies. Under stress the oscillogramm was restricted in the right leg, the treadmill ergometer examination had to be stopped at 3 km/h and 12% fall after 80 meters. The preliminary diagnosis was peripheral artery disease (PAD) grade IIB, a conservative therapy was initially suggested.

The patient was then transferred to our Department of Radiology for the evaluation of PAD. We performed multi-station bolus-chase magnetic resonance angiography (MRA) in the arterial phase of the pelvis and the whole lower extremity (3T, MAGNETOM Skyra, Siemens Healthcare, Erlangen, Germany) in 4 steps using a dedicated peripheral vascular coil together with the body-array and spine-array coils and a fast 3D spoiled gradient echo sequence (T1 3D FLASH) in coronal orientation (TR 3.75 ms, TE 1.33 ms, flip angle: 24°, parallel imaging factor: 3, base resolution: 384, number of slices per slab: 72–80, slice thickness: 1.3 mm, FOV: 420) [1]. A bi-phasic continuous injection of the contrast agent (CA) was used (1 ml/sec and 0.6 ml/sec) together with an automatic movement of the table (table advance per stage: 260–300 mm). Planning of the procedure was done by utilizing the Tim Planning Suite with a Set-n-Go protocol. For the timing of the CA the care bolus technique was applied. The MRA showed an occlusion of the popliteal artery in the P1/P2 segment over a distance of 5 cm with mild collateralization (Fig. 1). All the other vessels were

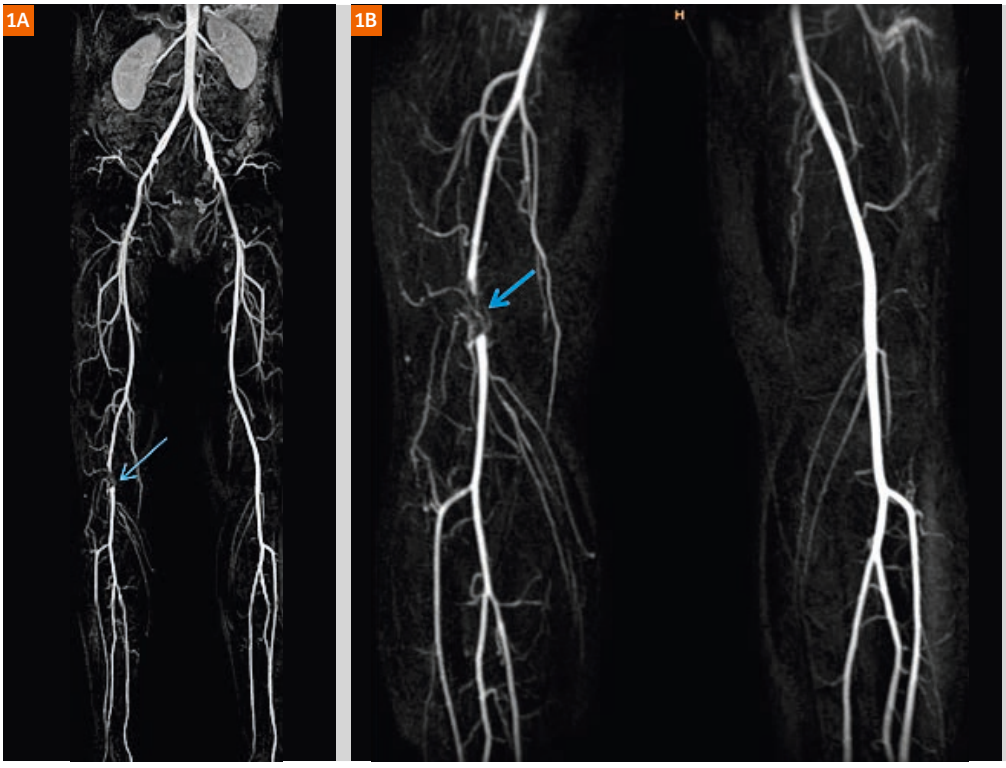

Figure 1: MR-angiography (3T, MAGNETOM Skyra) clearly depicting an occlusion of the popliteal artery in the P1/P2 segment over a distance of 5 cm with mild collateralization (blue arrows).

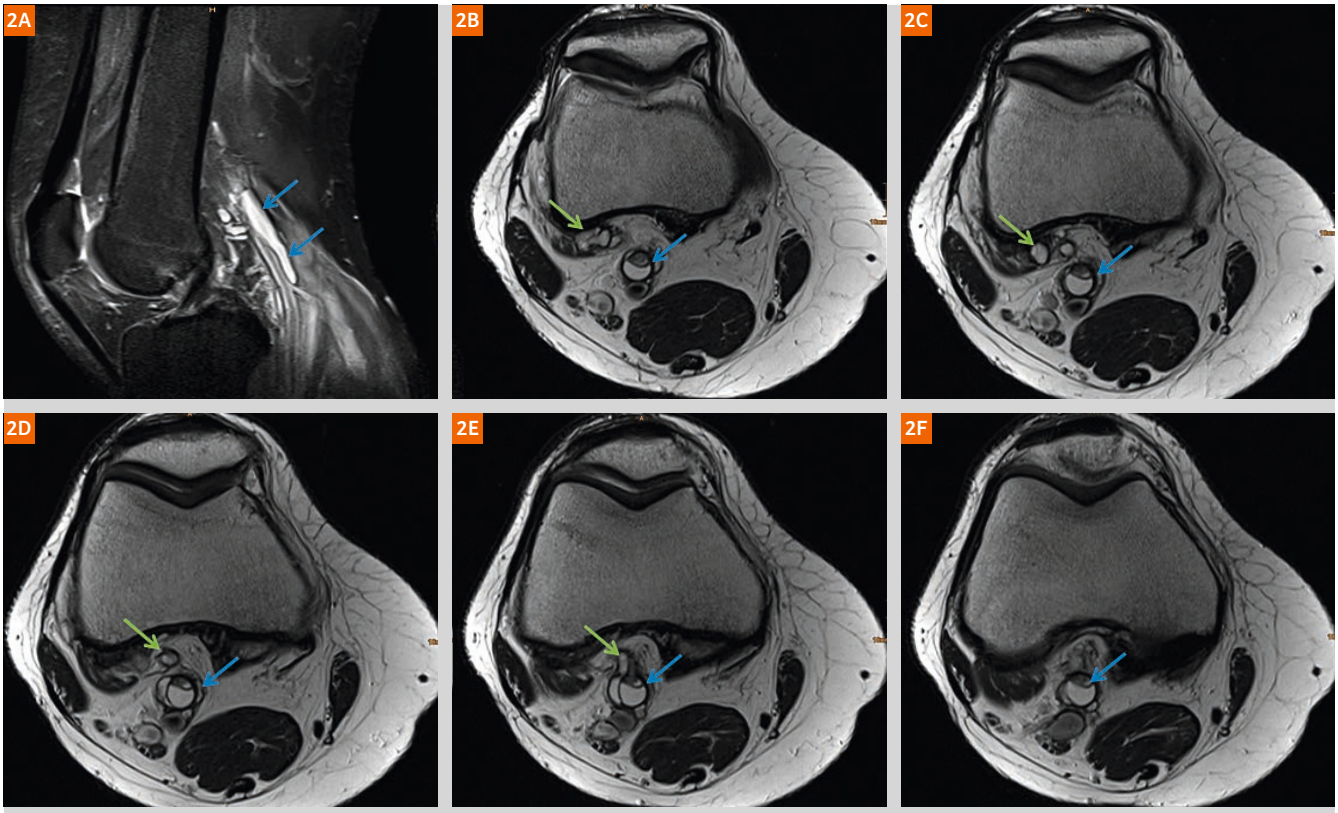

Figure 2: MRI of the knee (1.5T, MAGNETOM Avanto) demonstrating a cystic lesion that is adherent to the popliteal artery (blue arrow). Further we could demonstrate a connection to a ganglion that is adjacent to the knee joint (green arrow). Image **2A** is a sagittal TIRM (TE 15 ms, TR 3160 ms, SL 3 mm, matrix 316 x 320) and images **2C–F** are axial T2-weigthed turbo-spin-echo sequences (TE 79 ms, TR 4680 ms, SL 3 mm, matrix 384 x 384).

unremarkable which is unlikely for a vasosclerotic disease with only one focal manifestation in a young woman. Therefore we decided for a further evaluation by MRI of the knee to rule out other differential diagnosis for the occlusion. We performed knee MRI on a 1.5T scanner (MAGNETOM Avanto, Siemens Healthcare, Erlangen, Germany) with a dedicated knee coil (8-ch high-resolution knee array, Invivo, Gainesville, FL, USA). The protocol consisted of a sagittal TIRM sequence (TE 15 ms, TR 3160 ms, SL 3 mm, matrix 316 x 320) and an axial T2-weigthed turbo-spin-echo sequence (TE 79 ms, TR 4680 ms, SL 3 mm, matrix 384 x 384). We found a cystic lesion (hyperintense on TIRM and T2), adherent to the popliteal artery, with an extraluminal appearance (Fig. 2). The diagnosis was cystic adventitial degeneration of the popliteal artery causing a compression of the artery leading to a stenosis.

The patient was again referred to the Department of Vascular Surgery and due to the clinical burden a surgical procedure was performed. The affected part of the popliteal artery was resected and replaced with the vena basilica by an end to end anastomosis. Postoperative MRA showed a regular opacification of the interponate (Fig. 3). The clinical symptoms disappeared after the intervention and the patient at present is free of any symptoms.

Discussion

The cystic adventitial degeneration is a challenging diagnosis. The disease was initially described by Atkins in 1947 [2]. It is a vascular condition characterized by a collection of mucinous material within the adventitia that constricts the vessel from the outside [3–5]. The P2 segment of the popliteal artery is the most common localization. Patients typically present with the same symptoms as patients with classical PAD. The disease predominantly occurs in young males (age < 50 years) presenting with typical symptoms of claudication. The lack of risk factors for arteriosclerosis and the atypical age should alert for other differential diagnosis. Beside cystic adventitial degeneration other differential diagnosis such as chronic exertional compartment or popliteal entrapment syndrome, chronic venous insufficiency, degenerative disk disease, osteoarthritis, spinal stenosis and thrombangiitis obliterans should also be considered [6].

In some cases MRA can be negative and therefore misleading because the cyst of the adventitia leads to a dynamic exercise-dependent flow inhibition. In our case the occlusion could be clearly depicted with MRI and further associated to a cystic lesion by a local MRI of the knee.

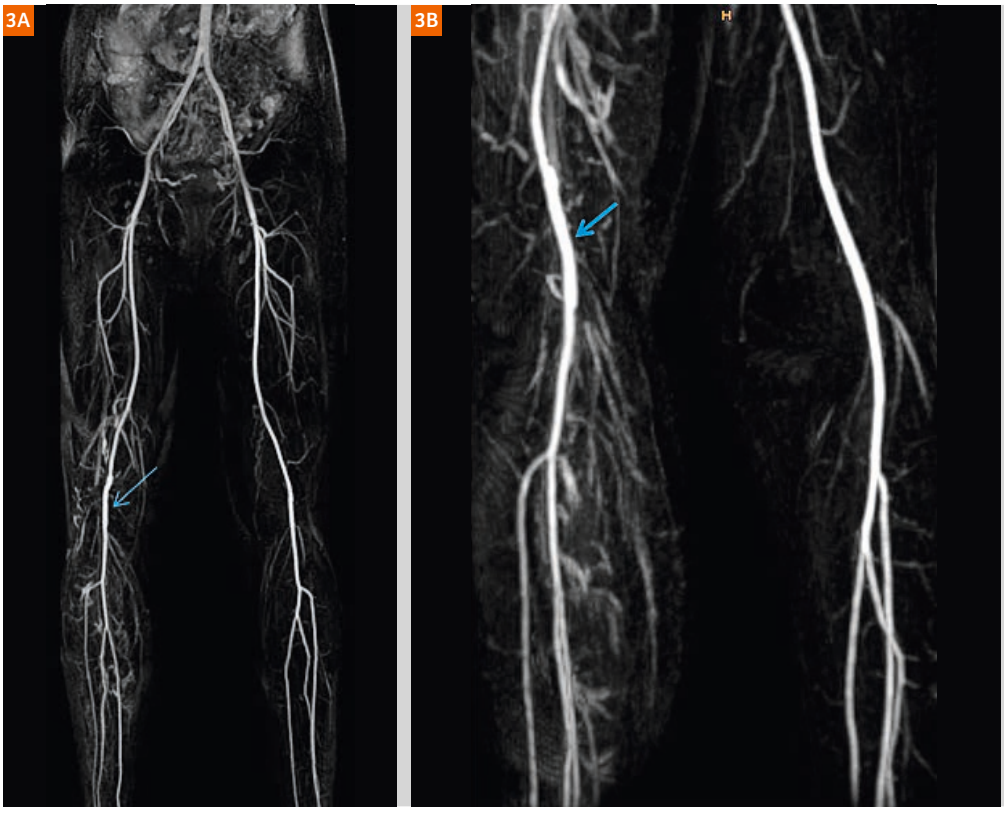

Figure 3: MR-angiography (3T, MAGNETOM Skyra) after resection of the affected popliteal artery and replacement with the vena basilica by an end-to-end anastomosis. Regular opacification of the interponate is shown (blue arrows).

The pathogenesis of cystic adventitial degeneration is still unexplained, but several theories have been advanced:

1. The synovial theory: adventitial cysts are seen as ganglia originating from the adjacent joint space [7];
2. The embryologic theory: inclusion of mucin-secreting cells in the wall of the vessel [8];
3. Microtrauma theory: repeated injuries lead to a progressive degeneration of the arterial adventitia [9, 10].

Our case supports theory 1 because we found a connection between the cyst and ganglia that was adjacent to the knee joint space (Fig. 2).

MRI with a combination of MRA and anatomical sequences are essential tools in the clarification of differential diagnosis in PDA. Further MRI is crucial for surgical planning and also for postoperative control.

References

1 Nielsen YW, Thomsen HS. Contrast-enhanced peripheral MRA: technique and contrast agents. Acta Radiol. 2012;53(7):769-77.
2 Atkins HJ, Key JA. A case of myxomatous tumour arising in the adventitia of the left external iliac artery; case report. Br J Surg. 1947;34(136):426.
3 Rich NM. Popliteal entrapment and adventitial cystic disease. The Surgical clinics of North America. 1982;62(3):449-65.
4 Korngold EC, Jaff MR. Unusual causes of intermittent claudication: popliteal artery entrapment syndrome, cystic adventitial disease, fibromuscular dysplasia, and endofibrosis. Current treatment options in cardiovascular medicine. 2009;11(2):156-66.
5 Kiskinis D, Raithel D. Uncommon causes of intermittent claudication: cystic adventitial disease of the popliteal artery and popliteal artery entrapment syndrome. Cardiovascular Research Center bulletin. 1979;17(4):69-74.
6 Sontheimer DL. Peripheral vascular disease: diagnosis and treatment. American family physician. 2006;73(11):1971-6.
7 Malghem J, Vande berg BC, Lebon C, Lecouvet FE, Maldague BE. Ganglion cysts of the knee: articular communication revealed by delayed radiography and CT after arthrography. AJR Am J Roentgenol. 1998;170(6):1579-83.
8 Levien LJ, Benn CA. Adventitial cystic disease: a unifying hypothesis. Journal of vascular surgery. 1998;28(2):193-205.
9 Chapman T, Pinkerton JA. Cystic adventitial disease of the popliteal artery. Southern medical journal. 1984;77(3):370-2.
10 Lassonde J, Laurendeau F. Cystic adventitial disease of the popliteal artery. Clinical aspects and etiology. The American surgeon. 1982;48(7):341-3.

Contact

PD Dr. Benjamin Henninger, M.D.
Department of Radiology
Medical University of Innsbruck
Anichstraße 35
6020 Innsbruck
Austria
benjamin.henninger@i-med.ac.at

Coronary PET/MR of Micro-Calcification in Atherosclerosis

Philip M. Robson, Ph.D.[1]; Marc R. Dweck, M.D.[2]; Maria Giovanna Trivieri, M.D.[3]; Ronan Abgral, Ph.D.[4]; Nicolas A. Karakatsanis, Ph.D.[1]; Zahi A. Fayad, Ph.D.[1,3]

[1] Translational and Molecular Imaging Institute, Icahn School of Medicine at Mount Sinai, New York, NY, USA
[2] British Heart Foundation Centre for Cardiovascular Science, University of Edinburgh, Edinburgh, UK
[3] Cardiovascular Institute, Icahn School of Medicine at Mount Sinai, New York, NY, USA
[4] Department of Nuclear Medicine, University Hospital of Brest, European University of Brittany, Brest, France

Introduction

Positron Emission Tomography (PET) is an established non-invasive imaging technology that allows the activity of specific disease processes to be measured. PET imaging using the radiotracer ^{18}F-fludeoxyglucose (^{18}F-FDG)[1] has been used previously in the study of vascular inflammation in atherosclerotic plaque [1, 2]. FDG, a sugar analogue, is taken up more avidly by activated macrophages in the plaque compared to surrounding tissue. Consequently, increased ^{18}F-FDG PET signal is a biomarker for active disease. Recently, ^{18}F-sodium fluoride (^{18}F-NaF), a PET tracer used in bone imaging that preferentially binds to areas of micro-calcification, has emerged as a marker of vascular micro-calcification activity in both aortic stenosis and atherosclerosis [3–5]. Whilst coronary calcium scoring using Computed Tomography (CT) measures macro-calcification and is well-established as a prognostic marker of coronary artery disease, the earlier stage of active micro-calcification is potentially a valuable marker of disease activity and of use for identifying patients with increased atherosclerotic burden and increased risk who may benefit from more aggressive risk factor modification.

[1] The full prescribing information for the Fludeoxyglucose F18 injection can be found at page 37.

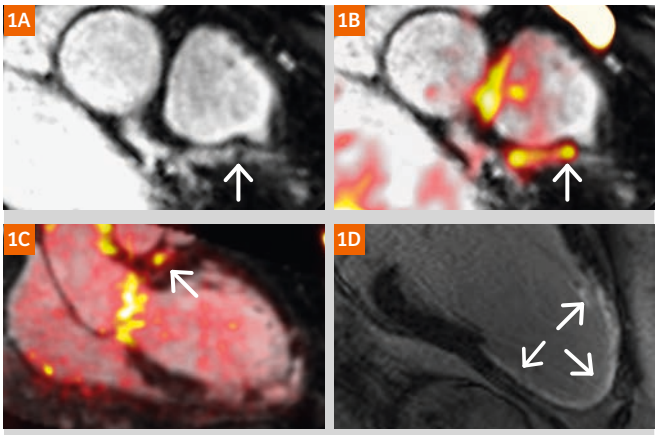

Figure 1: In a patient who had recently suffered a myocardial infarction, the culprit plaque is seen to cause aluminal stenosis in the left anterior descending artery seen on MR-angiography **(1A).** Elevated ^{18}F-NaF activity in the culprit plaque is identified by MR/PET and overlays the luminal stenosis seen on fused MR/PET-angiography **(1B),** and in a long axis view of the left ventricle **(1C).** Note uptake also in the wall of the aortic arch and the aortic valve. Extensive scarring is observed in late gadolinium enhanced MR in the territory of the lesion **(1D).**

Traditionally, cardiovascular PET imaging is performed using CT for anatomical and attenuation measurements. However, PET/CT imaging is limited by the additional radiation dose of CT, especially in chronic conditions such as atherosclerosis where serial imaging would be desirable. Moreover, vascular PET/CT imaging has predominantly focused on the aorta, carotid and peripheral arteries. Imaging of the coronary arteries, despite their great importance, is challenging owing to their small caliber and complex respiratory and cardiac motion. Although cardiac gating may be used in PET/CT to mitigate motion effects, data may invariably be lost. MR imaging on the other hand is well-suited for radiation-free imaging of cardiac motion required to correct PET data. The advent of hybrid systems combining PET cameras and Magnetic Resonance (MR) scanners is consequently of considerable interest for vascular imaging in atherosclerosis.

Coronary ^{18}F-NaF MR/PET imaging in a patient post myocardial infarction

A patient (64-year-old male) with unstable coronary artery disease who was 6 months post myocardial infarction for which he did not undergo revascularization underwent PET/MR imaging on the Biograph mMR system. He was injected with 5 MBq/kg ^{18}F-NaF 30 minutes prior to PET imaging. PET data was acquired for 60 minutes. PET image reconstruction employed an iterative ordinary poisson ordered-subsets expectation-maximization algorithm with 21 subsets and 6 iterations incorporating point-spread-function resolution modeling [6], a 344 x 344 x 127 matrix and a 2 mm full-width-at-half-maximum Gaussian post-reconstruction filter. Attenuation correction included the body transmission coil and 6 channels of the 16-ch spine array mounted in the table, but omitted the 6-channel chest array used for cardiac imaging. Attenuation for the body was measured using a 6–7 minutes free-breathing golden-angle radial VIBE sequence[2] to provide motion-averaged anatomical representation of the anatomy to match the PET data. Acquisition parameters included 500 x 500 mm^2

coronal field-of-view, 72–88 slices covering the whole body with partial-Fourier Cartesian slice-encoding, 3 mm isotropic resolution, TR/TE 4.5/2.45 ms, in-phase TE, 9° flip angle, 1600 radial views. Images were segmented into background and soft tissue before being converted to μ-maps and incorporated into offline PET reconstruction software (e7-tools[2], Siemens Healthcare). Free-breathing MR-attenuation correction is used to eliminate artifacts that can appear in the PET images due to mismatch of PET emission and attenuation data. Additional MR data acquired simultaneously included anatomical axial HASTE, short- and long-axis TrueFISP cine imaging, 3D whole-heart contrast-enhanced coronary MR angiography [7] and short-axis late gadolinium enhanced imaging.

Increased ^{18}F-NaF uptake was identified in the culprit plaque in the left anterior descending coronary artery. The plaque could be seen on the MR-angiography causing a proximal luminal stenosis that coincided with the hotspot on fused PET/MR images (Fig. 1). An extensive near-transmural myocardial infarction was observed on late gadolinium enhanced MR images, corresponding to the perfusion territory of this lesion.

The future of coronary PET/MR imaging

The preliminary work presented in this article has demonstrated the feasibility of coronary PET/MR imaging by successfully identifying active coronary disease in a patient post myocardial infarction. Additional technical development will improve the robustness and quantitative accuracy of attenuation correction methods for PET/MR.

Despite the superior coronary angiography and depiction of macro-coronary-calcification available with CT, combined PET/MR imaging is capable of excellent coronary angiography [8] and the potential for sensitive detection of macro-calcification [9] as well as having additional potential benefits. MR imaging provides a wealth of complementary information on plaque characteristics such as hemorrhage [9], vessel wall remodeling [10], and vessel wall permeability [11], as well as traditional cardiac MR measurements of morphology, function and scarring in a single scan. In addition, radiation-free MR imaging with its high spatial and temporal resolution has the potential to provide motion estimates that can be used to correct for the complex motion that affects coronary PET data, and will likely surpass cardiac gating that can be employed for PET/CT imaging.The continued development of ^{18}F-NaF as a tracer of atherosclerotic disease activity will be exciting. Studies are underway to examine whether coronary ^{18}F-NaF PET/CT provides prospective prediction of myocardial infarction in the PREFFIR trial (ClinicalTrial.gov NCT02278211). With increased interest in coronary PET/MR, the advent of new tracers targeting other aspects of the complex biology of atherosclerosis and thrombosis is an exciting possibility. Finally, the reduced radiation dose compared to PET/CT paves the way to investigate serial imaging of atherosclerotic disease activity in both clinical and research arenas.

References

1 Rudd JHF., Warburton EA., Fryer TD., et al. Imaging atherosclerotic plaque inflammation with [18F]-fluorodeoxyglucose positron emission tomography. Circulation 2002;105(23): 2708–11.

2 Rogers IS., Nasir K., Figueroa AL., et al. Feasibility of FDG imaging of the coronary arteries: comparison between acute coronary syndrome and stable angina. JACC Cardiovasc Imaging 2010;3(4):388–97. Doi: 10.1016/j.jcmg.2010.01.004.

3 Dweck MR., Chow MWL., Joshi NV., et al. Coronary arterial 18F-sodium fluoride uptake: a novel marker of plaque biology. J Am Coll Cardiol 2012;59(17):1539–48. Doi: 10.1016/j.jacc.2011.12.037.

4 Irkle A., Vesey AT., Lewis DY., et al. Identifying active vascular microcalcification by (18) F-sodium fluoride positron emission tomography. Nat Commun 2015;6:7495. Doi: 10.1038/ncomms8495.

5 Joshi NV., Vesey AT., Williams MC., et al. 18F-fluoride positron emission tomography for identification of ruptured and high-risk coronary atherosclerotic plaques: a prospective clinical trial. Lancet Lond Engl 2014;383(9918):705–13. Doi: 10.1016/S0140-6736(13)61754-7.

6 Aklan B., Oehmigen M., Beiderwellen K., et al. Impact of Point-Spread Function Modeling on PET Image Quality in Integrated PET/MR Hybrid Imaging. J Nucl Med Off Publ Soc Nucl Med 2016;57(1):78–84. Doi: 10.2967/jnumed.115.154757.

7 Liu X., Bi X., Huang J., Jerecic R., Carr J., Li D. Contrast-enhanced whole-heart coronary magnetic resonance angiography at 3.0 T: comparison with steady-state free precession technique at 1.5 T. Invest Radiol 2008;43(9): 663–8. Doi: 10.1097/RLI.0b013e31817ed1ff.

8 Dweck MR., Puntman V., Vesey AT., Fayad ZA., Nagel E. MR Imaging of Coronary Arteries and Plaques. JACC Cardiovasc Imaging 2016;9(3): 306–16. Doi: 10.1016/j.jcmg.2015.12.003.

9 Fan Z., Yu W., Xie Y., et al. Multi-contrast atherosclerosis characterization (MATCH) of carotid plaque with a single 5-min scan: technical development and clinical feasibility. J Cardiovasc Magn Reson Off J Soc Cardiovasc Magn Reson 2014;16:53. Doi: 10.1186/s12968-014-0053-5.

10 He Y., Zhang Z., Dai Q., et al. Accuracy of MRI to identify the coronary artery plaque: a comparative study with intravascular ultrasound. J Magn Reson Imaging JMRI 2012;35(1): 72–8. Doi: 10.1002/jmri.22652.

11 Maintz D., Ozgun M., Hoffmeier A., et al. Selective coronary artery plaque visualization and differentiation by contrast-enhanced inversion prepared MRI. Eur Heart J 2006;27(14):1732–6. Doi: 10.1093/eurheartj/ehl102.

[2] WIP, the product is currently under development and is not for sale in the US and in other countries. Its future availability cannot be ensured.

Contact

Zahi A. Fayad, Ph.D, FAHA, FACC, FISMRM

Icahn School of Medicine at Mount Sinai

Mount Sinai Endowed Chair in Medical Imaging and Bioengineering

Professor of Radiology and Medicine (Cardiology)

Director, Translational and Molecular Imaging Institute

Director, Cardiovascular Imaging Research

Vice-Chair for Research, Department of Radiology

One Gustave L. Levy Place
Box 1234
New York, NY 10029-6574
USA
Phone: +1 212 824 8452
Fax: +1 240 368 8096
zahi.fayad@mssm.edu

Imaging Proximal Coronary Arteries / Coronary Root Imaging

Jonathan Richer

Clinical Applications Specialist MRI, Siemens Healthineers, Wayville, SA, Australia

Introduction

Cardiac imaging can be a challenging examination and imaging coronary arteries can be slightly more complex still. There are quite a few protocols available for imaging of these small arteries within the Siemens library, such as a breath-hold slab, or using dual gating (respiratory and ECG gating) covering the entire heart or on a targeted approach 3D. Both methods can achieve excellent results. However, they are very patient-dependent, can be time consuming and, in the case of the breath-hold 3D, results are variable due to the very long breath-hold times.

To answer the clinical questions with MRI, the majority of clinicians will typically only need to consider imaging the coronary root in cases of anomalous vessels, and rarely do we need to image the entire vasculature.

Technique

I have modified a 2D TrueFISP sequence in order to image the proximal coronary arteries with a segmented bright blood approach imaging quickly and within a few breath-holds. This can be adapted for both 1.5 and 3T, and protocol parameters are very similar.

You can start by using the TrueFISP sequence in the Siemens library.

1

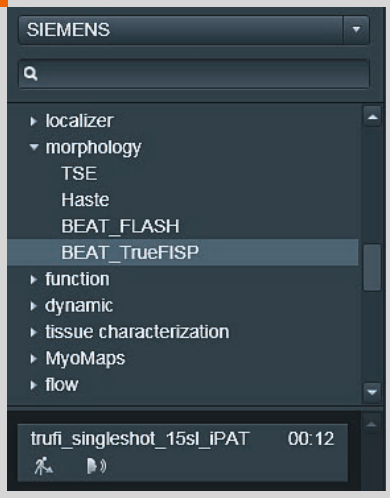

Figure 1: Heart → Morphology → BEAT_TrueFISP → **"trufi_singleshot_15sl_iPAT"**

To achieve a nice thin slice thickness in order to minimize partial voluming effects, we need to image at a minimum slice thickness of 3 mm which this sequence won't allow you to do unless we change the RF excitation pulse type from Fast → to Normal. This will disable the VERSE pulse mode and enables standard RF wave form for a better slice excitation profile, thus allowing for a thinner imaging slice.

2

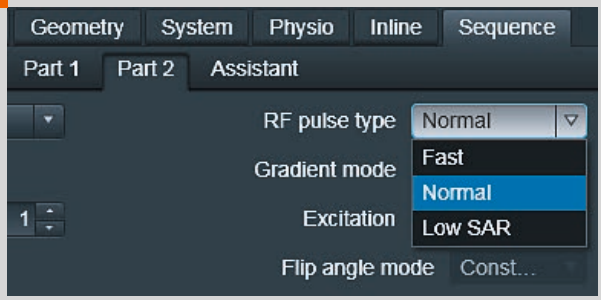

Figure 2: Sequence → Part 2 → RF Pulse type → **"Normal"**

Whilst a 3 mm slice thickness is great, we want to eliminate the slice gap, and what this sequence will allow us to do is to set a slice overlap which again helps with minimizing slice partial voluming. This can be set to **-50%** of the slice thickness where we end up with a slice thickness of 3 mm with a 1.5 mm overlap – achieving the similar results to truly acquiring the data at 1.5 mm slice thickness which is outside the possibility of this sequence. We will also need to increase the slice coverage from 25 slices to 30 or 35 slices – ensuring the coronary sinus is covered.

3

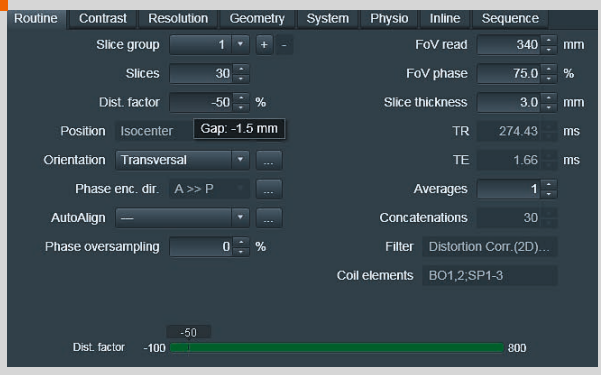

Figure 3: Eliminate the slice gap.

Another important parameter to look at is the echo spacing and ideally we must keep this below 3.4 msec. This is particularly important at 3T where an echo spacing of 3.4 or

lower will result in less dephasing artifacts. Changing the asymmetric echo from Weak → to Strong and increasing the bandwidth will enable you to reach this target echo spacing.

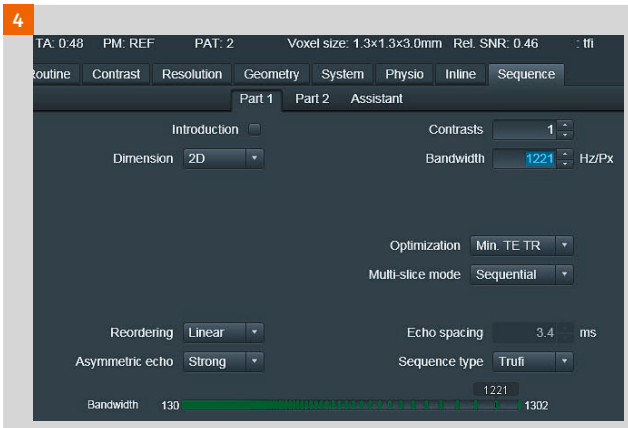

Figure 4: Sequence → Part 1 → Asymmetric echo → **"Strong"**

The next step is to ensure appropriate triggering in order to achieving motion-free images. This is done by segmentation where we need to segment/limit *k*-space data acquisitions to appropriate intervals within the cardiac cycle.

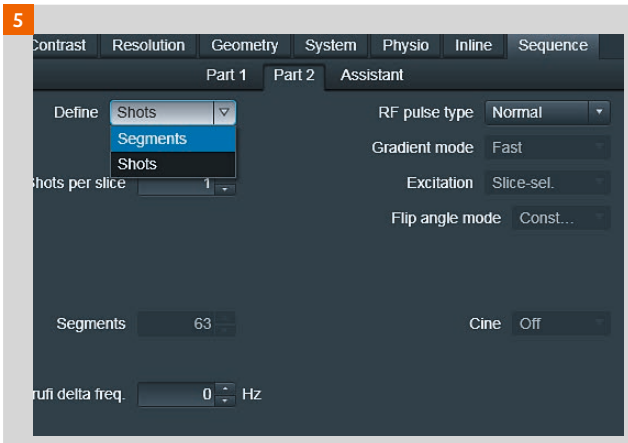

Figure 5: Sequence → Part 2 → Define → **"Segments"**

Now we need to increase the segments lines (*k*-space lines acquired in each heart beat) to roughly 30 which gives us a data readout of roughly 100 ms – suitable for most heart rates. To ensure optimal image quality, we must acquire data within the cardiac cycle when the coronary arteries are stationary. This can be done easily with the timing method – by looking at the trigger time on a 4-chamber cine image Trigger Time (TT stamp). Typically the most stable part of the cardiac cycle is in the diastolic phase; however, in fast heart rates, this may be in the systolic phase. Carefully page through the cine images, keep an eye on the right coronary sinus and take note of the trigger time when the heart stops moving in the diastolic phase and when it starts to move again at the end of the cardiac cycle – this will give us the window of opportunity to acquire data.

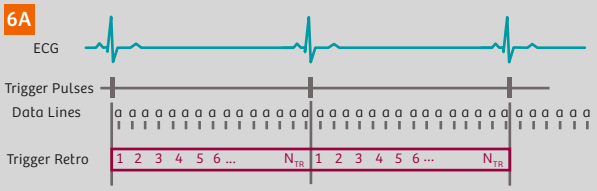

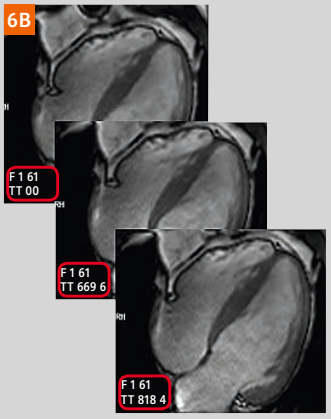

Figure 6A: Trigger Time corresponds to the time within the averaged heart beat in msec.

Figure 6B: Example: Heart stops moving in diastolic phase at "TT**669**" and starts moving again at "TT**818**" (818 - 669 = **149** msec **window**) thus we must **start acquiring after 669** msec and **finish by 818** msec.

Tip: If the heart rate has changed from the start of the examination to the point where we need to do this timing method, the timing will not reflect the patient's current heart rate and therefore you will need to re-run your 4-chamber cine view for accurate results.

Figure 7: Hovering on the Trigger delay will display detailed acquisition information: **Data window duration:** how long we acquire data for (data readout) adjusted by segments (increase segments increase window duration and vis versa) **Data window start:** time we start acquiring data which is manipulated by adjusting the Trigger Delay value. Adding the **Data window start** & **Data window duration** gives us the time we finish acquiring.

In the example above (Figs. 6A, B), we need to start acquiring after 669 msec and finish by 818 msec, and here (Fig. 7) we start at 695 msec and finish at 797 msec (102 + 695 = 797) which is excellent. If we need to start later or earlier, this is done by modifying the Trigger delay. In the case where the heart is not stationary for 102 msec (fast heart rates), we need to decrease the segments (*k*-space lines acquired in each heart beat) to reduce the Data window duration (data readout) fitting for the HR.

Now that we've taken care of the triggering and imaging slab, we must ensure we can acquire data within appropriate breath-hold times. This is done by applying breath-hold option under the Physio and PACE card which will then enable you to modify the concatenations (breath-holds). Once you have updated the concatenations, hover over the acquisition time "TA" to see the actual breath-hold times for each concatenation if appropriate for your patient.

8

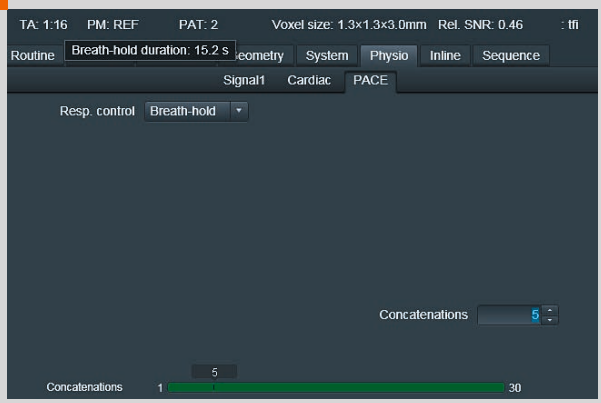

Figure 8: Physio → PACE → Resp. Control → **Breath-hold** Physio → PACE → Concatenations → **5**

Parameter name	Value	Parameter change
Slice thickness	3 mm	RF Pulse Type: Normal
Slice gap	-50%	Routine Tab
Segments	30 or appropriate for HR	Sequence Part 2 → define by segments
Breath-hold timing	15 seconds or appropriate	PACE → Breath-hold → Concatenations → 5
Echo spacing	3.4 or less	Sequence → Part 1 → asymmetric echo → Strong & possible BW increase
Flip angle	80–90 (the higher the brighter the blood)	Contrast → Flip angle

Table 1: Imaging parameters.

Contact

Jonathan Richer

Siemens Healthcare Pty. Ltd.
HC APC AUS SV-CS APP DI

27 Greenhill Road
5034 Wayville SA
Australia
Phone: +61 1800 310 300
Mobile: +61 409 723 125
jonathan.richer@siemens.com

Results

This modified sequence will enable you to image the coronary root with a standard 2D bright blood approach within a few breath-holds tailored for your patient's breath-hold capability and heart rate which is generally acquired faster and with higher success rates when compared to the 3D options. Since we are imaging at 3 mm with a 1.5 mm slice overlap, this data will also enable you to create some modified multiplanar reconstructions (MPR) for better visualization in the 3D card. Figures 9 and 10 are some recent examples.

9

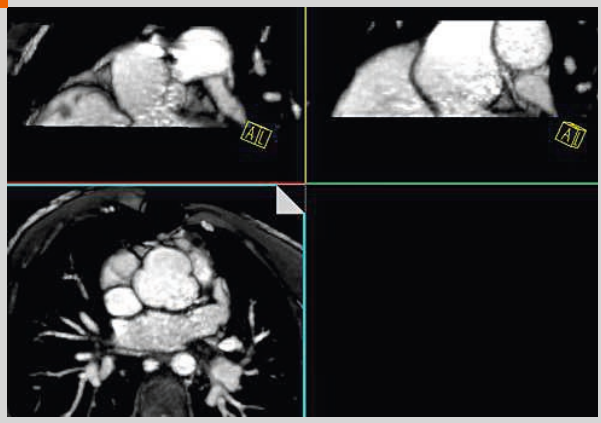

Figure 9: 7-year-old patient. *(1.5T MAGNETOM Aera. Courtesy of Lady Cilento Children's Hospital, Brisbane, Queensland, Australia)*

10

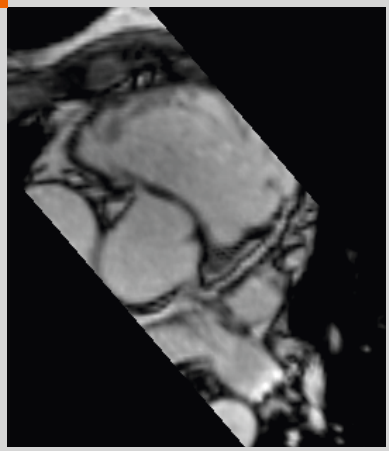

Figure 10: 34-year-old patient. *(3T MAGNETOM Prisma. Courtesy of Hunter Medical Research Institute, Newcastle, NSW, Australia)*

Conclusion

This technique is a great way to image the proximal coronary arteries using conventional imaging technique standard on any MAGNETOM system. However this technique does have its limitations shared by all normal cardiac imaging, such as consistent heart rates and reproducible breath-holds.

Compressed Sensing Cardiac Cine[1]
Beyond speed. Beyond breath-holds.

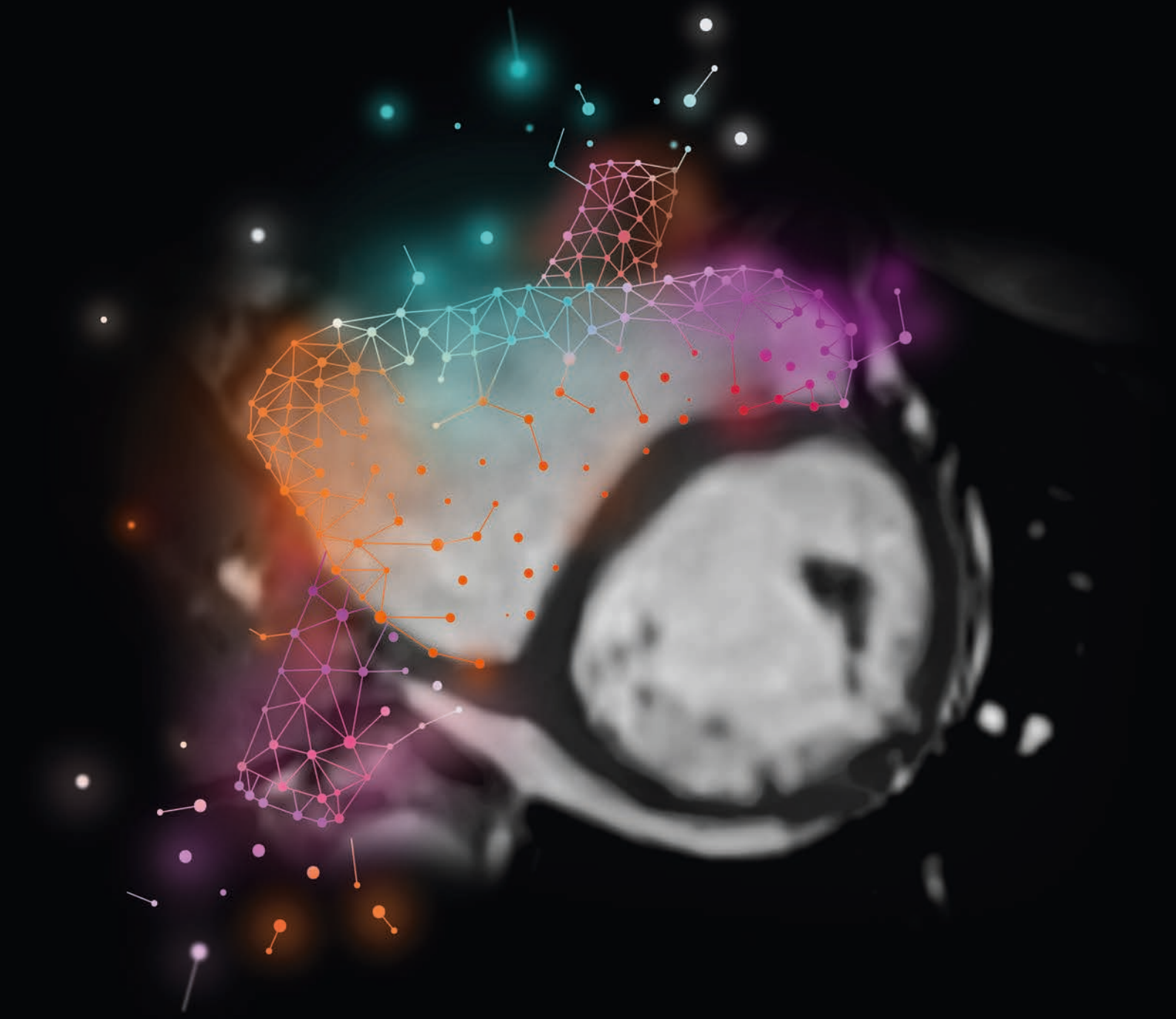

Acquire free-breathing, high-resolution Cardiac Cine images.

Capture the whole cardiac cycle for precise quantification.

Expand patient population eligible for cardiac MRI.

---

[1] 510(k) pending. Compressed Sensing Cardiac Cine is not commercially available. Future availability cannot be guaranteed.

Imaging of Vascular Calcification Using PETRA and StarVIBE

Marcos P. Botelho[1,2]; Shivraman Giri[3]; Ioannis Koktzoglou[1,4]; Robert R. Edelman[1,2]; James Carr[1]

[1] Northwestern Memorial Hospital, Chicago, IL, USA
[2] NorthShore University HealthSystem, Evanston, IL, USA
[3] Siemens Healthineers, Chicago, IL, USA
[4] University of Chicago Pritzker School of Medicine, Chicago, IL, USA

New horizons for MRI of vascular calcifications

The presence of dense peripheral vascular calcifications has negative prognostic implications in patients with peripheral arterial disease (PAD). In addition, the presence of dense calcifications may alter the choice of access site for patients undergoing percutaneous revascularization or TAVR (transcatheter aortic valve replacement) procedures. Peripheral MR angiography is commonly used as an alternative to CT angiography for the evaluation of patients with PAD. While peripheral vascular calcifications are readily depicted with CT angiography, they are inapparent with MR angiography (MRA).

In this work, we present an approach that combines nonenhanced MRA with tailored 3D imaging of vascular calcifications. While QISS[1] is used for nonenhanced MRA, we propose two options for imaging of vascular calcifications:

1. PETRA, which relies on the use of an ultra-short echo time.
2. StarVIBE – as part of FREEZEit – which acquires data using a stack-of-stars *k-space* trajectory. Briefly, we adjust the echo time such that fat and water signals are in-phase, and apply a very small flip angle for the RF excitation which minimizes the impact of T1 relaxation time differences among tissues. This approach generates a homogenous signal level across most tissues, except for calcifications appear dark due to a very short T2* relaxation time. The use of StarVIBE is also helpful in minimizing motion sensitivity in the abdominal and pelvic regions compared with a fully Cartesian 3D acquisition.

[1] Requires QISS license on the scanner.

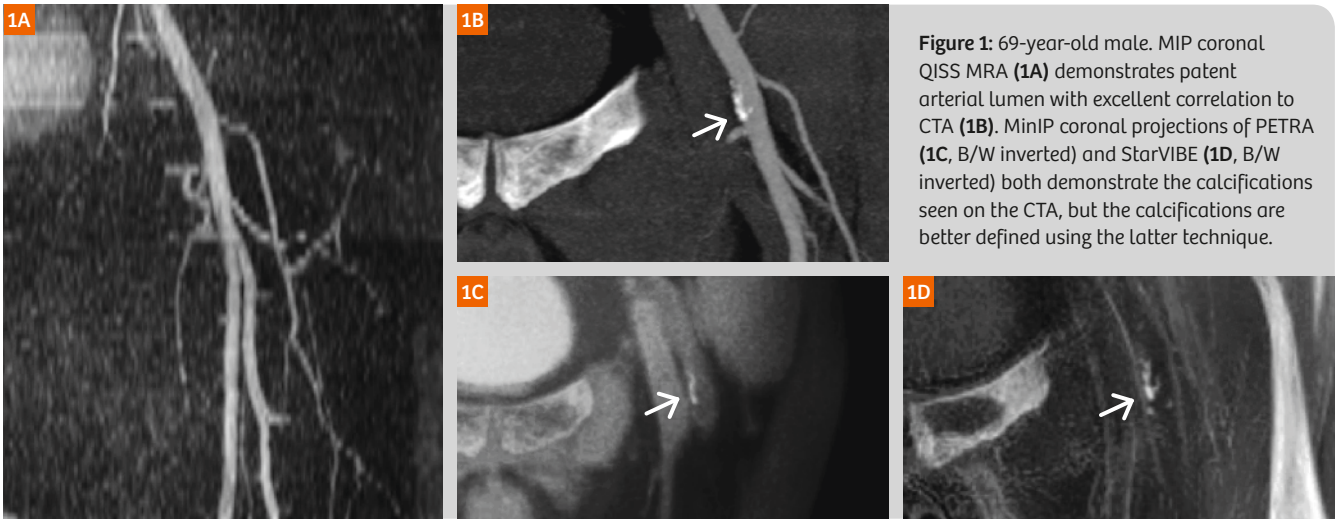

Figure 1: 69-year-old male. MIP coronal QISS MRA **(1A)** demonstrates patent arterial lumen with excellent correlation to CTA **(1B)**. MinIP coronal projections of PETRA **(1C**, B/W inverted) and StarVIBE **(1D**, B/W inverted) both demonstrate the calcifications seen on the CTA, but the calcifications are better defined using the latter technique.

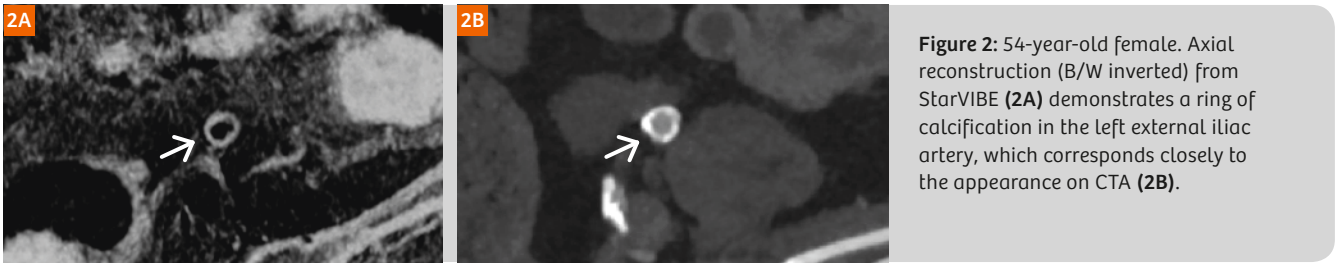

Figure 2: 54-year-old female. Axial reconstruction (B/W inverted) from StarVIBE **(2A)** demonstrates a ring of calcification in the left external iliac artery, which corresponds closely to the appearance on CTA **(2B)**.

How to build your protocol on *syngo*.MR E11A 1.5T MAGNETOM Aera-XQ system?

1. PETRA approach
One can start with the default PETRA protocol that can be found in the following location:

Default →
→ Sequence Region →
→ Siemens Seq →
→ Default.

The parameters to be updated are as follows:

Parameter name	Tab combination	Value
Orientation	Routine	Coronal
TR	Contrast/Common	4.7
TE	Contrast/Common	0.07
Flip angle	Contrast/Common	5
Table position mode	System/ Miscellaneous	ISO
Radial views	Resolution/Common	60000
FOV read	Resolution/Common	400
Base resolution	Resolution/Common	384
Bandwidth	Sequence/Part1	338

Table 1: Protocol adaptations required for PETRA sequence to image calcification. Please start with the default protocol that can be found on scanner at: Default → Sequence Region → Siemens Seq → Default

2. StarVIBE approach
(requires FREEZEit license):
One can start with any of the StarVIBE sequences. We started with the one in following location:

SIEMENS →
→ abdomen →
→ library → 3D

The parameters to be updated are as follows:

Parameter name	Tab combination	Value
Orientation	Routine	Coronal
Slice thickness	Routine	1.0
Slice Oversampling	Routine	25.0
Slices per slab	Routine	128
TR	Contrast/Common	7.61
TE	Contrast/Common	4.77
Flip angle	Contrast/Common	3.5
Fat suppr.	Contrast/Common	None
Table position mode	System/ Miscellaneous	ISO
Radial views	Resolution/Common	600
FOV read	Resolution/Common	416
Base resolution	Resolution/Common	416
Slice resolution	Resolution/Common	75%
Optimization	Sequence/Part1	In phase
Bandwidth	Sequence/Part1	300
Incr. Gradient spoiling	Sequence/Part2	Yes

Please make sure that fat-suppression and centric ordering are turned off.

Table 2: Protocol adaptations required for StarVIBE sequence to image vascular calcification. Please start with the protocol that can be found on scanner at: SIEMENS → abdomen → library → 3D

PETRA	StarVIBE
Sensitive to motion	Insensitive to motion
Available on all *syngo*.MR E11 systems	Part of the FREEZEit option

Suggestions for 3T imaging

1. For PETRA: No change required.
2. For StarVIBE: Please use the above values from MAGNETOM Aera-XQ, and then change the following TE = 2.46 ms, Flip angle = 2.5°, TR = 4.8 ms.

Post-processing to generate CT-like images

Both MR sequences generate images that make calcifications appear dark. This can be changed by going to the 'Image' menu, choosing the 'Color Lookup Table' option, and then selecting 'Inverted Gray Scale'. Now the calcifications appear bright – just like in CT. Use of a minimum intensity projection (MinIP) can improve display of the vascular calcifications.

Discussion

We have shown that angiography and calcification imaging can be accomplished using nonenhanced MR approaches during a single scan session. We presented two approaches for imaging of vascular calcification, one based on PETRA and the other on StarVIBE. In our experience so far, the StarVIBE outperforms PETRA due to its insensitivity to motion and overall image sharpness. A more detailed analysis, including 3T results, can be found in our recently published article "MR Imaging of Iliofemoral Peripheral Vascular Calcifications using Proton Density-Weighted, In-Phase Three-Dimensional Stack-of-Stars Gradient Echo" by Edelman et al. in *Magnetic Resonance in Medicine*, 2016.

Coils: Body matrix coils were used in our studies.

Contact

Marcos P. Botelho, M.D.

Northwestern University
Department of Radiology

Evanston, IL, USA
marcos.botelho@
fsm.northwestern.edu

Compressed Sensing: Application to Time-of-Flight MR Angiography

Takayuki Yamamoto; Tomohisa Okada; Koji Fujimoto; Yasutaka Fushimi; Akira Yamamoto; Kaori Togashi

Department of Diagnostic Imaging and Nuclear Medicine, Kyoto University, Kyoto, Japan

Introduction

Time-of-Flight MR Angiography (TOF MRA) is a reliable method to visualize the cerebral vasculature and is widely used in clinical practice. It is a non-invasive technique, which is free from radiation exposure and adverse effects of contrast materials. The main concerns of high-resolution TOF MRA are its long scan time and decreased signal-to-noise ratio (SNR).

Compressed sensing (CS) provides a novel approach to restore the original image quality from fewer *k-space* acquisitions by exploiting intrinsic sparsity in the imaged object combined with iterative reconstruction and its denoising capabilities. MRA is a good candidate for CS because of the high signal in the vessels which are sparse in space [1]. The combination of parallel acquisition (PAT) and CS can significantly reduce the examination time [3].

Scan time reduction is important not only for economic reasons but also to reduce the burden on the patient and to limit motion artifacts which can disrupt vascular depictions. In this case study, we will describe our early experiences with Compressed Sensing (CS) TOF[1] MRA in various clinical patients to visualize the cerebral arteries.

CS TOF technique

For data acquisition, a conventional 3D TOF gradient-echo sequence was combined with random sampling. For this purpose, the *k-space* of each imaging slab was subsampled in the k_y-k_z phase-encoding with a variable density Poisson disk sampling pattern. In the pattern, the sampling density was gradually increased from periphery toward the center of *k-space* to optimize the acquisition of data in high image-energy central *k-space* regions and hence enhance signal-to-noise ratio (SNR). The incoherence of the random sampling pattern would lead to artifacts that scatter across the whole image in a 'noise-like' manner after Fourier transform. A fully sampled region in the center of *k-space* was utilized to estimate the coil sensitivity maps.

After data acquisition, the image can be recovered from the sub-sampled data by nonlinear, iterative reconstruction.

[1] WIP, Compressed Sensing TOF is currently under development and is not for sale in the US and in other countries. Its future availability cannot be ensured.

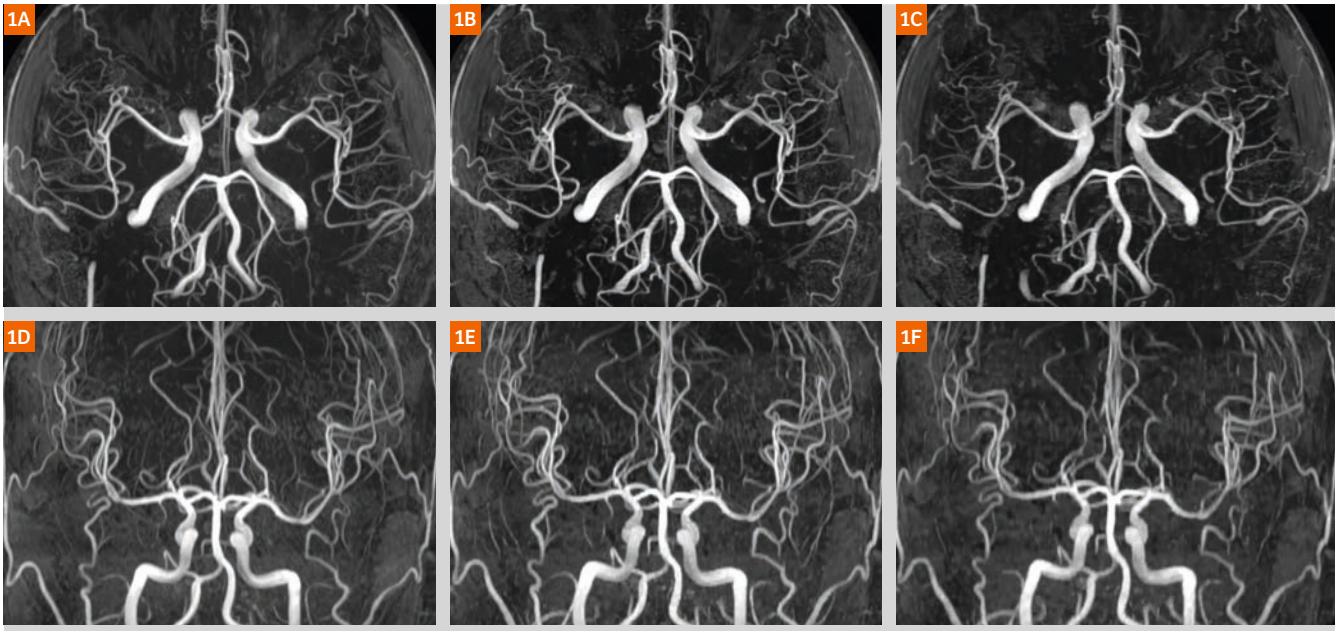

Figure 1: Axial **(1A–C)** and coronal **(1D–F)** MIP images of a healthy subject (35-year-old, male) reconstructed from full-sampling data **(1A, D)**, 3.4-fold net acceleration **(1B, E),** and 6.4-fold net acceleration **(1C, F)**, respectively.

In this reconstruction, the images were reconstructed by solving the following minimization problem [4–6]:

$$\min_{x} ||Ax - y||_2^2 + \lambda ||\Phi(x)||_1$$

where y is the acquired *k-space* data and x the estimated image. The system matrix, A, describes the data acquisition process, which is required for the comparison of the image and acquired data. The transform sparsity term enforces a sparse representation of the image. For this purpose, the image is transformed a sparse representation by Φ(·), for example, using the redundant Haar wavelet transform. The balance between data fidelity and sparsity is adjusted with the regularization parameter λ, which was empirically set to 0.0002. The iterative reconstruction process was terminated after 20 iterations.

Imaging was performed at a clinical 3T MR scanner (MAGNETOM Skyra, Siemens Healthcare, Erlangen, Germany) with a 32-channel head coil. Parameters for the imaging protocol were TR 20 ms, TE 3.7 ms, flip angle 18° and bandwidth 189 Hz/Px. In total, 5 slabs were acquired with 20% slice oversampling with a matrix of 384 x 326 x 90 and a voxel size of 0.3 x 0.3 x 0.35 mm (FOV 220 x 190 cm). The images of conventional TOF imaging with a PAT factor of 2 and 3 were compared to those acquired with CS TOF featuring acceleration rates from 3.4 up to 6.4.

Image reconstruction was done directly on the scanner with standard hardware.

Imaging examples of cerebral angiography with CS TOF

Figures 1 and 2 show images of healthy subjects. On maximum intensity projection (MIP) images, cerebral arteries are well visualized in CS TOF images with acceleration rates from 3.4 up to 6.4 (Fig. 2). Although the depiction of distal branches become weaker at a higher acceleration rate (Fig. 3), the visualization of proximal branches was acceptable, which is important to diagnose the steno-occlusive diseases or cerebral aneurysms. We have previously reported that the diagnostic quality of distal branches was maintained with nominal acceleration factor of 6, which achieved a shorter acquisition time of less than half of the conventional PAT acceleration of 2 [1].

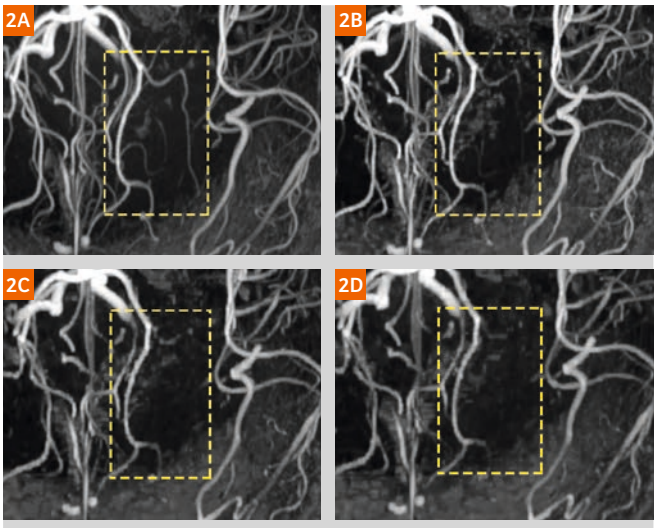

Figure 2: Magnified view of MIP images for the same subject as in Figure 1. Net acceleration rates are **(2A)** full sampling, **(2B)** 3.4, **(2C)** 6.4, and **(2D)** 7.1. Most of the arterial branches are visualized well, but small branch with lower signal is a challenge for CS TOF (shown with rectangles in yellow dashed lines).

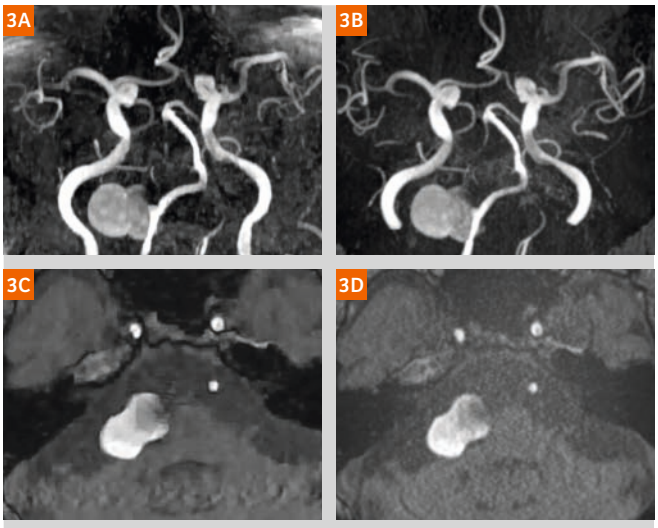

Figure 3: An aneurysm of the right vertebral artery in a 68-year-old male. **(3A, C)** CS TOF with net acceleration rate of 6.1, and **(3B, D)** conventional TOF MRA (using PAT factor of 3 in the phase encoding direction and partial Fourier of 7/8) with a net acceleration rate of 3.

Case 1

68-year-old male was followed up for a large aneurysm of right vertebral artery for several years (Fig. 4). The aneurysm gradually increased in size, and the patient was admitted to our hospital. The size and the gourd-like shape of the aneurysm are well depicted in CS TOF. There is almost no difference in the MIP image between CS TOF and conventional TOF, although CS TOF is twice as fast.

Figure 4: Two aneurysms of the right internal carotid artery (arrows). **(4A)** CS TOF with a net acceleration rate of 6.1 and **(4B)** conventional TOF with a net acceleration rate of 3.

Case 2

78-year-old female was admitted to our hospital because of left hemiplegia. Two aneurysms in the right internal carotid artery (Fig. 5) are incidentally found. Both aneurysms are well visualized in spite of their small sizes.

Figure 5: Stenosis of the left internal carotid artery (circle). **(5A)** CS TOF with a net acceleration rate of 6.1 and **(5B)** conventional TOF with a net acceleration rate of 3.

Figures 3 through 6 show cases in clinical practices. The result images of CS TOF and conventional TOF are displayed side by side to facilitate comparison of vascular shape. Conventional TOF used modified GRAPPA (acceleration factor of 3) and partial Fourier technique (7/8 for the phase and the slice direction). A net acceleration rate of 6.1 was used for CS TOF for all cases. Matrix size of conventional TOF was kept the same as CS TOF, but the number of slab was 3, which was set to 5 for CS TOF. The acquisition time for conventional TOF was 3 min 11 sec.

Conclusion

CS TOF can drastically reduce the scan time while minimizing loss of image quality at high acceleration rates. In some cases, residual sub-sampling artifacts remain in the reconstructed images, however without influencing the image quality of the MIP angiogram remarkably. The first experiences indicate that a diagnostic image quality can be achieved in clinical setting using highly accelerated CS TOF for the visualization of cerebral arteries. Our results warrants future larger clinical studies in a larger cohort to find the optimal balance between acquisition speed and high resolution.

Acknowledgements

The kind support of Aurelien F. Stalder, Yutaka Natsuaki, and Michaela Schmidt, employees in research and development functions of Siemens Healthineers, is greatly appreciated.

Case 3

74-year-old male with diabetes mellitus. The routine examination for diabetes revealed a severe stenosis of left internal carotid artery (Fig. 6). The lesion is similarly depicted both in CS TOF and conventional TOF. Arterial irregularity is additionally seen at the proximal portion of right internal carotid artery only in CS TOF, which gives the impression of stronger stenotic change. An influence of motion is possibly suspected.

Figure 6: Stenosis of the left middle cerebral artery (arrows). **(6A)** CS TOF with a net acceleration rate of 6.1 and **(6B)** conventional TOF with a net acceleration rate of 3.

References

1 Yamamoto T, Fujimoto K, Okada T, Fushimi Y, Stalder AF, Natsuaki Y, et al. Time-of-Flight Magnetic Resonance Angiography With Sparse Undersampling and Iterative Reconstruction. Invest Radiol. 2015 Nov [epub ahead of print].
2 Fushimi Y, Fujimoto K, Okada T, Yamamoto A, Tanaka T, Kikuchi T, et al. Compressed Sensing 3-Dimensional Time-of-Flight Magnetic Resonance Angiography for Cerebral Aneurysms. Invest Radiol. 2016 Apr;51(4):228–35.
3 Liang D, Liu B, Wang J, Ying L. Accelerating SENSE using compressed sensing. Magn Reson Med. 2009 Dec;62(6):1574–84.
4 Beck A, Teboulle M. A Fast Iterative Shrinkage-Thresholding Algorithm for Linear Inverse Problems. SIAM J Imaging Sci. 2009 Jan;2(1):183–202.
5 Liu J, Rapin J, Chang T-C, Lefebvre A, Zenge M, Mueller E, et al. Dynamic cardiac MRI reconstruction with weighted redundant Haar wavelets. Proceedings of the 20th Annual Meeting of the ISMRM, Melbourne, Australia; 2012. p. 4249.
6 Stalder AF, Schmidt M, Quick HH, Schlamann M, Maderwald S, Schmitt P, et al. Highly undersampled contrast-enhanced MRA with iterative reconstruction: Integration in a clinical setting. Magn Reson Med. 2014 Dec 17.

Contact


Takayuki Yamamoto


Tomohisa Okada

Tomohisa Okada, M.D., Ph.D.

Human Brain Research Center
Graduate School of Medicine
Kyoto University

54 Shogoin-Kawaharacho,
Sakyo-ku
Kyoto 606-8507
Japan
tomokada@kuhp.kyoto-u.ac.jp


Koji Fujimoto


Yasutaka Fushimi


Akira Yamamoto


Kaori Togashi

Improving Dynamic MR Angiography: Iterative TWIST

Bernd J. Wintersperger[1,2]; Luigia D'Errico[1,2]; Christoph Forman[3]; Jens Wetzl[4]; Michaela Schmidt[3]; Aurelien F. Stalder[3]

[1] Department of Medical Imaging, Peter Munk Cardiac Centre, University Health Network, Toronto, Ontario, Canada
[2] Department of Medical Imaging, University of Toronto, Toronto, Ontario, Canada
[3] Siemens Healthcare, Erlangen, Germany
[4] Pattern Recognition Lab, Department of Computer Science, FAU Erlangen-Nürnberg, Erlangen, Germany

Introduction

Nowadays, many vascular territories are explored non-invasively for the purpose of diagnosis, therapy planning and surveillance of vascular disease. Invasive catheter angiography is almost exclusively being used during therapy and intervention. However, the benefits of invasive approaches include the ability to visualize dynamics of applied dye and may therefore provide additional information on the potential hemodynamic relevance of vascular disease or stenosis.

In recent years, magnetic resonance angiography (MRA) has become a dominant tool of non-invasive high-resolution delineation of body and peripheral vasculature. With the ever increasing importance of continuous surveillance in genetic aortic disease (e.g. Marfan's, Ehlers-Danlos, Loeys-Dietz, etc.), the role of MRA developed beyond atherosclerotic disease and focuses more often on a younger population.

Most commonly, outside the brain, contrast-enhanced MRA (CE-MRA) techniques are being employed sampling a high-resolution data set after a contrast agent timing bolus.

In order to overcome the limitations of purely static MRA, various techniques such as time-resolved imaging of contrast kinetics (TRICKS) and time-resolved angiography with stochastic trajectories (TWIST) are being employed [1, 2]. The predominant underlying principle of these approaches relates to keyhole imaging with more frequent sampling of central *k*-space data vs. peripheral *k*-space data. In addition to commonly applied acceleration techniques (e.g. partial Fourier, parallel imaging, etc.), dynamic CE-MRA also relies on view-sharing for peripheral *k*-space coverage in order to improve temporal resolution (Figs. 1–2).

Dynamic CE-MRA using TWIST has proven beneficial and successful in the diagnosis of disease across vessel territories from head to toe [3–5]. Besides a direct vascular focus, the relatively high temporal resolution 3D coverage, combined with prominent T1-weighting and background tissue suppression, has been applied to tissue perfusion studies.

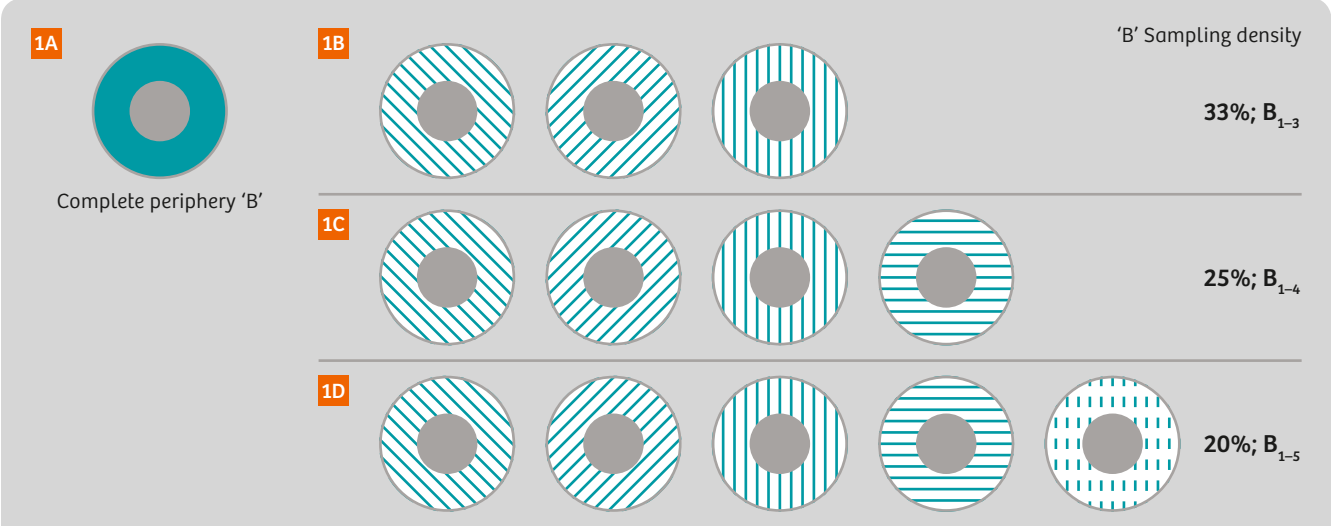

Figure 1: In TWIST, sampling of the **(1A)** complete peripheral *k*-space (region 'B') can be achieved by the variation of the sampling density **(1B–D)**. With a sampling density of **(1B)** 33%, the peripheral *k*-space is subdivided into 3 different samplings, while for sampling densities of **(1C)** 25% and **(1D)** 20%, peripheral *k*-space acquisition requires 4 or 5 different samplings, respectively.

Dynamic contrast-enhanced MRA with iterative TWIST

With repeated updates of the central *k*-space data, the dynamic pass of a Gadolinium-based contrast agent (GBCA) can be followed through the vasculature of interest without the need for a timed bolus. However, while the sharing of peripheral *k*-space data across multiple time points provides an improved update rate of images (apparent 'temporal resolution'), it also results in a prolongation of the 'temporal footprint' of TWIST (Fig. 2). Especially in areas of possible motion and fast blood circulation (e.g. chest, pulmonary vasculature), this may result in inconsistencies, temporal blurring and subsequent image degradation, specifically of small vasculature.

Recent interest in Compressed Sensing approaches successfully demonstrated benefits of these techniques in various MR applications including CE-MRA [6] and dynamic CE-MRA [7, 8]. The potential benefits of such iterative reconstruction approaches have recently been explored in clinical scenarios [8, 9].

Iterative TWIST (IT-TWIST)[1] uses the sampling pattern of a regular TWIST acquisition, but does not rely on view sharing during image reconstruction. Instead, the implemented iterative reconstruction algorithm relies on the intrinsic incoherent sampling pattern of the peripheral *k*-space data and uses a Compressed Sensing approach with spatial and temporal regularization to suppress artifacts arising from *k*-space undersampling.

More in detail, the TWIST acquisition consists of interleaved acquisitions of central *k*-space (region 'A') and different incoherent sub-samplings of peripheral *k*-space (region 'B'). Regular TWIST reconstruction then combines multiple 'B' regions (view sharing) with one 'A' region to form a coherently subsampled *k*-space suitable for parallel imaging reconstruction (see Figures 1, 2). In contrast, the iterative TWIST reconstruction uses a single region 'A' and region 'B' pair per time frame, thus decreasing the 'temporal footprint' to be identical to the 'image update rate' (apparent 'temporal resolution') (Fig. 3). To recover the individual time frames despite the higher undersampling, a non-linear iterative SENSE reconstruction is being used. The iterative reconstruction uses spatio-temporal regularization based on Haar wavelets [8, 10]. This reconstruction process results in a considerable computational burden and therefore is carried out on the Graphics Processing Unit (GPU) of the standard image reconstruction system. Depending on detailed acquisition parameters and time frames current reconstruction times are about 20 minutes.

[1] WIP. IT-TWIST is work in progress and is not commercially available. Future availability cannot be guaranteed.

2

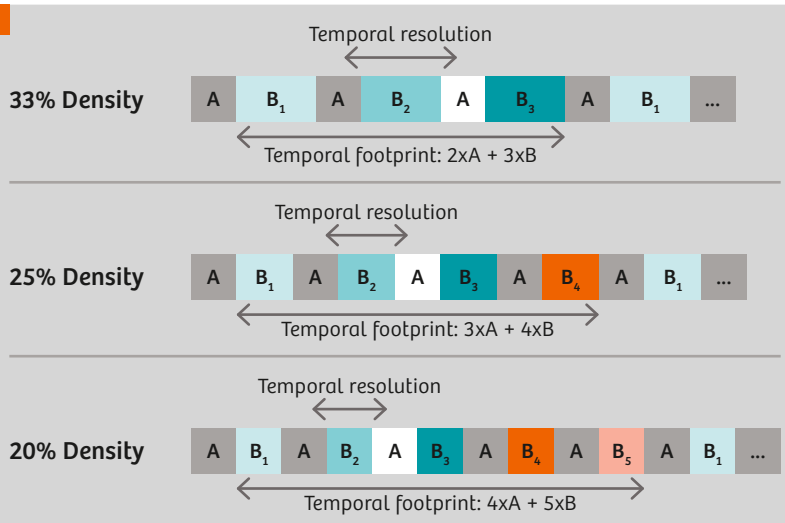

Figure 2: Assuming a fixed size of the central *k*-space (region 'A') sampling in TWIST, a reduction in the density of the peripheral *k*-space (region 'B') sampling results in an improved temporal resolution but simultaneously also prolongs the temporal footprint of the technique. Temporal resolution in TWIST refers to the distance of two adjacent 'A' regions and as such reflects the contrast agent dynamics while the temporal footprint describes the time from beginning to the end of all data sampling used for a single time frame data reconstruction. As shown, the prolongation of the temporal footprint mainly relates to the update of the central *k*-space (region 'A') between the different peripheral *k*-space samplings (region 'B').

3

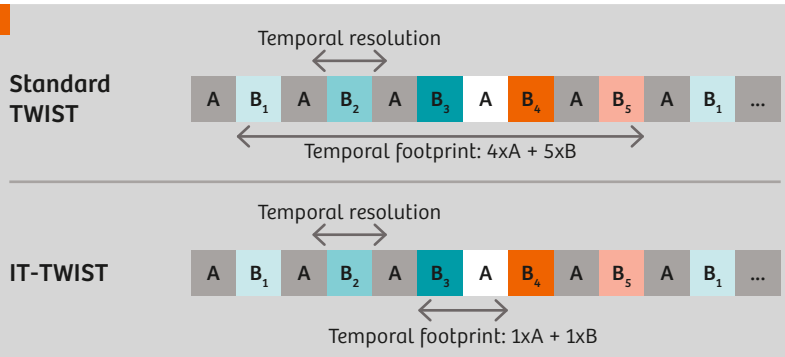

Figure 3: Iterative TWIST (IT-TWIST) allows a substantial shortening of the temporal footprint in data reconstruction. While in standard TWIST a complete coverage of region 'B' is required (sampling density of 20% shown), IT TWIST reconstruction reduces the temporal footprint to a single 'B' region in addition to the respective central *k*-space (region 'A'). This is achieved by the incoherent sampling pattern of region 'B' in TWIST and application of a Compressed Sensing reconstruction approach with spatial and temporal regularization.

Parameter name	Value
FoV	333 x 380 x 88 mm³
Voxel size (measured)	1.2 x 1.0 x 1.2 mm³
Voxel size (interpolated)	1.0 x 1.0 x 1.0 mm³
iPAT	4 x 2
TR / TE / Flip angle	2.89 ms / 1.05 ms / 17°
'A' region (sampling density)	15%
'B' region (sampling density)	20%
Temporal resolution (apparent)	2.4 s

Table 1: Imaging protocol.

In order to assess the impact of such improved 'temporal footprints' and increased signal-to-noise ratio (SNR) of the CS reconstruction algorithm due to de-noising, we aimed at patients referred for the assessment of the thoracic aorta and the great thoracic vessels. The applied imaging protocol focused on high temporal and spatial resolution [8] (Table 1). All imaging was performed on a 64-channel MAGNETOM Skyra^{fit} system and contrast enhancement for TWIST was provided by automated injection of Gadobutrol (Gadavist, Bayer Pharma, Berlin) [8]. All acquired raw data sets were reconstructed twice: using the (1) standard product reconstruction as well as the above described (2) IT-TWIST reconstruction.

In all patients, IT-TWIST was equal or superior to TWIST reconstruction; in fact, in the vast majority of cases, image quality as assessed by two readers with respect to aortic contrast-to-noise (CNR), aortic delineation and medium-to-

4

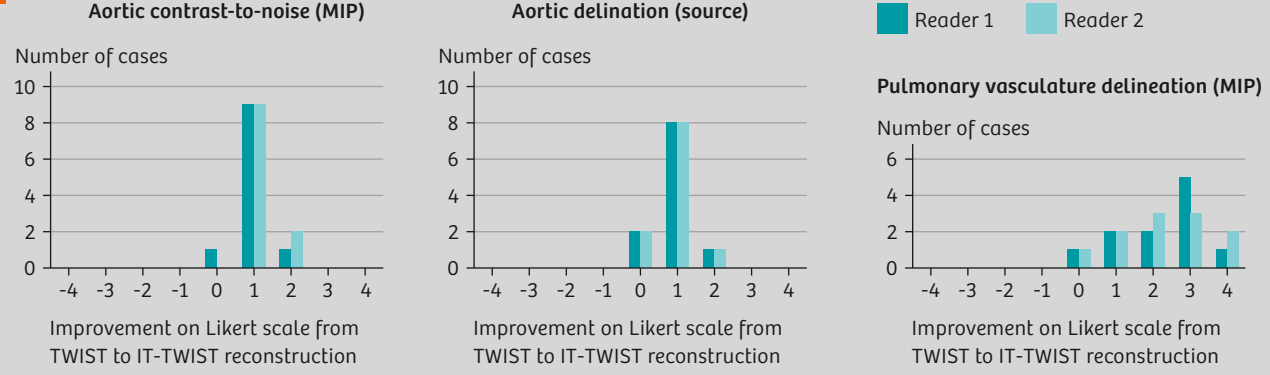

Figure 4: Selection of imaging parameters of the applied TWIST acquisition. Contrast enhancement was provided by injection of 8 ml of (1:3) diluted (saline) gadolinium based contrast agent.

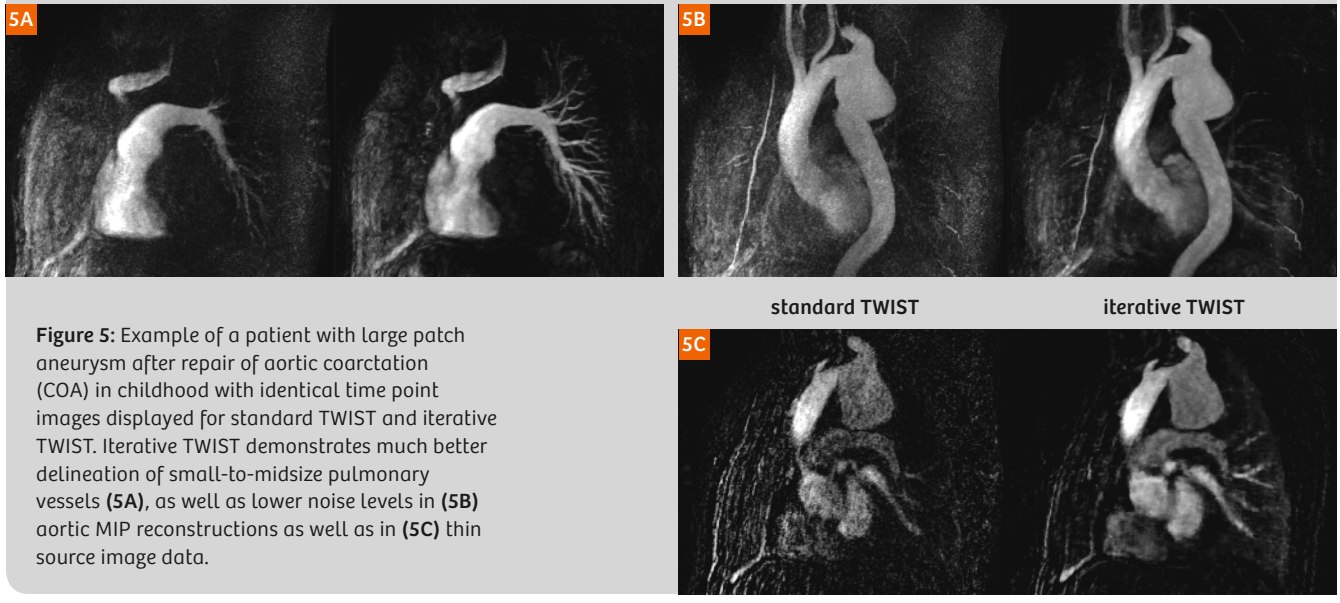

Figure 5: Example of a patient with large patch aneurysm after repair of aortic coarctation (COA) in childhood with identical time point images displayed for standard TWIST and iterative TWIST. Iterative TWIST demonstrates much better delineation of small-to-midsize pulmonary vessels **(5A)**, as well as lower noise levels in **(5B)** aortic MIP reconstructions as well as in **(5C)** thin source image data.

small vessel (pulmonary vasculature) delineation improved by at least 1 point on the Likert scale (0 = non-diagnostic; 1 = poor; 2 = fair; 3 = good; 4 = excellent) [9] (Figs. 4–6). The most prominent improvement with IT-TWIST was seen in the area of medium-to-small vessels of the pulmonary vasculature, which also demonstrated an improvement in the signal response amplitude as compared to TWIST [8] (Figs. 4–6).

Conclusion

Initial experiences of IT-TWIST in clinical thoracic imaging with dynamic CE-MRA demonstrate extremely promising results, especially when focusing on the medium-to-small sized pulmonary vasculature. The specific improvement within the pulmonary vasculature most likely relates to the substantially shortened 'temporal footprint' with IT-TWIST. This approach allows to further push temporal resolution by lowering sampling density of the peripheral *k*-space. As the principles of Compressed Sensing maintain a reasonable SNR and CNR level, a further push of spatial resolution by using higher parallel imaging accelerations is possible. While experience in other vascular territories is currently limited at our site, further exploration will determine the possible benefit across the body vasculature and also the impact of IT-TWIST on detailed parameters of vessel boundaries and vessel size. Furthermore, it will provide insights into the possibly required adaptation of specific factors of the reconstruction based on territory, image quality need and acceleration.

Nevertheless, IT-TWIST represents an important step ahead towards high spatial/high temporal resolution dynamic CE-MRA of the future. This will provide a straightforward inject-and-shoot CE-MRA protocol without the need for any bolus timing and quite possibly also result in changes of the required contrast agent volumes.

Figure 6: In a patient with suspicion of a dilated ascending aorta the iterative TWIST again demonstrates a much improved delineation of the **(6A)** pulmonary vasculature and **(6B)** lower noise levels for the aorta on MIP reconstruction.

References

1 Korosec FR, Frayne R, Grist TM, Mistretta CA (1996) Time-resolved contrast-enhanced 3D MR angiography. Magn Reson Med 36:345-351.
2 Song T, Laine AF, Chen Q, Rusinek H, Bokacheva L, Lim RP, Laub G, Kroeker R, Lee VS (2009) Optimal *k*-space sampling for dynamic contrast-enhanced MRI with an application to MR renography. Magn Reson Med 61:1242-1248.
3 Jeong HJ, Vakil P, Sheehan JJ, Shah SJ, Cuttica M, Carr JC, Carroll TJ, Davarpanah A (2011) Time-resolved magnetic resonance angiography: evaluation of intrapulmonary circulation parameters in pulmonary arterial hypertension. J Magn Reson Imaging 33:225-231.
4 Kinner S, Quick HH, Maderwald S, Hunold P, Barkhausen J, Vogt FM (2013) Triple-TWIST MRA: high spatial and temporal resolution MR angiography of the entire peripheral vascular system using a time-resolved 4D MRA technique. Eur Radiol 23:298-306.
5 Lohan DG, Tomasian A, Saleh RS, Singhal A, Krishnam MS, Finn JP (2009) Ultra-low-dose, time-resolved contrast-enhanced magnetic resonance angiography of the carotid arteries at 3.0 tesla. Invest Radiol 44:207-217.
6 Stalder AF, Schmidt M, Quick HH, Schlamann M, Maderwald S, Schmitt P, Wang Q, Nadar MS, Zenge MO (2015) Highly undersampled contrast-enhanced MRA with iterative reconstruction: Integration in a clinical setting. Magn Reson Med 74:1652-1660.
7 Rapacchi S, Natsuaki Y, Plotnik A, Gabriel S, Laub G, Finn JP, Hu P (2015) Reducing view-sharing using compressed sensing in time-resolved contrast-enhanced magnetic resonance angiography. Magn Reson Med 74:474-481.
8 Wetzl J, Forman C, Wintersperger BJ, D'Errico L, Schmidt M, Mailhe B, Maier A, Stalder AF (2016) High-resolution dynamic CE-MRA of the thorax enabled by iterative TWIST reconstruction. Magn Reson Med. 10.1002/mrm.26146.
9 D'Errico L, Schmidt, M., Wetzl J, Forman C, Stalder AF, Wintersperger BJ (2016) Improved Dynamic Contrast-Enhanced Magnetic Resonance Angiography (CE-MRA) using Iterative Data Reconstruction. Journal of Cardiovascular Magnetic Resonance 18:O112.
10 Forman C, Piccini D, Grimm R, Hutter J, Hornegger J, Zenge MO (2015) Reduction of respiratory motion artifacts for free-breathing whole-heart coronary MRA by weighted iterative reconstruction. Magn Reson Med 73:1885-1895.

Contact

Bernd J. Wintersperger, MD EBCR FAHA

Department of Medical Imaging

Toronto General Hospital, 1 PMB-273
585 University Avenue
Toronto, Ontario, M5G 2N2, Canada
+1 416-340-4800 ex. 8593
Bernd.Wintersperger@uhn.ca

4D Flow MRI – an Update

Michael Markl, Ph.D.[1,2]; James Carr, M.D.[1]; Michael Rose, B.S.[3]; Cynthia K. Rigsby, M.D.[1,3,4]; Julia Geiger, M.D.[1]

[1] Department of Radiology, Feinberg School of Medicine, Northwestern University, Chicago, USA
[2] Department Biomedical Engineering, McCormick School of Engineering, Northwestern University, Chicago, USA
[3] Department of Medical Imaging, Ann & Robert H. Lurie Children's Hospital of Chicago, Chicago, USA
[4] Department of Pediatrics, Feinberg School of Medicine, Northwestern University, Chicago, USA

Introduction

MRI techniques provide non-invasive and non-ionizing methods for the accurate anatomic depiction of the cardiovascular system. In addition, the intrinsic sensitivity of MRI to motion offers the unique ability to acquire blood flow simultaneously with anatomical data within a single measurement (phase contrast (PC) principle). The characterization of the dynamic components of blood flow with MRI has achieved considerable progress in recent years including new methodological advances such as 4D Flow MRI for the comprehensive *in-vivo* analysis of complex time-resolved 3D blood flow characteristics [1–7].

Standard clinically employed 2D CINE PC MRI takes advantage of the direct relationship between blood flow velocity and the MR signal to measure blood flow velocity along a single direction, similar to Doppler echocardiography [8]. Typical clinical imaging protocols measure blood flow in 2D imaging slices positioned orthogonal to the vessel which usually includes single-direction velocity measurement (through-plane encoding) and is performed during a 10–15 second breath-hold period. The resulting images are used to quantify flow parameters such as peak velocity, net flow, or regurgitant fraction at the site of the imaging plane.

In 4D Flow MRI[1], velocity is encoded along all three spatial dimensions throughout the cardiac cycle, thus providing a time-resolved 3D velocity field. As a result, 4D Flow MRI can provide full volumetric coverage of the vessel of interest and thus give more comprehensive spatial and temporal (4D = 3D + time) coverage. In this article, we describe the latest technical progress and data analysis protocols of the 4D Flow MRI for the Siemens platform, and we present different examples for clinical cardiothoracic and intracranial applications.

[1] The product is still under development and not commercially available yet. Its future availability cannot be ensured.

Technical advances

4D Flow data acquisition

Initial limitations for including 4D Flow MRI into clinical daily routine standard MRI protocols were related to long scan times of up to 20 minutes. Methodological improvements based on k-t parallel imaging or Compressed Sensing have been successfully employed to achieve significant imaging acceleration and reduced times [9, 10]. Combination with advanced respiration control [11, 12] for cardiothoracic and abdominal applications today allows the acquisition of 4D Flow MRI data within clinically acceptable scan times on the order of 5–10 minutes.

Continued developments based on alterative data sampling strategies such as radial or spiral data readout have high potential to further reduce scan times. For example, a recent study showed that the combination of highly efficient spiral sampling with dynamic compressed sensing can achieve major acceleration, which allowed for the acquisition of abdominal 4D Flow MRI data during a single breath-hold [10]. Ongoing methodological improvements focus on the acquisition of dual-venc acquisitions [13–15] which are expected to be of great benefit for the simultaneous assessment of low and fast flow velocities, e.g. in the brain or in congenital heart disease (CHD), where a high dynamic

	venc	respiration gating, R_{eff}	acceleration factor R	spatial resolution	temporal resolution	total scan time
aorta/PA	150–400 cm/s	60–80%	5	$(2.2–2.8\ mm)^3$	35–45 ms	5–8 min
whole heart	150–400 cm/s	60–80%	5	$(2.8–3.2\ mm)^3$	35–45 ms	8–12 min
head	80–120 cm/s	N/A	5	$(1.0–1.2\ mm)^3$	35–45 ms	8–10 min
abdomen	60–120 cm/s	60–80%	5	$(2.5–3.0\ mm)^3$	35–45 ms	10–15 min

Table 1: 4D Flow MR imaging scenarios for different application areas based on adult subjects with heart rates on the order of 60–70 bpm. For cardiothoracic and abdominal applications, respiratory navigator gating is typically used to minimize breathing artifacts. The combination with advanced data acquisition strategies (respiratory driven phase encoding) allows for high scan efficiencies (R_{eff}) on the order of 60–80%. The selection of the lower end of the velocity sensitivity (venc) is based on the expected maximal normal blood flow velocities in each vascular territory which will have to be adapted to higher velocities in patients with cardiovascular disease such as aortic valve stenosis. PA = pulmonary artery.

range is critical to cover the wide arterial and venous flow velocity spectrum.

A summary of imaging protocols for different application areas is provided in Table 1 and illustrates currently achievable spatio-temporal resolution and scan times based on recently described *k*-t accelerated 4D Flow MRI methods with high acceleration factors of R = 4 – 6 [16–18].

4D Flow data analysis workflow

For the visualization of cardiovascular flow patterns, commonly used techniques are 3D streamlines and time-resolved 3D pathlines to depict changes in hemodynamics associated with disease. Figure 1 illustrates the use of 3D streamlines to depict systolic 3D flow patterns in the thoracic aorta of a patient with a bicuspid aortic valve. Time-resolved 3D pathlines utilize the full 4D (3D and time) information and can be used to visualize the spatio-temporal dynamics of pulsatile 3D blood flow patterns.

An example of aortic 4D Flow MRI and comparison of the resulting imaging findings with standard MRI techniques is shown in Figure 1. A benefit compared to traditional 2D PC-MR imaging is related to the possibility for retrospective and flexible quantification and visualization of cardiovascular blood flow without being limited to 2D planes as in standard 2D CINE PC MRI. 4D Flow MRI offers a single and easy to prescribe data acquisition (3D volume covering cardiovascular region of interest) instead of multiple 2D planes for flow analysis with standard 2D CINE PC MRI that may be difficult to position in cases with complex vascular architecture (e.g. congenital heart disease, liver vasculature). As a result, 4D Flow MRI may help to avoid missing regions of interest for flow quantification where 2D CINE PC MRI may not have been acquired or planes were misplaced. Recent studies have confirmed that volumetric analysis based on 4D Flow MRI allows for improved assessment of aortic and pulmonary peak velocities which may be underestimated by 2D CINE PC MRI [19, 20].

The anatomic and velocity information of the 4D Flow data can additionally be used to calculate a 3D phase contrast angiogram (3D PC-MRA) which can be combined with 3D blood flow visualization to guide anatomic orientation (see Figs. 1–3). In addition, the 3D PC-MRA data serve as a basis for the 3D segmentation of vessels to improve 3D visualization or to provide the ability to mask the underlying velocity data to calculate systolic 3D velocity maximum intensity projections (MIP). As shown in Figure 2C, systolic velocity MIPs are an easy to use tool to give an overview over the 3D velocity distribution as well as automated quantification of peak velocities v_{peak} and thus estimate pressure gradients Δp using the simplified Bernoulli equation ($\Delta p = 4v_{peak}^2$). The increased complexity of 4D Flow data (3D + time + 3-directional velocities) offers the opportunity to derive new physiologic and pathophysiologic hemodynamic parameters, such as wall shear stress (WSS), pulse wave velocity, 3D pressure difference maps, or turbulent kinetic energy. These advanced hemodynamic measures can provide quantitative information on the impact of vascular pathologies on cardio- or cerebro-

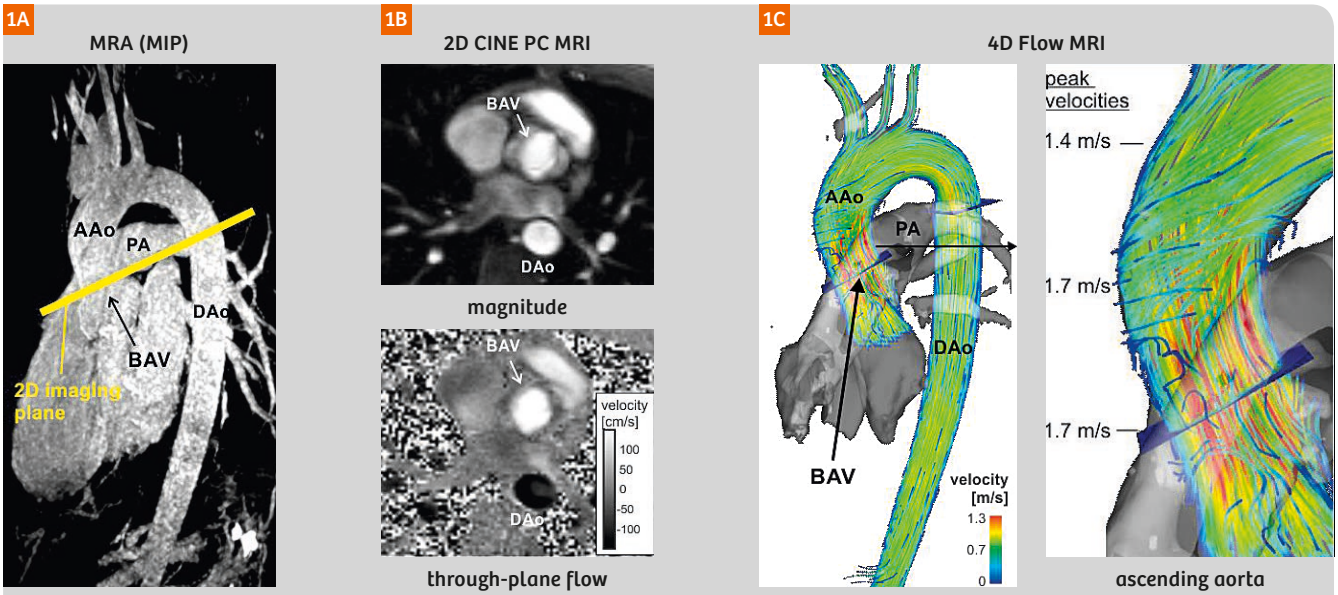

Figure 1: MR angiography (MRA, depicted as a maximum intensity projection, MIP) and 2D CINE PC-MRI in a patient with bicuspid aortic valve (BAV) disease. The patient underwent standard MR angiography **(1A)** as well as 2D CINE PC-MRI **(1B)** for the assessment of valve morphology and flow quantification at the level of the aortic valve in the ascending aorta (AAo). 1B shows the maximum aortic valve opening and blood flow during peak systole. The yellow line in 1A shows the imaging plane for 2D CINE PC-MRI acquisitions in 1B. **(1C)** 3D streamline visualization of systolic blood flow in the thoracic aorta as assessed by 4D Flow MRI. Note that 4D Flow MRI provides full volumetric coverage of the thoracic aorta and flexible retrospective quantification of peak systolic velocities at multiple locations in the thoracic aorta which revealed a peak velocity of 1.7 m/s distal to the BAV. DAo = descending aorta, PA = pulmonary artery

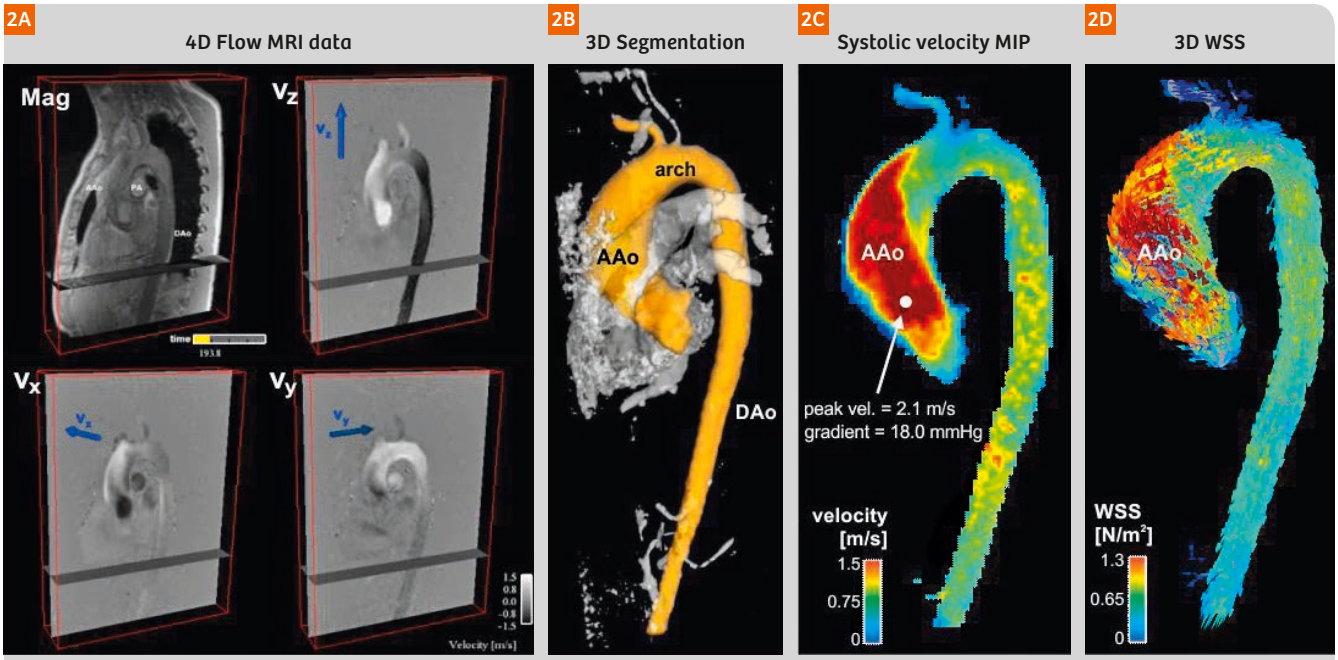

Figure 2: Data analysis workflow for the assessment of aortic velocity distribution and 3D WSS in a patient with bicuspid aortic valve (BAV) and ascending aortic (AAo) dilatation. **(2A)** 4D Flow MRI data with full volumetric coverage of the thoracic aorta including anatomical and 3-directional flow data. **(2B)** 3D segmentation based on 3D PC-MRA data (gray shaded iso-surface) is used to isolate the aortic lumen. **(2C)** The 3D segmentation is used to mask the measured time-resolved 3D velocity data and calculate a systolic velocity maximum intensity projection (MIP). The velocity MIP data can be used to automatically extract the peak systolic velocity and pressure gradient (estimated via the simplified Bernoulli equation) without the need for manual analysis plane placement. Results indicate mild BAV stenosis causing mildly elevated pressure gradient. **(2D)** Advanced hemodynamic analysis can be employed to map peak systolic wall shear stress (WSS) vectors onto the aortic surface which indicate substantially elevated WSS (red color) along the outer curvature of the ascending aorta. DAo = descending aorta.

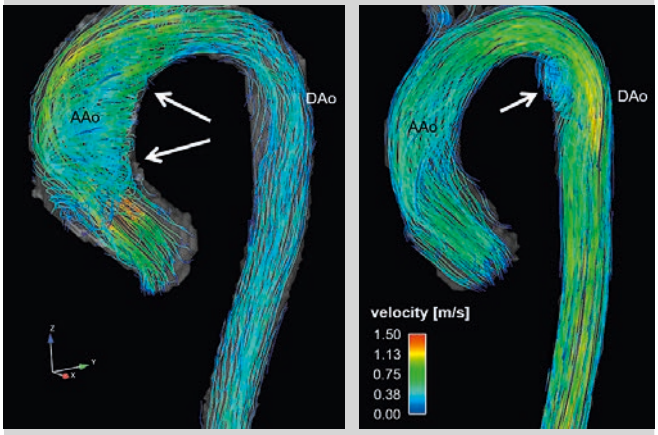

Figure 3: Systolic 3D streamline visualization in two patients with different aortic disease. **(3A)** 56-year-old patient with bicuspid aortic valve (BAV) demonstrates pronounced helix flow in the dilated ascending aorta (AAo) while blood flow in the descending aorta (DAo) is normal. **(3B)** In contrast, this 22-year-old patient with Marfan syndrome who has no marked aortic ectasia shows physiological flow in the AAo but an abnormal localized vortex flow pattern in the proximal DAo.

vascular blood flow patterns beyond currently available techniques. For example, methods have been developed to compute volumetric 3D WSS, a known pathophysiological parameter implicated in vascular remolding, along the segmented surface of the entire aorta (Fig. 2D) [21, 22]. The application of this technique in patients with aortic disease demonstrated that a 3D WSS mapping technique allows for compact visualization and regional quantification of hemodynamic parameters assessed across multiple subjects [23].

For a detailed overview of 4D Flow MRI developments and its use for 3D flow visualization and quantification throughout the human circulatory systems the reader is referred to a number of recently published review articles [1–7] and 4D Flow MRI consensus statement [24].

Clinical applications

In recent years, 4D Flow MRI has been increasingly applied in various vessel territories and diseases ranging from aortic pathologies to complex CHD, abdominal indications and intracranial applications.

Thoracic aorta

A number of studies indicate the important role of 4D Flow MRI for the comprehensive analysis of the impact of focal

4A

anterior view

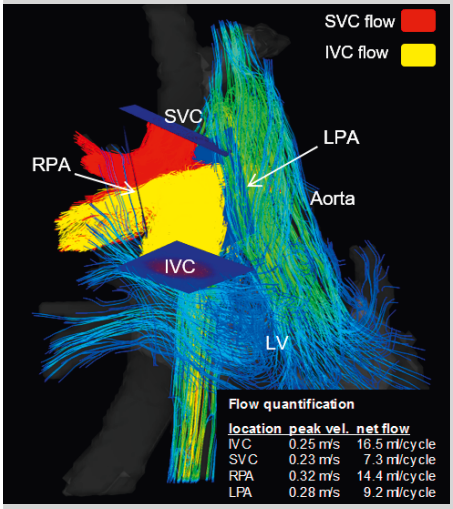

4B

posterior view

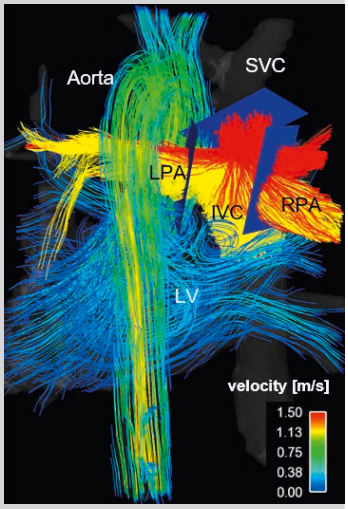

Figure 4: (4A) Blood flow visualization based on 3D streamlines in a 16-year-old patient with tricuspid atresia and palliative surgical repair with connection of the upper and lower caval veins directly to the right pulmonary artery (RPA) with detour of the right heart in the so called Fontan procedure. **(4B)** Color coded streamlines illustrate the distribution of venous flow originating in the superior caval vein (SVC, red) and inferior caval vein (IVC, yellow) towards the RPA and left pulmonary artery (LPA). Retrospective flow quantification allows for the assessment of peak velocities and flow volumes in the vessels of interest **(4A).** Blood flow in the left ventricle and aorta is color-coded to local flow velocity in this example.

5

left anterior view

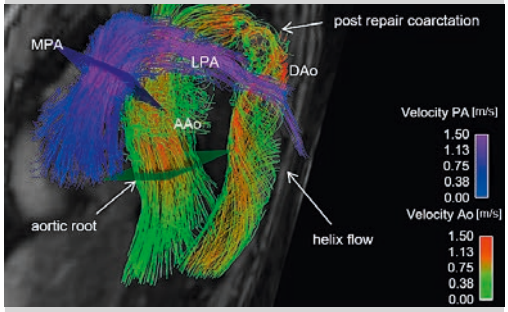

Flow quantification

location	peak vel.	net flow
aortic root	1.10 m/s	105 ml/cycle
MPA	2.26 m/s	99 ml/cycle

Figure 5: 3D flow pattern in a 15-year-old patient with d-transposition of the great arteries (d-TGA) after arterial switch procedure depicting the typical postoperative anatomy of the main and branch pulmonary arteries without relevant postsurgical obstruction shown for main and left pulmonary artery (MPA, LPA). Color-coded streamlines according to vessel origin and velocity reveal the flow distribution in the pulmonary arteries (blue-purple) and the aorta (green-red) during systole. Note the marked helix flow in the DAo as a result after associated coarctation repair.

aortic abnormalities (aortic valve abnormality, coarctation, aortic dilatation) or genetic disorders (e.g. Marfan syndrome) on changes in 3D blood flow affecting the entire aorta [25–28]. Changes in flow patterns due to aortic valve stenosis or congenitally abnormal valves such as bicuspid aortic valve (BAV) affect predominantly the ascending aorta but can also expand into the aortic arch and descending aorta. In addition, the application of 4D Flow MRI in patients with aortic coarctation provides an overview of the hemodynamic changes which are not limited to the coarctation site and might be overlooked or misjudged by 2D CINE PC MRI. In addition, flow derived parameters such as WSS have shown high potential to derive better understanding of the underlying pathophysiology for aortic disease progression. Figure 3 depicts flow alterations in two representative patients with focal (BAV) and global (Marfan) aortic disease.

Complex congenital heart disease

Whole heart 4D Flow MRI techniques allow for a non-invasive comprehensive assessment of cardiovascular hemodynamics in the heart and its surrounding great vessels. While scan times are still long due to full volumetric coverage of the entire heart (8–12 minutes depending on heart rate and respiration control efficiency), it facilitates the systematic assessment of blood flow in multiple vessels and enables the retrospective analysis of any region of interest within the imaging volume. The examination of the pulmonary arteries and the right heart commonly has priority in CHD, and postsurgical assessment of the pulmonary blood flow is crucial to rule out potential re-stenoses or postsurgical sequelae which need re-intervention such as in patients with tetralogy of Fallot, transposition of the great arteries, or in subjects with functional single ventricle (see Figs. 4 and 5). Correct plane placement and flow assessment by 2D CINE PC MRI is particularly challenging in these cases. Previous studies have shown that the 4D Flow technique can reliably identify altered 3D flow characteristics related to the post-interventional status in patients with CHD. In addition, 4D Flow MRI based flow quantification has been shown to be equivalent or even improved when compared to 2D techniques, while needing less imaging time than time needed for positioning and acquisition of multiple planes [29–33].

Cerebrovascular disease

In clinical practice, transcranial Doppler ultrasound is routinely used for cerebrovascular flow measurements. However, the technique is operator-dependent and significantly limited by the available acoustic windows of the head, mainly in adults. 2D PC-MRI can provide flow measurements in large intracranial arteries and veins.

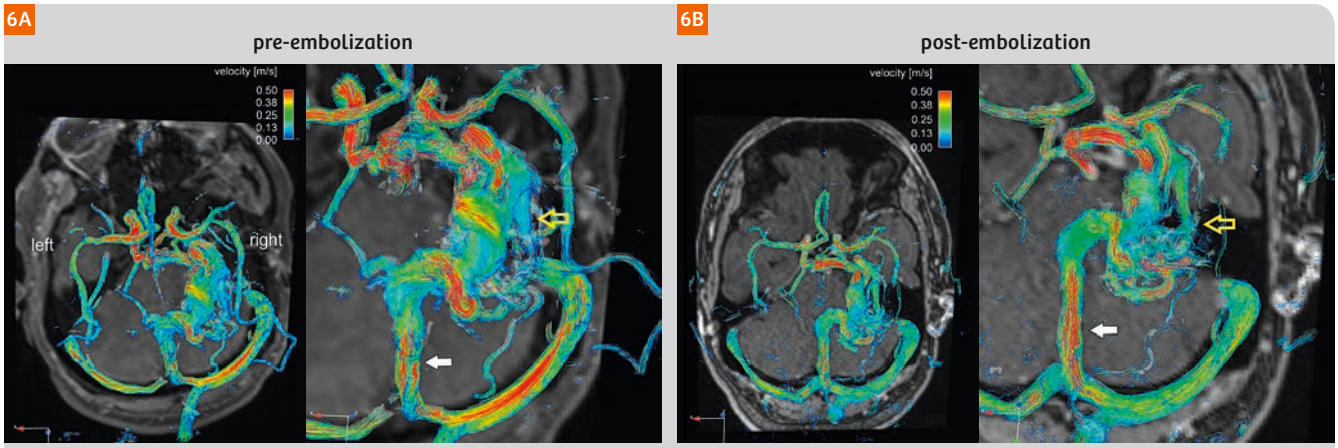

Figure 6: Intracranial 4D Flow MRI for the assessment of arterial and venous cerebrovascular hemodynamics. 3D blood flow visualization using time-integrated 3D pathlines in a 29-year-old male patient with a large unruptured AVM centered in the right mesial temporal lobe with compact nidus prior to treatment **(6A)** and following invasive staged embolization therapy **(6B:** DSA guided endovascular superselective occlusion of AVM feeding arteries with nidal penetration). Complex arterial feeding and convoluted hemodynamics as well as differences in pre- and post-embolization vascularization and hemodynamics are clearly visible. Staged embolization resulted in compaction of the AVM with reduced blood flow velocities (yellow arrows) and reduced flow velocities for venous drainage (white arrow).

However, small and tortuous vessels, complex vascular anatomy and the need for the manual placement of 2D imaging planes in multiple vessel segments represent challenges [34]. In contrast, 4D Flow MRI offers 3D blood flow visualization and retrospective flow quantification with full coverage of cerebral arteries and veins. Emerging applications include the hemodynamic evaluation of intracranial aneurysms, arteriovenous malformations (AVM), and intracranial atherosclerotic disease (ICAD), as well as venous flow. Figure 6 demonstrates the potential of 4D Flow MRI for the evaluation of global and regional AVM flow characteristics and treatment-induced changes in cerebrovascular flow distribution [35, 36]. In patients with cerebral AVMs, the pathological vascularization (direct shunting of blood from arterial to the venous sides without an intervening capillary bed) leads to abnormal hemodynamics. Flow information is potentially valuable for a better understanding of the impact of a focal AVM on the flow redistribution in the brain and/or in treatment planning by attempting to identify the feeding arteries with highest flow, enabling efficient and targeted embolization treatment.

Conclusion

A large number of studies have provided evidence that 4D Flow MRI can help to better understand altered hemodynamics in patients with cardiovascular diseases and may lead to improved patient management and monitoring of therapeutic responses. The novel hemodynamic insights obtained are also likely to provide new risk stratification metrics in patients that have prognostic significance and can also impact individualized treatment decisions to optimize patient outcome. Future research efforts will improve the clinical applicability of 4D Flow MRI and provide results in larger cohort studies.

References

1 Ebbers T. Flow imaging: cardiac applications of 3D cine phase-contrast MRI. Current Cardiovascular Imaging Reports. 2011;4:127-133.
2 Markl M, Kilner PJ, Ebbers T. Comprehensive 4D velocity mapping of the heart and great vessels by cardiovascular magnetic resonance. J Cardiovasc Magn Reson. 2011;13:7.
3 Frydrychowicz A, Francois CJ, Turski PA. Four-dimensional phase contrast magnetic resonance angiography: Potential clinical applications. Eur J Radiol. 2011.
4 Markl M, Frydrychowicz A, Kozerke S, Hope M, Wieben O. 4D flow MRI. J Magn Reson Imaging. 2012;36:1015-1036.
5 Hope MD, Sedlic T, Dyverfeldt P. Cardiothoracic magnetic resonance flow imaging. J Thorac Imaging. 2013;28:217-230.
6 Stankovic Z, Allen BD, Garcia J, Jarvis KB, Markl M. 4D flow imaging with MRI. Cardiovasc Diagn Ther. 2014;4:173-192.
7 Vasanawala SS, Hanneman K, Alley MT, Hsiao A. Congenital heart disease assessment with 4D flow MRI. J Magn Reson Imaging. 2015;42:870-886.
8 Nayak KS, Nielsen JF, Bernstein MA, Markl M, P DG, R MB, Saloner D, Lorenz C, Wen H, B SH, Epstein FH, J NO, Raman SV. Cardiovascular magnetic resonance phase contrast imaging. J Cardiovasc Magn Reson. 2015;17:71.
9 Schnell S, Markl M, Entezari P, Mahadewia RJ, Semaan E, Stankovic Z, Collins J, Carr J, Jung B. k-t GRAPPA accelerated four-dimensional flow MRI in the aorta: Effect on scan time, image quality, and quantification of flow and wall shear stress. Magn Reson Med. 2014;72:522-533.
10 Dyvorne H, Knight-Greenfield A, Jajamovich G, Besa C, Cui Y, Stalder A, Markl M, Taouli B. Abdominal 4D Flow MR Imaging in a Breath Hold: Combination of Spiral Sampling and Dynamic Compressed Sensing for Highly Accelerated Acquisition. Radiology. 2015;275:245-254.
11 Uribe S, Beerbaum P, Sorensen TS, Rasmusson A, Razavi R, Schaeffter T. Four-dimensional (4D) flow of the whole heart and great vessels using real-time respiratory self-gating. Magnetic resonance in medicine. 2009;62:984-992.
12 van Ooij P, Semaan E, Schnell S, Giri S, Stankovic Z, Carr J, Barker AJ, Markl M. Improved respiratory navigator gating for thoracic 4D flow

MRI. Magn Reson Imaging. 2015;33:992-999.
13 Ha H, Kim GB, Kweon J, Kim YH, Kim N, Yang DH, Lee SJ. Multi-VENC acquisition of four-dimensional phase-contrast MRI to improve precision of velocity field measurement. Magnetic resonance in medicine. 2016;75:1909-1919.
14 Binter C, Knobloch V, Manka R, Sigfridsson A, Kozerke S. Bayesian multipoint velocity encoding for concurrent flow and turbulence mapping. Magn Reson Med. 2013;69:1337-1345.
15 Macgowan CK, Liu GK, van Amerom JF, Sussman MS, Wright GA. Self-gated Fourier velocity encoding. Magn Reson Imaging. 2010;28:95-102.
16 Griswold MA, Jakob PM, Heidemann RM, Nittka M, Jellus V, Wang J, Kiefer B, Haase A. Generalized autocalibrating partially parallel acquisitions (GRAPPA). Magn Reson Med. 2002;47:1202-1210.
17 Baltes C, Kozerke S, Hansen MS, Pruessmann KP, Tsao J, Boesiger P. Accelerating cine phase-contrast flow measurements using k-t BLAST and k-t SENSE. Magn Reson Med. 2005;54:1430-1438.
18 Jung B, Stalder AF, Bauer S, Markl M. On the undersampling strategies to accelerate time-resolved 3D imaging using k-t-GRAPPA. Magn Reson Med. 2011;66:966-975.
19 Nordmeyer S, Riesenkampff E, Messroghli D, Kropf S, Nordmeyer J, Berger F, Kuehne T. Four-dimensional velocity-encoded magnetic resonance imaging improves blood flow quantification in patients with complex accelerated flow. Journal of magnetic resonance imaging : JMRI. 2013;37:208-216.
20 Rose MJ, Jarvis K, Chowdhary V, Barker AJ, Allen BD, Robinson JD, Markl M, Rigsby CK, Schnell S. Efficient method for volumetric assessment of peak blood flow velocity using 4D flow MRI. J Magn Reson Imaging. 2016, published online.
21 Potters WV, van Ooij P, Marquering H, Vanbavel E, Nederveen AJ. Volumetric arterial wall shear stress calculation based on cine phase contrast MRI. Journal of magnetic resonance imaging: JMRI. 2014:1-12.
22 van Ooij P, Potters WV, Nederveen AJ, Allen BD, Collins J, Carr J, Malaisrie SC, Markl M, Barker AJ. A methodology to detect abnormal relative wall shear stress on the full surface of the thoracic aorta using four-dimensional flow MRI. Magn Reson Med. 2015;73:1216-1227.
23 Guzzardi DG, Barker AJ, van Ooij P, Malaisrie SC, Puthumana JJ, Belke DD, Mewhort HE, Svystonyuk DA, Kang S, Verma S, Collins J, Carr J, Bonow RO, Markl M, Thomas JD, McCarthy PM, Fedak PW. Valve-Related Hemodynamics Mediate Human Bicuspid Aortopathy: Insights From Wall Shear Stress Mapping. J Am Coll Cardiol. 2015;66:892-900.
24 Dyverfeldt P, Bissell M, Barker AJ, Bolger AF, Carlhall CJ, Ebbers T, Francios CJ, Frydrychowicz A, Geiger J, Giese D, Hope MD, Kilner PJ, Kozerke S, Myerson S, Neubauer S, Wieben O, Markl M. 4D flow cardiovascular magnetic resonance consensus statement. J Cardiovasc Magn Reson. 2015;17:72.
25 Barker AJ, Markl M, Burk J, Lorenz R, Bock J, Bauer S, Schulz-Menger J, von Knobelsdorff-Brenkenhoff F. Bicuspid aortic valve is associated with altered wall shear stress in the ascending aorta. Circ Cardiovasc Imaging. 2012;5:457-466.
26 Allen BD, van Ooij P, Barker AJ, Carr M, Gabbour M, Schnell S, Jarvis KB, Carr JC, Markl M, Rigsby C, Robinson JD. Thoracic aorta 3D hemodynamics in pediatric and young adult patients with bicuspid aortic valve. J Magn Reson Imaging. 2015;42:954-963.
27 Frydrychowicz A, Markl M, Hirtler D, Harloff A, Schlensak C, Geiger J, Stiller B, Arnold R. Aortic Hemodynamics in Patients With and Without Repair of Aortic Coarctation: In Vivo Analysis by 4D Flow-Sensitive Magnetic Resonance Imaging. Invest Radiol. 2011;46:317-325.
28 Geiger J, Markl M, Herzer L, Hirtler D, Loeffelbein F, Stiller B, Langer M, Arnold R. Aortic flow patterns in patients with Marfan syndrome assessed by flow-sensitive four-dimensional MRI. J Magn Reson Imaging. 2012;35:594-600.
29 Nordmeyer S, Riesenkampff E, Crelier G, Khasheei A, Schnackenburg B, Berger F, Kuehne T. Flow-sensitive four-dimensional cine magnetic resonance imaging for offline blood flow quantification in multiple vessels: a validation study. J Magn Reson Imaging. 2010;32:677-683.
30 van der Hulst AE, Westenberg JJ, Kroft LJ, Bax JJ, Blom NA, de Roos A, Roest AA. Tetralogy of fallot: 3D velocity-encoded MR imaging for evaluation of right ventricular valve flow and diastolic function in patients after correction. Radiology. 2010;256:724-734.
31 Hsiao A, Alley MT, Massaband P, Herfkens RJ, Chan FP, Vasanawala SS. Improved cardiovascular flow quantification with time-resolved volumetric phase-contrast MRI. Pediatric radiology. 2011;41:711-720.
32 Valverde I, Nordmeyer S, Uribe S, Greil G, Berger F, Kuehne T, Beerbaum P. Systemic-to-pulmonary collateral flow in patients with palliated univentricular heart physiology: measurement using cardiovascular magnetic resonance 4D velocity acquisition. J Cardiovasc Magn Reson. 2012;14:25.
33 Gabbour M, Schnell S, Jarvis K, Robinson JD, Markl M, Rigsby CK. 4-D flow magnetic resonance imaging: blood flow quantification compared to 2-D phase-contrast magnetic resonance imaging and Doppler echocardiography. Pediatr Radiol. 2015;45:804-813.
34 Schubert T, Bieri O, Pansini M, Stippich C, Santini F. Peak velocity measurements in tortuous arteries with phase contrast magnetic resonance imaging: the effect of multidirectional velocity encoding. Invest Radiol. 2014;49:189-194.
35 Ansari SA, Schnell S, Carroll T, Vakil P, Hurley MC, Wu C, Carr J, Bendok BR, Batjer H, Markl M. Intracranial 4D Flow MRI: Toward Individualized Assessment of Arteriovenous Malformation Hemodynamics and Treatment-Induced Changes. AJNR Am J Neuroradiol. 2013;34:1922-1928.
36 Wu C, Ansari SA, Honarmand AR, Vakil P, Hurley MC, Bendok BR, Carr J, Carroll TJ, Markl M. Evaluation of 4D Vascular Flow and Tissue Perfusion in Cerebral Arteriovenous Malformations: Influence of Spetzler-Martin Grade, Clinical Presentation, and AVM Risk Factors. Am J Neuroradiol. 2015;36:1142-1149.


James Carr

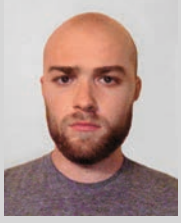
Michael Rose

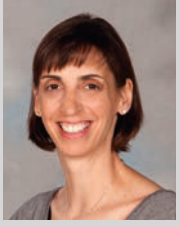
Cindy Rigsby


Julia Geiger


Michael Markl

Contact

Michael Markl, Ph.D.

Department of Radiology

Northwestern University
737 N. Michigan Avenue Suite 1600
Chicago, Illinois 60611, USA
Phone: +1 312-695-1799
Fax: +1 312-926-5991
mmarkl@northwestern.edu

Meet Siemens Healthineers

Engineering success. Pioneering Healthcare. Together.

Our brand name Siemens Healthineers embodies our pioneering spirit and engineering expertise in the healthcare industry. The people working for Siemens Healthineers are highly passionate about providing medical technology that improves your clinical, operational and financial performance, leading also to positive patient experience. With this issue we start to introduce colleagues from all over the world to you – people who put their hearts into what they do.

Christian Geppert

Erlangen, Germany

Christian Geppert graduated in physics from University of Bremen in 2005. After joining Siemens he worked in oncology predevelopment and most recently in PET/MR. Since January 2017 he succeeds Edgar Müller as the head of the MR Cardiovascular Predevelopment Team.

"I have the pleasure of taking over a team of four scientists in Erlangen with many years of experience and renown in the field. I am also in charge of coordinating our global predevelopment projects together with my colleagues in the respective countries. After several years in collaborations – in New York – and in marketing, I am excited to return to the predevelopment field, where I started my career within Siemens."

How did you first come in contact with MRI?
I started to work in MR back in 2000 during my diploma thesis on spectroscopic imaging and my fascination for MR has never stopped. I remember my first ISMRM 2001 in Glasgow, seeing movies of the beating heart for the first time – I was blown away.

What is most fascinating about MRI?
When my son was in Kindergarten he told his friends that his dad had a machine at work that could see inside the human body – but his friends thought this was impossible.

What I have always loved about my jobs in Siemens is that I have continuously been working with our partners – outstanding researchers as well as leading radiologists – and that I have been involved in identifying innovations, helping them gain maturity and finally clinical acceptance. Even when you have been working in the field of MRI for a while – when you see an exciting new technique come to light for the first time, this is always a great moment.

What do you think are the most important developments in MRI and in Healthcare?
For MRI in general, acceleration and robustness as realized in Compressed Sensing and motion insensitive scanning. For Healthcare in general, I think it is the (slow) rise of evidence-based medicine.

What would you do, if you could do for one month whatever you wanted?
To actually work in a clinical environment for an extended amount of time is something that is extremely helpful. While I had the pleasure to do this at times, given the vast range of partners that we have, you can never have sufficient knowledge about the real life usage of our products. It can be truly eye opening. Outside of work, I would love to spend a month to focus on making music (electronics, guitar), which is something that I usually don't find the time for.

Christianne Leidecker graduated in Physics from the Friedrich-Alexander University (FAU), Erlangen, Germany in 2000. She then went on to obtain a Ph.D. at the Institute for Medical Physics at the FAU on the topic of automatic exposure control in Computed Tomography. In 2006, she joined Siemens as a Collaboration Manager in the US CT collaboration group based out of Philadelphia. 2010, she returned to Germany to head Global Collaborations for CT. Since July 2016 she has held the position of Head of the Cardiac Functional Team and Central Zone Director in the US MR Collaboration Team in Chicago. In this position, she works closely with our research partners in the US as well as the R&D team in headquarters.

Christianne Leidecker

Chicago, USA

How did you first come in contact with MRI?
Having started my career in medical imaging with CT, MR was, for the longest time, "the other" imaging modality. Every now and then, in discussions with clinicians and physicists, the discussions would turn to MR and this is how it slowly but surely crept its way into my life. To me, it was always fascinating how much we could learn from each other across the different modalities. So when the opportunity opened up to head the US CMR team out of Chicago, I grabbed it!

What is most fascinating about your job?
I have been working “in collaborations” since I left academia and joined Siemens. What fascinates me most about it is the unique opportunity to provide a bridge between clinical researchers and our development teams at Siemens. Working with our luminary partners and our excellent engineers enables us to translate cutting-edge research into products and clinical routine benefiting a large patient population. Innovation has always been a particular strength of Siemens, and collaborating closely with the scientific community has always been a pillar of our innovation strategy. I feel very privileged to be able to contribute.

What would you do, if you could do for one month whatever you wanted?
Well, first and foremost, I would negotiate for 6 weeks 🙂 and then use this opportunity to do my Scuba Dive Master with my diving friends in Roatan, Honduras. Since my first dive in 2010 I have been fascinated by the peace and quiet and wonders of the underwater world and blowing bubbles became my favorite past time.

If I had one month to spend on my job, I would spend a week each with four different research partners at their institution and/or hospital.

What is most motivating about your job?
While a little hesitant in the beginning because of my CT background, I found it tremendously enriching to translate this to MR and I very much enjoy discussions with all those who are guiding me on this way. Cardiac MR is a fascinating field with tremendous opportunities and I look forward to participating in this development.

The entire editorial staff at Charité Campus Buch, HELIOS-Clinics Berlin Buch and at Siemens Healthineers extends their appreciation to all the radiologists, technologists, physicists, experts and scholars who donate their time and energy – without payment – in order to share their expertise with the readers of MAGNETOM Flash.

MAGNETOM Flash – Imprint

Publisher:
Siemens Healthcare GmbH
Magnetic Resonance,
Karl-Schall-Str. 6, D-91052 Erlangen, Germany

Editor-in-chief:
Antje Hellwich
(antje.hellwich@siemens-healthineers.com)

Guest Editor:
Prof. Dr. Jeanette Schulz-Menger
University Medicine Berlin, Charité Campus Buch
Experimental Clinical Research Center (ECRC)
HELIOS Clinics Berlin Buch
Department of Cardiology and Nephrology
Schwanebecker Chaussee 50, D-13125 Berlin, Germany
Phone: +49 30 040153536
jeanette.schulz-menger@charite.de

Editorial Board:
Reto Merges; Wellesley Were; Sunil Kumar S.L., Ph.D.;
Gary R. McNeal, MS (BME)

Review Board:
Christoph Forman, Edgar Müller, Efren Ojeda,
Michaela Schmidt, Christian Schuster, Ph.D.,
Susanne von Vietinghoff

Production:
Norbert Moser,
Siemens Healthcare GmbH

Layout:
Agentur Baumgärtner,
Friedrichstr. 4, D-90762 Fürth, Germany

Printer:
G. Peschke Druckerei GmbH,
Taxetstr. 4, D-85599 Parsdorf b. Munich, Germany

We welcome your questions and comments about the editorial content of MAGNETOM Flash. Please contact us at magnetomworld.med@siemens.com.

Manuscripts as well as suggestions, proposals and information are always welcome; they are carefully examined and submitted to the editorial board for attention. MAGNETOM Flash is not responsible for loss, damage, or any other injury to unsolicited manuscripts or other materials. We reserve the right to edit for clarity, accuracy, and space. Include your name, address, and phone number and send to the editors, address above.

MAGNETOM Flash is also available online:

www.siemens.com/magnetom-world

Siemens Healthineers Publications

Our publications offer the latest information and background for every healthcare field. From the hospital director to the radiological assistant – here, you can quickly find information relevant to your needs.

MAGNETOM Flash
Everything from the world of magnetic resonance imaging.

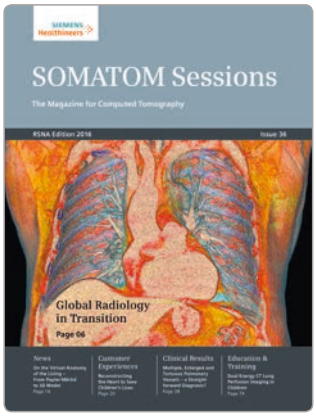

SOMATOM Sessions
Everything from the world of computed tomography.

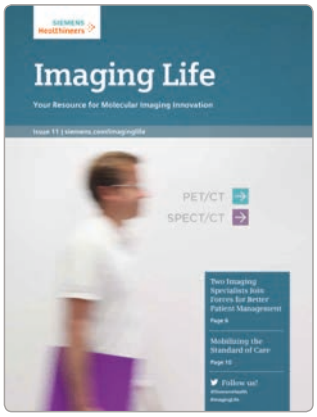

Imaging Life
Everything from the world of molecular imaging innovations.

AXIOM Innovations
Everything from the world of interventional radiology, cardiology, and surgery.

Go HYBRID!
Everything from the world of image-guided therapy.

Medical Solutions Online
Innovations and trends in healthcare.
The magazine is designed especially for members of hospital management, administration personnel, and heads of medical departments. Read online at:
siemens.com/medical-solutions

For current and past issues, and to order the magazines, please visit
siemens.com/healthcare-magazine

MAGNETOM Flash

Issue Number 67, 1/2017
SCMR Edition

siemens.com/magnetom-world

SIEMENS Healthineers

Please enter your business address

Institution

Department

Function

Title

Name

Street

Postal Code

City

State

Country

MR system used

Please include me in your mailing list for the following Siemens Healthcare customer magazine(s):

☐ MAGNETOM Flash

☐ SOMATOM Sessions

☐ Imaging Life

☐ AXIOM Innovations

☐ Go HYBRID!

Stay up to date with the latest information

Register for:

E-mail

☐ Yes, I consent to the above information being used for future contact regarding product updates and other important news from Siemens.

☐ unsubscribe from info service

Please print clearly!

→ Visit www.siemens.com/magnetom-world for case reports, clinical methods, application tips, talks and much more clinical information.

Subscribe now!

– and get your free copy of future MAGNETOM Flash!

Interesting information from the world of magnetic resonance – gratis to your desk. Send us this postcard, or subscribe online at

www.siemens.com/magnetom-world

Siemens Healthcare GmbH
Antje Hellwich
HC DI MR CRM SCI
Karl-Schall-Str. 6
91052 Erlangen
Germany

MAGNETOM Flash

On account of certain regional limitations of sales rights and service availability, we cannot guarantee that all products included in this brochure are available through the Siemens sales organization worldwide. Availability and packaging may vary by country and is subject to change without prior notice. Some/All of the features and products described herein may not be available in the United States.

The information in this document contains general technical descriptions of specifications and options as well as standard and optional features which do not always have to be present in individual cases, and which may not be commercially available in all countries.

Due to regulatory reasons their future availability cannot be guaranteed. Please contact your local Siemens organization for further details.

Siemens reserves the right to modify the design, packaging, specifications, and options described herein without prior notice. Please contact your local Siemens sales representative for the most current information.

Note: Any technical data contained in this document may vary within defined tolerances. Original images always lose a certain amount of detail when reproduced.

Siemens Healthineers Headquarters
Siemens Healthcare GmbH
Henkestr. 127
91052 Erlangen
Germany
Phone: +49 9131 84 0
siemens.com/healthineers

A91MR-1000-123M-7600 Printed in Germany | PS MR 4492 01174. |